Gas dynamics and kinematical signatures of turbulent planet-forming disks

Marcelo Barraza-Alfaro

Heidelberg, 2022

Dissertation

submitted to the

Combined Faculty of Mathematics, Engineering and Natural Sciences

of Heidelberg University, Germany

for the degree of

Doctor of Natural Sciences

Put forward by

M.Sc. Marcelo Barraza-Alfaro

born in Coquimbo, Chile

Oral examination: July 27th, 2022

Gas dynamics and kinematical signatures of turbulent planet-forming disks

Referees:

Dr. Mario Flock

Prof. Dr. Cornelis P. Dullemond

Abstract

Gas dynamics and turbulence in protoplanetary disks play a crucial role in disk evolution and planet formation, not only by dictating the motion of solid particles through the planet-forming disk but also by allowing the transport of angular momentum and so the mass accretion onto the star. Significant are the effects of turbulence on dust settling, dust concentration and growth/fragmentation, fundamental ingredients for the dust to grow into pebbles and planetesimals, building blocks of planets. Therefore, exploring the gas dynamics and observational signatures of turbulence is essential to further understand its origin and impact in planet formation.

In this thesis, I present a study on the gas dynamics and kinematical signatures of disks unstable to the vertical shear instability (VSI), a robust candidate to generate turbulence in the outer regions of protoplanetary disks. Via high-resolution 3D hydrodynamical simulations post-processed with radiative transfer predictions and synthetic observations, I show that the VSI produces observational signatures in CO kinematics, observable within ALMA's capabilities. However, I also show that the interplay between the VSI and forming massive planets can substantially affect their kinematic signatures, by partially suppressing the VSI and sculpting a complex velocity structure. These predictions will help to interpret upcoming ALMA kinematical observations, potentially revealing a process behind gas turbulence in planet-forming disks.

Zusammenfassung

Gasdynamik und Turbulenz in protoplanetaren Scheiben spielen eine entscheidende Rolle bei der Scheibenentwicklung und der Planetenbildung, indem sie nicht nur die Bewegung von Staubteilchen durch die sich bildende Scheibe diktiert, sondern auch den Transport von Drehimpuls erlaubt und die damit verbundene Akkretion von Masse auf den Stern.

Bedeutsam sind die Auswirkungen der Turbulenz auf die Staubablagerung, Staubkonzentration und Wachstum/Fragmentierung, die grundlegend dafür sind dass der Staub zu Kieselsteinen und Planetesimalen, den Bausteinen von Planeten, heranwachsen kann.

Daher ist die Erforschung der Gasdynamik und dessen Beobachtungssignaturen von Turbulenzen von entscheidender Bedeutung für das weitere Verständnis ihres Ursprungs und ihrer Auswirkungen auf die Planetenbildung.

In dieser Arbeit wird eine Studie über die Gasdynamik und die kinematischen Eigenschaften von Scheiben vorgestellt. Der Fokus liegt auf der vertikalen Scherungsinstabilität (VSI), einem robusten physikalischem Prozess welcher Turbulenz in den äußeren Regionen protoplanetarer Scheiben erzeugen kann.

Mihilfe hochauflösende hydrodynamische 3D-Simulationen, die mit Strahlungstransfer-Vorhersagen und synthetischen Beobachtungen verbunden sind, zeige ich dass die VSI Signaturen in der CO-Kinematik erzeugt, die mit dem ALMA Teleskop beobachtbar sind.

Die Ergebnisse zeigen auch dass das Zusammenspiel zwischen der VSI und der Bildung massereicher Planeten deren kinematische Signaturen erheblich beeinflussen kann, indem sie die VSI teilweise unterdrücken. Diese Vorhersagen werden für kommende kinematischen ALMA Beobachtungen von hoher Bedeutung sein, die Beobachtungen zu interpretieren und den Prozess der Planetenentstehung zu verstehen.

Resumen

La dinámica y turbulencia del gas en discos protoplanetarios juega un rol crucial en la evolución del disco y la formación planetaria, no solo al dictar el movimiento de las partículas sólidas en el disco protoplanetario, si no también al permitir el transporte de momentum angular y con ésto la acreción de masa hacia la estrella.

La turbulencia causa efectos significativos en el asentamiento, concentración, crecimiento y fragmentación del polvo, ingredientes fundamentales para que el polvo crezca a granos y planetesimales, bloques que componen los cimientos de los planetas. Por lo tanto, explorar la dinámica del gas y firmas observacionales de la turbulencia es esencial para entender su origen e impacto en la formación planetaria.

En esta tesis, presento un estudio de la dinámica del gas y firmas cinemt́icas de discos inestables al vertical shear instability (VSI), un candidato robusto a generar turbulencia en las regiones externas de los discos protoplanetarios. Utilizando simulaciónes hidrodinámicas 3D en alta resolución post-procesadas con trasferencia radiativa y observaciónes sintéticas, demuestro que la VSI produce firmas observacionales en la cinemática del CO, que son observables con ALMA. Sin embargo, también demuestro que la interacción entre la VSI y los planetas masivos en formación puede afectar sustancialmente sus firmas cinemáticas, suprimiendo parcialmente la VSI y esculpiendo una estructura de velocidades compleja. Estas predicciónes ayudarán a la interpretación de futuras observaciones de cinemática con ALMA, con el potencial de revelar un proceso detrás de la turbulencia del gas en discos de formación planetaria.

In honor of my beloved mother

Contents

List of Figures

List of Tables

1 Introduction

Early on in our evolution as humans, the night sky has stimulated our imagination, with the hope that in the vast universe we find answers to the fundamental questions about our existence. How did the Earth form? What is the origin of our Solar System? Is our Solar System unique? Are there extra-solar planets similar to Earth?

From the oldest known evidence of humans looking at the night sky, such as the prehistoric paintings in the walls of the Lascaux cave in France painted about 16500 years ago and the stunningly beautiful Nebra sky disc found in Germany made roughly 3600 years ago, to today's astonishing high-resolution images from modern telescopes, a huge progress has been made by humankind's brightest minds in the comprehension of the Universe and our Solar System. A particularly important finding for our understanding of our Solar System is the discovery of extrasolar planets, firstly observed in 1992 (Wolszczan & Frail, 1992). Today, thousands of extrasolar planetary-systems have been observed[1], with an incredibly diversity of properties and architectures. From this fundamental discovery, we know that planet formation is a universal process, and that planetary systems similar to ours exist.

Nevertheless, fundamental questions about the formation and evolution of planetary systems are still standing. What is the mechanism behind planet-formation?, What is the timescale of planet formation? Which processes define the planet properties and chemical composition? These and other questions about the formation of planets are tackled by studying the so-called protoplanetary disks, disks of gas and dust that surround young stars. The early theoretical concept of a circumstellar disks came to the minds of philosophers Immanuel Kant and Pierre-Simon Laplace in their Nebular hypothesis (Kant, 1755; Laplace, 1796), a visualization of the formation stage of our Solar System. By fortune, it is possible to observe protoplanetary disks in the Solar neighborhood, where looking at nearby star forming regions (e.g., star-forming regions in the Taurus molecular cloud and Orion Nebula) and a few single systems (e.g., HD 163296 disk) we have a chance to look into the formation process of a planetary system and test planet formation theories, and at the same time try to re-construct our Solar-System history.

Among the fundamental properties of the gaseous disk that are still under investigation, turbulence is one of the most important. Globally, gas turbulence could affect the global evolution of the disk by transporting angular momentum through the disk, which could help to explain the observed stellar accretion rates. Locally, it can affect the dynamics of solids in the protoplanetary disk via diffusion and mixing, changing its ability to settle, be trapped

[1] http://exoplanets.org/

in structures, grow and fragment, important for dust to growth into larger sizes to form planetary embryos. Further, once the protoplanet is formed but still embedded, turbulence can influence its migration and accretion. Thus, comprehend the origin of turbulence is key to understand its role in these processes.

During the last decade, modern observational facilities, such as the Atacama Large Millimeter/submillimeter Array (ALMA), have been able to spatially resolve the dust and gas emission from nearby protoplanetary disks. These exquisite observations have revealed ubiquitous disk substructures (e.g., dust rings in HL Tau ALMA Partnership et al. 2015), and the direct detection of two accreting planets carving a cavity in the protoplanetary disk PDS 70 (Keppler et al., 2018; Benisty et al., 2021). Understanding the origin of these structures is fundamental: are these substructures crucial in the planet formation process or/and are a manifestation of already formed planets?

In the theoretical interpretation, numerical simulations have reproduced the observed dust substructures for a variety of possible pathways. Aforementioned, embedded planets can interact with the disk creating dust substructures; however, direct detection of embedded planets still elusive. Alternatively, dust substructures are produced naturally from physical processes in the disk. These non-planetary scenarios invoke fundamental physics, such as irradiation from the central star, fluid instabilities, disk self-gravity, magnetic fields, among others. Moreover, theoretical simulations have shown that inside these dust substructures dust can grow into pebbles, planetesimals, and planetary embryos, the building blocks of planets. Thus, understanding the origin of these dust substructures is essential.

Due the variety of mechanism capable to explain dust substructures, gas kinematics observations have gained attention, as they can indirectly reveal the presence of massive embedded planets by tracing its effect in the disk velocities (Disk Dynamics Collaboration et al., 2020); therefore, proving planet-disk interaction as origin of dust substructures. Nevertheless, kinematical observations also opens the window to study kinematical signatures of alternative mechanisms to explain dust substructures, and disk physical processes. In particular, high-resolution observations of gas tracers can be directly used to reveal signatures of instabilities operating in the disk, that could be a source of turbulence.

In this dissertation, I investigate if high resolution ALMA kinematic observations of CO could reveal signatures of the vertical shear instability (VSI). The VSI is an hydrodynamical instability that can operate in the outer regions of protoplanetary disks, and a robust candidate to generate gas turbulence. I explore the cases in which the VSI is operating in a region without already formed planets, and with an embedded massive planets carving a gap in the disk. These predictions aim to help interpretation of ALMA kinematic observations and give insights on the origin of turbulence in planet-forming disks.

1.0.1 Thesis Outline

The main objective of this thesis is to explore the kinematical signatures produced by the hydrodynamical vertical shear instability (VSI) in planet-forming disks, proposed as gas turbulence origin mechanism in the outer regions of the disk. To achieve this goal, I followed a workflow that combines three-dimensional high-resolution hydrodynamical simulations, radiative transfer calculations, synthetic imaging and kinematic data analysis. In this thesis I show support that kinematical signatures from the VSI are unique and observable in CO

kinematics within the capabilities of the ALMA interferometer. However, I also show that in the presence of embedded massive planets complex dynamical structure can results from the interplay of the VSI and planet-disk interactions, with damping of the VSI in the disk midplane regions. The thesis is organized in the following manner:

Chapter 2 I expand on the context of my thesis work by introducing protoplanetary disks, planet formation theory and observations, addressing the importance of studying turbulence in planet-forming disks, theoretical works on the VSI and planet-disk interactions, and the current status of gas kinematic studies.

Chapter 3 I describe the numerical tools used in each step of the workflow used in this thesis.

Chapter 4 In this chapter I present an investigation of the observability of the vertical shear instability in CO kinematical observations. I demonstrate that VSI produces detectable kinematical signatures in ALMA high-resolution observations of CO isotopologues.

Chapter 5 As continuation of the work shown in Chapter 4, I present a follow-up study by including the presence of massive planets embedded in the VSI-unstable disk. I show that the disk kinematical structure can be substantially affected by the interplay between planets and VSI.

Chapter 6 I summarize the research presented in this thesis and present the main conclusions. In addition, I address the future prospects of my research in planet-forming disks.

2 Brief Review of Planet formation in Circumstellar Disks

In this Chapter, I broaden on the context of the work conducted in this thesis, briefly introducing planet formation and protoplanetary disks. I focus on protoplanetary disk gas turbulence, resolved kinematic observations, and planet-disk interactions.

2.1 Protoplanetary Disks and Planet Formation

Protoplanetary disks are disks of gas and dust that surround newborn stars, in which planets are formed within and feed from its material through accretion. These disks are understood as a by-product of the formation of the central star, where the star forms via gravitational collapse in a rotating molecular cloud. Then, the material surrounding the young star forms a disk due to angular momentum conservation of the initial cloud.

From the early observational evidence of protoplanetary disks by the detection of an abnormal infrared excess in the spectral energy distribution (SED) of young stars, result of energy being re-processed in the circumstellar dust, these objects have been understood as an intermediate stage between the formation of the star and a mature planetary system, which have been classified in classes of young stellar objects (YSO). Observers have divided YSO into four classes depending on the shape of the object's SED, interpreted as different evolutionary stages: an early collapsing phase of the protostar surrounded by an envelope (Class 0), a still forming embedded disk (Class I), a envelope-free disk (Class II), and a disk of debris in which the gas has already been dispersed (Class III). This simplified evolution of a YSO is constrained to take place in tens of Myr timescale, in which the earliest Class 0 and I stages occur in the first Myr of the system's evolution. In addition, a particular class of disks has been observed, the so called transition disks, which

show a dust-depleted cavity; however, still unclear if these are a transitional stage between class II and III.

While a fairly clear idea of the evolution of a YSO is set, it is still unclear at which stage planet formation takes place. Two main theories have been proposed to explain the formation of planets, gravitational instability and core-accretion. The first, explains planet formation as consequence of disk being massive enough to be unstable to gravitational instabilities, fragmenting the circumstellar disk. The second, supports the idea of the formation of a planetary core via growth of solids, that when reaching a critical mass can trigger efficient accretion of material from the disk (e.g., Goldreich & Ward, 1973). These theories have different requirements, timescales and barriers. Gravitational instability is predicted to be very efficient, having a timescale comparable to the local orbital timescale; however, a disk with a large amount of mass in gas and efficient disk cooling are required. Core -accretion has a larger timescale, and requires the dust to growth several orders of magnitude in size, going from micron-sized dust to planetesimals of hundreds of km in size.

In addition to detect forming planets, trying to find observational evidence of core-accretion and GI has been the goal of the community studying planet formation. Observations trying to constraint disk masses from dust and molecular line observations, have concluded that the bulk of the mass of protoplanetary disks is stored in gas phase, but most of them do not reach the required mass to trigger gravitational instabilities or are marginally gravitationally unstable (see e.g., Miotello et al., 2022). Still, there is a large uncertainty in the measurements of disk masses, due the strong assumptions and complex modelling. Moreover, GI might proceed fast in the earliest stages of the disk, which are harder to catch in observations, and harder to analyze due the presence of the envelope. For the case of core-accretion, observational evidence is hard to find, since is not feasible to observe large solid bodies. Nevertheless, dust observations show concentrations of emission in rings and crescent shaped morphology, which trace dust concentrations (e.g., ALMA Partnership et al., 2015). Further, multi-wavelength radio observations have shown that inside the sub-substructures larger size of dust is present (Carrasco-González et al., 2019), confirming that growth of solids has taken place.

Spatially resolving dust substructures and explore their origins has been the focus in the last decade, as they are regions of solids concentration, and/or

might be produced by protoplanets. For this purpose, large surveys have been performed in particular with ALMA (e.g., DSHARP survey, Andrews et al. 2018) and the Very Large Telescope (e.g., DARTTS-S survey, Avenhaus et al. 2018; Garufi et al. 2020). These surveys have revealed an incredible rich amount of substructures in protoplanetary disks, including gaps, rings, crescents and spiral arms. The theoretical interpretation is that these dust substructures are a direct reflection of the gas dynamics of the protoplanetary disk, in which gas exerts a drag force in the dust particles depending on its Stokes number. In particular, variations in the disk pressure structure can modify the gas velocity, creating a maxima to whose particles move towards or pressure-trap of dust (Pinilla et al., 2012a,b). Thus, resolving the gas dynamics is needed to disentangle the origin of dust structures.

Thanks to ALMA, now its possible to resolve the emission of gas tracers, both spatially and spectrally. These observations have also shown substructures in both its spatial distribution and kinematics. Today, having a multi-wavelength picture of the brightest protoplanetary disk is possible (see e.g., Figure 2.1), probing a three-dimensional view of the disk. Understanding a global picture to interpret these resolved can help us to disentangle the physical and thermo-chemical processes operating in the disk, constrain the disk properties, and find evidence of unseen forming-planets.

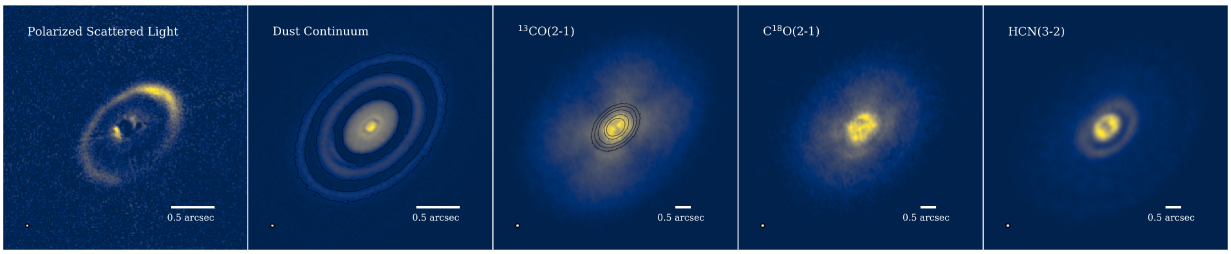

Figure 2.1: Multi-wavelenght observations of the HD 163286 protoplanetary disk, showing rich amount of substructures in both gas and dust. From left to right: dust polarized scattered light observations with SPHERE/VLT (Muro-Arena et al., 2018), dust continuum emission observations with ALMA, and gas tracers ^{13}CO, C^{13}O and HCN integrated emission observed with ALMA (Öberg et al., 2021). Note the difference in scale, shown in the right-lower corner of each panel. The black contours in the middle panel trace the disk continuum emission.

2.2 On the importance of disk turbulence

Gas turbulence plays an important role on the global disk evolution and the dynamics of gas and dust in the disk, relevant for planet formation. Therefore, studying its possible origins is crucial to further understand its impact in the formation of a planetary system.

In the global disk evolution, gas turbulence can regulate the radial transport of angular momentum outwards through the generation of an effective viscosity, allowing the gas to accrete onto the central star (Shakura & Sunyaev 1973; Lynden-Bell & Pringle 1974; see also PP review chapters in Turner et al. 2014 and Lesur et al. 2022). Locally, turbulence can be crucial for different physical processes relevant for planet formation, for example, gas accretion onto protoplanets (Picogna et al., 2018), the formation and lifetime of vortices (Fu et al., 2014), dust settling (Fromang & Papaloizou, 2006), and dust growth and concentration in pressure bumps (Ormel & Cuzzi, 2007; Birnstiel et al., 2010; Pinilla et al., 2012a,b). Moreover, radial variations in the strength of the turbulence can trigger the formation of pressure bumps (Lyra et al., 2009; Regály et al., 2012; Flock et al., 2015).

Observations of both gas and dust, in combination with detailed radiative transfer modelling, have been used in order to constrain the strength of turbulence in protoplanetary disks. From high spatial resolution ALMA dust continuum observations, it is possible to measure a global value from the vertical settling observed in edge-on disks (Villenave et al., 2020, 2022), and a local value from the radial and vertical extent of dust rings (Pinte et al., 2016; Dullemond et al., 2018). Both approaches have obtained a low level of turbulence; therefore, dust is well settled into the disk midplane and dust rings are radially narrow. However, constraints of gas turbulence from dust (sub-)mm observations are indirect and limited to the midplane layer of the disk.

Gas tracers observations can serve as a direct measurement of gas turbulence, by studying the impact of the turbulent motions onto the broadening of molecular lines. Still, obtaining the magnitude of the gas turbulent velocities is incredibly challenging, as the emission from rotational transitions of molecules at radio wavelengths have a substantial contribution from thermal broadening (e.g., Flaherty et al. 2020; Pinte et al. 2022). Thus, most studies of line broadening in sub-mm observations have only allowed to set upper limits on disk turbulence. Early attempts to measure turbulence from

spatially unresolved line broadening with the Submillimeter Array (SMA) enabled Hughes et al. 2011 and Guilloteau et al. 2012 to derive turbulence upper limits for the bright disks TW Hya, HD 163296 and DM Tau of around 40, 300, and 130 m s^{-1}. Recently, the Atacama Large Millimeter/submillimeter Array (ALMA) has allowed for a direct study of the gas turbulence in the disk's outer regions ($\gtrsim 30$ au) for the first time via spatially resolved observations of molecular gas lines. From the search of nonthermal line broadening, weak levels of turbulence ($\lesssim 5-10\%$ the local sound speed) have been constrained in HD 163296, TW Hya, MWC 480, and V4046 Sgr protoplanetary disks (Flaherty et al., 2015; Teague et al., 2016; Flaherty et al., 2017, 2018; Teague et al., 2018b; Flaherty et al., 2020). Conversely, one detection of turbulence has been possible in the disk DM Tau ($0.23-0.33\,c_s$; Flaherty et al., 2020). Furthermore, opposite to dust constraints, turbulence measurements obtained from molecular line observations can trace different emission disk layers, with the potential of mapping the value of turbulent motions at different regions of the disk. However, a precise constraint on the disk temperature is necessary to extract the effects of non-thermal motions on the integrated line emission, and strong assumptions are used in the modelling of turbulence.

The aforementioned constraints of turbulence have been incredible difficult to obtain for both gas and dust observations, by requiring high resolution observations with good sensitivity, and complex radiative transfer modelling. For this reason, turbulence constraints have been obtained on only a handful of the brightest nearby protoplanetary disks. Nonetheless, despite the limited sample, its observed that most of the targets show weak level of turbulence ($\alpha \lesssim 10^{-3}$), an important indication on the nature of gas turbulence in the outer regions of protoplanetary disks.

From a theoretical perspective, strong conclusions can be drawn from the low level of disk turbulence observed. First, the magneto-rotational instability (MRI) can be discarded as the main driver of turbulence in the outer regions of protoplanetary disks, since higher values of turbulence are predicted from theoretical studies in the case in which MRI is fully active (Simon et al., 2015). Second, gas turbulence has a partial contribution on driving gas accretion onto the central star, likely operating in combination with magnetically-driven winds that remove angular momentum from disk (Turner et al., 2014; Bai, 2017). These results are consistent with outer protoplanetary disk regions being weakly ionized (Dzyurkevich et al., 2013; Desch & Turner, 2015);

therefore, the magneto-rotational instability (MRI, Balbus & Hawley, 1991; Hawley & Balbus, 1991) is unlikely to be active in most disk regions. In this MRI "dead-zone", pure hydrodynamical instabilities are expected to dominate as the turbulence source. However, several hydro-instabilities have been proposed to operate inside the dead-zone, for example, zombie vortex instability (ZBI, Marcus et al., 2015, 2016), convective overstability (COV, Klahr & Hubbard, 2014; Lyra, 2014), and the vertical shear instability (VSI, Nelson et al., 2013). Yet, these instabilities require specific local disk conditions, and which hydro-instability prevails strongly depends on the local cooling timescale (see e.g., Malygin et al., 2017; Lyra & Umurhan, 2019; Pfeil & Klahr, 2019; Lesur et al., 2022). Nevertheless, determining the turbulence level alone is not enough to confirm the dominant instability. In order to disentangle which one of these is at play, imperative are a combination of resolved kinematic observations and predictions of observational signatures from disk hydro-instabilities. In this thesis, I focus on the study of kinematic signatures produced by the VSI, that could help to identify it operating in the outer regions of planet-forming disks.

2.2.1 The vertical shear instability

The vertical shear instability (henceforth VSI, Nelson et al., 2013; Stoll & Kley, 2014) is a purely hydro-instability that operates in the outer disk regions with fast cooling (Pfeil & Klahr, 2019), which produces anisotropic turbulence (Stoll, Moritz H. R. et al., 2017). It arises naturally from the vertical gradient of the disk's angular velocity, where the surface layers rotate more slowly than the midplane. The VSI works more efficiently in isothermal disks (Nelson et al., 2013), but can also be active in a radiative disk (Stoll & Kley, 2014; Flock et al., 2017, 2020). Moreover, it can also be effective in a magnetized disk where nonideal MHD effects suppress the MRI (Cui & Bai, 2020). The VSI produces large-scale gas motions in its saturated state, which correspond to the long-wavelength modes. The large-scale gas motions have a characteristic meridional circulation pattern (see Figure 2.2), in which the gas vertical motions can produce stresses significantly larger than the radial motions (Stoll, Moritz H. R. et al., 2017). A small-scale component can also be seen as turbulent eddies (Flores-Rivera et al., 2020).
The effective Shakura & Sunyaev α viscosity generated in the radial direction by the VSI has been found to be small, with values between 10^{-4} and

10^{-3} (Nelson et al., 2013; Flock et al., 2017; Stoll & Kley, 2014; Manger & Klahr, 2018). This low level of turbulence is consistent with the upper limits constrained from ALMA molecular gas line observations mentioned above (Flaherty et al., 2015; Teague et al., 2016; Flaherty et al., 2017, 2018, 2020), and with the recent estimates from CO evolution models (Trapman et al., 2020).

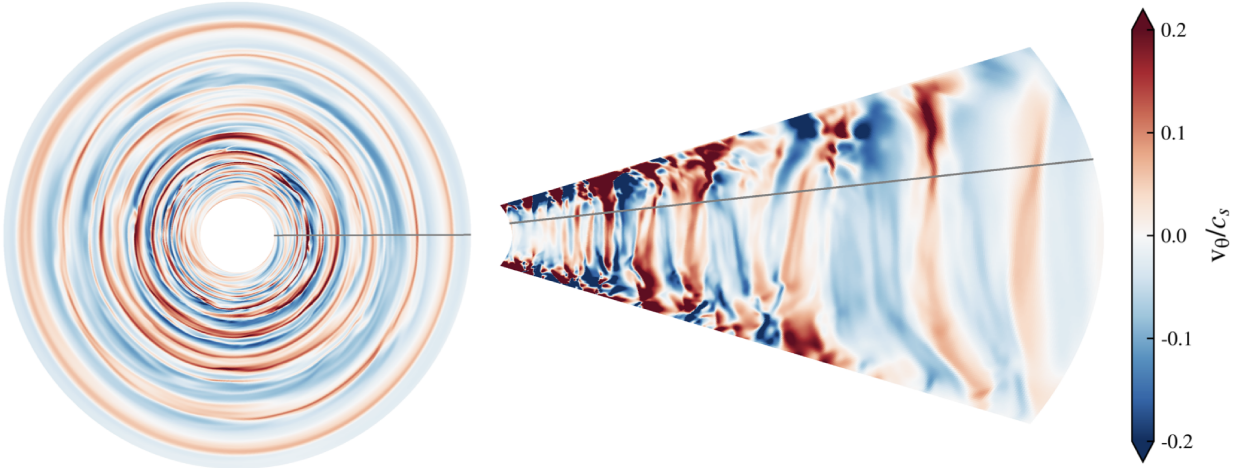

Figure 2.2: Slices of the gas meridional velocity structure produced by the vertical shear instability (VSI). The slice showing the disk face-on is taken at about $2H$ from the midplane. The VSI induces quasi-axisymmetric meridional flows with a corrugated pattern.

The VSI is one of the most robust instabilities to operate in the outer regions of protoplanetay disks, under the assumption that magnetic fields remain decoupled from the gas; however, it can be partially suppressed in layers where the local physical conditions forbid efficient cooling. For example, in the uppermost layers of the disk gas and dust collisional decoupling can increase significantly the local relaxation time suppressing the growth of the VSI (Pfeil & Klahr, 2021). Moreover, linear instability analysis show that the inclusion of dust evolution can also constrain the VSI active region to the midplane disk layers (Fukuhara et al., 2021). Nevertheless, realistic global 3D simulations that can self-consistently constrain the layers in which the VSI can operate are still under development. Still, looking for signatures of the VSI operating at different layers traced by, for example, CO isotopologues, can help to constrain the regions in which the conditions for VSI to operate are satisfied.

The gas dynamics produced by the VSI has direct influence on the dynamical evolution of solid dust grains. First, the VSI vertical motions can lift

up grains settled towards the midplane, increasing the dust scale height of (sub)mm dust particles (Flock et al., 2017, 2020). Second, the VSI meridional circulation can induce dust traffic jams, that is radial regions where the speed of radial drift is reduced (Stoll & Kley, 2016; Flock et al., 2017, 2020). Such traffic jams can produce overdensities of dust, possibly helping planetesimal formation by creating the conditions to trigger the streaming instability (SI) (Schäfer, Urs et al., 2020). Third, the VSI can also produce anticyclonic vortices in the gas velocities (e.g., Manger & Klahr 2018; Pfeil & Klahr 2021, that can efficiently trap dust particles in their centers creating azimuthally concentrated dust traps, once again helping to reach the conditions for dust growth and planetesimal formation. Nevertheless, such dust substructures can also be induced by alternative mechanisms; therefore, studying the resolved kinematic structure is needed to robustly disentangle the VSI in protoplanetry disks.

For a thorough description on disk fluid instabilities including the VSI see, for example, review by Lyra & Umurhan 2019 and the recent Protostars & Planets VII review chapter on disk hydro-, mangetohydro- and dust-gas dynamics in protoplanetary disks by Lesur et al. 2022.

2.3 Resolved kinematic observations of planet-forming disks

The study of the gas kinematics in protoplanetary disk has been demonstrated to be crucial to unveil the physical processes in the disk (Pinte et al., 2022). Thanks the development of ALMA, high spectral and spatial resolution of molecular line emission can be performed, allowing the study of the dynamical structure of planet forming disk. These observations can reach spatial resolutions that can resolve the disk pressure scale height of the disk ($\lesssim 10$ au), needed to spatially resolve disk substructures. Not only that, ALMA observations can map the disk with fine spectral resolution, that can reach a velocity resolution of ≈ 30 m s^{-1} in Band 7 observations. Such data quality it is so exquisite that can reveal dynamical perturbations in the disk relative to the background Keplerian disk rotation (Disk Dynamics Collaboration et al., 2020).

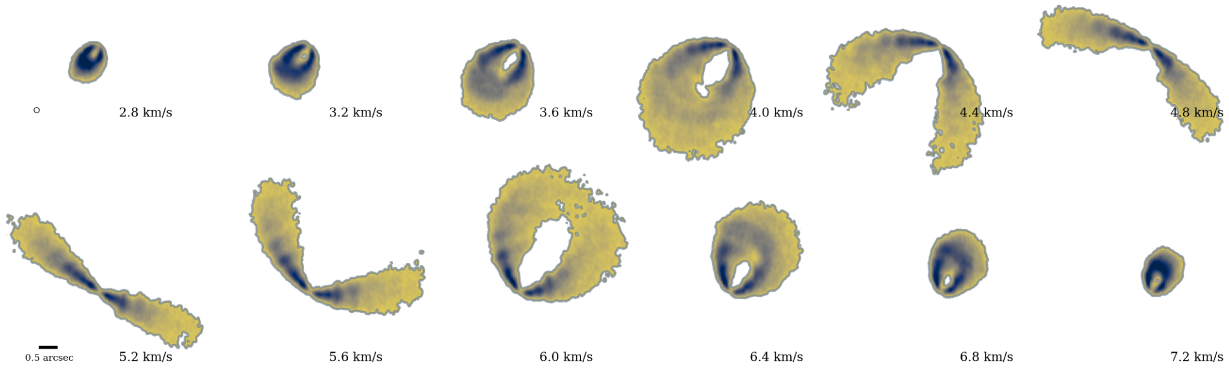

Figure 2.3: Emission from individual velocity channels of ^{12}CO ALMA observations of the protoplanetary disk MWC 480 (Öberg et al., 2021; Teague et al., 2021).

The observed disk substructures has been successfully reproduced via numerical simulations of planet-disk interactions for most protoplanetary disks (e.g., Zhang et al., 2018; Baruteau et al., 2019). However, with the exception of the transition disk PDS 70, these companions have not been directly observed (Asensio-Torres et al., 2021). In spite of this, oriented by theoretical predictions of planetary induced kinematical signatures (Perez et al., 2015; Pérez et al., 2018), long integration observations of CO have been performed for the brightest protoplanetary disks, with the aim to find indirect evidence of putative hidden population of forming planets. Moreover, the analysis of such data products required the development of new techniques to ex-

tract weak kinematical perturbations (Teague et al., 2018a, 2019a; Casassus & Pérez, 2019), and dedicated post-processed numerical simulations, with a fruitful outcome of signatures consistent with embedded planets detected in HD 163296 (Teague et al., 2018a; Pinte et al., 2018; Teague et al., 2021; Izquierdo et al., 2022) and HD 97048 (Pinte et al., 2019). Nevertheless, kinematic observations have also revealed a myriad of intricate non-Keplerian kinematical signatures in other targets, including 'Doppler-flips' (Casassus & Pérez, 2019; Pérez et al., 2020), large-scale spiral arms (Teague et al., 2019b; Wölfer, L. et al., 2021), and rings/arcs (Teague et al., 2021).

Circumstellar disk theory and observations reveal that the global motion of the gas around the star follows (sub-)Keplerian rotation. Therefore, velocity perturbations in kinematics data are understood as deviations relative to a reference disk equilibrium solution (or unperturbed disk solution). Such perturbations can be hunted in individual velocity channel maps (e.g., Pinte et al., 2018, 2020), in which each channel shows the spatial distribution of gas moving within a finite range of velocities in the velocity projected into the line-of-sight (see e.g., channel maps of MWC 480 in Figure 2.3). Also can be seen as coherent structures in the model residuals when subtracting a background (sub-)Keplerian disk model to the line-of-sight velocity map of the traced molecule (e.g., Teague et al., 2019b, 2021). The simplest reference model adopted is an axis-symmetric Keplerian background model, that accounts for the geometry of the emission surface and the disk orientation (see details in Chapter 3 Section 3.3.2). An example of the later approach is shown in Figure 2.4, in which the model residuals reveal subtle deviations from the global Keplerian rotation, unveiling a complex kinematic structure (Teague et al., 2021). Alternatively, a radial view of the disk velocities structure can be obtained by stacking the spectral cube in concentric annulus, with the advantage to find weaker perturbations thanks to a boosted sensitivity. Not only that, its possible also to decompose each velocity component, which has been applied to find meridional flows in HD 163296 (Teague et al., 2019a) and HD 169142 (Yu et al., 2021). Still, a robust possible origin of the kinematical signatures should be compatible with all the views stated above, that is, individual channels emission, coherent non-Keplerian structures, and radial velocity profiles.

Although most of the times kinematic signatures are interpreted as the dynamical imprint of planets, the incredible potential of ALMA kinematic observations has provoked the research of kinematical signatures from alter-

native physical mechanisms. Three-dimensional simulations combined with radiative transfer post-processing, have predicted observable kinematic signatures for gravitational instabilities (Hall et al., 2020), with a tentative detection in Elias 2-27 (Paneque-Carreño et al., 2021); anti-cyclonic vortices (Robert et al., 2020), consistent with the observed structure in HD 142627 (Boehler et al., 2021); (sub-)stellar companions, observed in HD 100453 (Rosotti et al., 2019); and VSI (Barraza-Alfaro et al., 2021), whose kinematical signatures are studied in this dissertation. These findings demonstrate the extraordinary potential of ALMA to unveil the disk physics by resolving the disk kinematic structure.

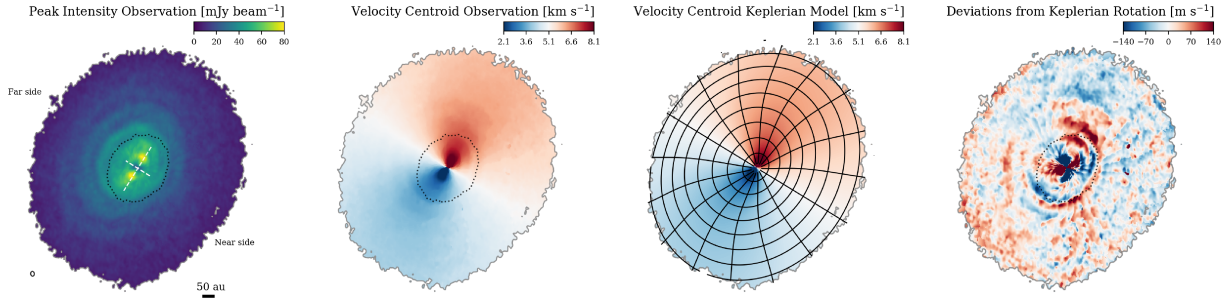

Figure 2.4: ALMA MAPS $^{12}CO(2-1)$ observations of MWC 480 (Öberg et al., 2021; Teague et al., 2021). From left to right, are shown the peak intensity map, velocity in the line-of-sight, best fit Keplerian model, and model residuals representing deviations from Keplerian rotation. The overlaid dotted black line shows the extent of the mm-dust continuum, while the solid black lines in the third panel show the model elevated emission surface.

For a complete picture of the current status of planet-forming disk kinematics and their interpretation see (Disk Dynamics Collaboration et al., 2020), and recent PPVII chapter by Pinte et al. 2022.

2.4 Planet-induced Substructures

ALMA continuum observations have discovered ubiquitous dust substructures, whose morphology are consistent with unseen forming planets. These findings might indicate a population of massive planets orbiting at large distances from the star ($r \gtrsim 10$ au); however, elusive to its direct detection (Disk Dynamics Collaboration et al., 2020). Such statement have gained support from the observations of substructures in early stages of the disk (Segura-Cox et al., 2020), hinting that planet formation might occur in the first 0.5 Myr of the disk evolution. Moreover, the rotational profile of the disk with kinematic signatures of protoplanets is consistent with planet-induced pressure bumps, radially trapping dust at their maxima (Teague et al., 2018a). Thus, for studies of observational signatures of disk physical processes, it's necessary to consider the possible influence that an unseen massive planet might have in the observable structures. Consequently, in this thesis in include the presence of massive planets on the study of kinematical signatures produced by the VSI, presented in Chapter 5.

The influence of the planet in their host disk can manifest in a range of disk substructures and gas flows spanning a wide range of spatial scales. These substructures created by the planet can be divided in different categories: spirals arms, gaps/rings, spiral wakes, vortices, turbulent motions, circumplanetary disks, and meridional circulation. However, the morphologies and velocities of these structures strongly depend on the planet's mass. For example, depending on its mass is that a planet could open a gap or induce meridional flows. Particularly important its the mass in which non-linear effects start to become significant, substantially affecting the planet triggered structures. This mass its the so-called thermal mass, defined as:

$$M_{th} = \frac{c_s^3}{\Omega_K G} = M_\star \left(\frac{H}{R_P}\right)^3, \tag{2.1}$$

where $M_\star$ is the mass of the central star, H and R_p are the pressure scale height at the planet's position and radial distance from the star to the planet, respectively. In a disk model for a Solar mass central star and a disk aspect ratio ($h = H/R$) of 0.1 at the planet's position, the thermal mass is approximately the mass of Jupiter (with a planet-to-star mass ratio of $\approx 10^{-3}$). Figure 2.5 shows the influence of an embedded Jupiter mass planet in the gas density and velocity field of the protoplanetary disk. Note that these

values represent the average value for one disk pressure scale height, starting at the disk midplane, in order to highlight the presence of meridional flows, which are cancelled out at the midplane layer. In the gas density (ρ/ρ_0), the massive planet opens a gap, triggers spiral arms and spiral wakes. In the radial velocity (v_{rad}), strong flows reaching up to few percents of the local Keplerian speed develop around the planet's location, and the Lindblad spiral arms. In the meridional velocity (v_θ), vertical flows are seen around the gap location. Finally, in the azimuthal direction, strong velocity deviations are seen along the spiral wakes and along rings of sub- and super- Keplerian gas in the gap and gap's edges. Following, a brief summary on formation theory and observational signatures of these variety of substructures is presented, highlighting the differences between linear theory and simulations of massive planets.

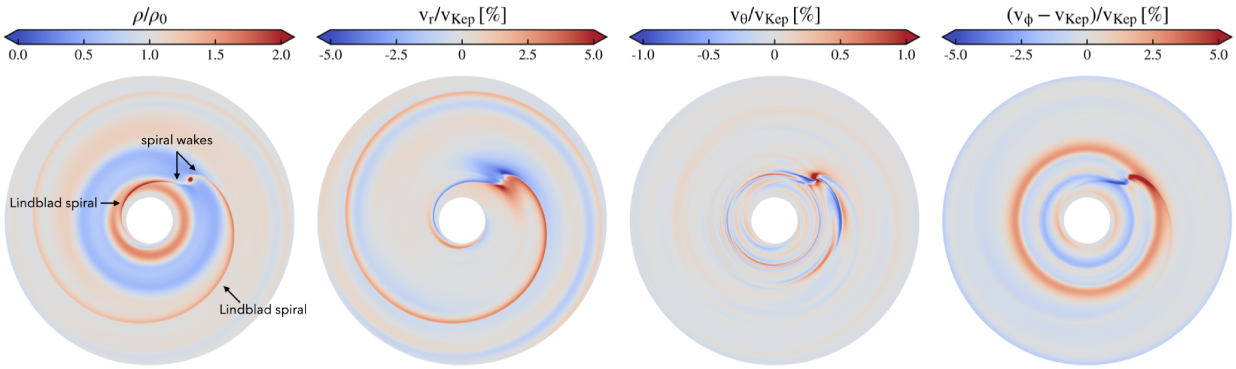

Figure 2.5: Structures induced by an embedded Jupiter mass planet in a protoplanetary disk, showing the *average* value from the disk midplane to one pressure scale height. Simulations show a broad range of substructures: *Gaps, rings, spiral wakes, spiral arms and meridional flows.*

2.4.1 Spiral arms

A planet can excite large-scale spiral arms in the gas via Lindblad resonances (Goldreich & Tremaine, 1980), that is, the orbital frequency of the planet is in resonance with the local gas epicyclic frequency. These large scale spiral arms can efficiently transport angular momentum trough the disk and give origin to gaps.

In numerical studies, relatively low mass planets create the Lindblad spirals expected from linear theory, that is, one spiral outer and one spiral inner to the planet's orbit. However, hydrodynamical simulations of planet-disk inter-

actions of planets above the thermal mass show the development of multiple spiral arms inside the planet's orbit. While the development of multiple spiral arms is strongly affected by non-linear effects, recent works explain their origin as constructive interference of different sets of wave modes around the Lindblad resonances (Bae & Zhu, 2018).

In the dust distribution of the disk, spiral arms are expected to be present for the dust well coupled to the gas. For example, the μm-sized dust observable in near-infrared wavelengths. In continuum observations at radio wavelengths, spiral arms are hard to observe as they do not act as efficient traps of mm-sized dust. Nevertheless, current predictions indicate that it might still be possible to extract thermal emission from Lindblad spirals in ALMA observations (Speedie et al., 2022).

Finally, in a inefficiently cooled disks with realistic thermodynamics, an additional set of spiral arm can develop via buoyancy resonances (Bae et al., 2021). These spirals are tightly wound compared to the Lindblad spirals, and have a strong vertical velocity component.

2.4.2 Gaps and rings

As mentioned above, spiral arms are the responsible for the opening of a gas density gap in the disk, by depositing angular momentum of the locations in which the spiral steepens into a shock (Bae et al., 2017). The gas density structure developed in the gap region has a direct consequence in the pressure structure of the disk, forming rings of super- and sub- Keplerian gas. These pressure changes in the disk create radial dust traps in the disk, in the radial regions in which the pressure has a maxima (Pinilla et al., 2012a). Planet-induced dust traps have been invoked to explain ringed structures observed in (sub-)mm dust continuum emission (e.g., Dipierro et al., 2015; Zhang et al., 2018). However, the gap properties, such as width and depth not only depend on the planet's mass, but also on the disk temperature and gas viscosity (e.g., Kanagawa et al., 2016). In particular, gas turbulence plays an important role in gap formation acting as a diffusion mechanism re-filling the gap.

Meridional circulation

As direct consequence of the depletion of gas in the gap modifying the vertical pressure gradient, planets can generate vertical flows (Kley et al., 2001; Tanigawa et al., 2012; Szulágyi et al., 2014; Morbidelli et al., 2014). On an

azimuthal average, inside the gap these flows are expected to move gas from the upper layers of the disk towards the midplane. On the contrary, at the gap edges the flows move from the midplane towards the disk atmosphere. The meridional circulation of gas can directly affect the dust vertical distribution in the disk, by lifting up grains from the midplane (Binkert et al., 2021; Bi et al., 2021). Moreover, it is theorized that they can modify the disk thermochemical evolution via mixing (Alarcón et al., 2020).

Turbulent motions

Along the planet-carved gap region and along the Lindblad spiral arms gas flows are expected to have an increase on the gas velocity dispersion (Dong et al., 2019). Such turbulent flows are expected to increase the width of the molecular emission line by introducing non-thermal broadening, potentially observable in deep kinematic observations.

2.4.3 Anticyclonic vortices

In disk with low effective gas viscosity, the Rossby-wave instability can be triggered at the sharp gap edges, developing long-lived anti-cyclonic vortices (e.g., Huang et al., 2018). The importance of these structures on planet-formation its due the effect of the gas onto the solid dust particles (Barge & Sommeria, 1995). These, vortices can efficiently trap dust, creating crescent-shaped azimuthal asymmetries (Baruteau et al., 2019). Inside these dust traps, high dust-to-gas mass ratio is reached, ideal for dust to growth and planetesimal formation (e.g., Li et al., 2020). While these vortices have been predicted to be observable in gas kinematics (Robert et al., 2020), they are strongest close to the midplane layer of the disk, harder to trace with good sensitivity in high-resolution molecular line observations.

2.4.4 Circumplanetary disks

The material of the disk flowing towards the planet is expected to form a circumplanetary disk (CPD) before its accreted into the planet. This structure is present at spatial scales below the planet's Hill radius, with large velocities compared to the local Keplerian rotation. The CPD region is connected to the disk via the spiral wakes and meridional flows, whose dictate how the material falls towards the CPD region and its accreted into the planet. In

particular, most recent simulations show that meridional flows of gas plays a fundamental role in the planet accretion process (Szulágyi et al., 2022).

Sub-mm dust particles can form a long lived CPD, predicted to be observable at radio wavelengths (Zhu et al., 2018; Szulágyi et al., 2017). Such CPD emission was observed for the first time in recent high resolution ALMA observations of the dust continuum around the disk PDS 70 (Benisty et al., 2021). This breakthrough discovery opens the door to empiric studies of solid accretion towards the CPD region and moon formation.

Circumplanetary disk are also expected to leave an imprint in the gas kinematics. Particularly, the CPD region is expected to emit offset of the Keplerian disk at several individual velocity channel maps, due the large velocities of the CPD gas (Perez et al., 2015; Disk Dynamics Collaboration et al., 2020). Moreover, it could also produce a localized increase of the line width of the molecular emission at the CPD region (Perez et al., 2015).

2.4.5 Interpreting planet-induced substructures

Despite the variety of structures triggered by embedded planets in their host disks, the large scale features have alternative scenarios. For example, as described in Section 2.2.1, the VSI can produce dust rings via traffic jams, anticyclonic vortices and meridional flows. The structures localized around the planet's location, that is, spiral wakes and circumplanetary disk, can easily confirm the planet scenario, but are harder to observe as they are shown in smaller spatial scales. Therefore, connecting different observational signatures in multi-wavelength observations to a single planet can confirm an indirect detection. Nevertheless, understanding the alternative scenarios and their interplay with planet triggered structures is crucial. This having been said, gas kinematics is a powerful tool to disentangle different mechanisms, as it can directly probe the induced gas flows in the disk at different disk layers (e.g., Teague et al., 2021).

For a more detailed description of planet-disk interactions and their observational signatures see, for example, dedicated chapters in the Protostars and Planets Series (Baruteau et al., 2014; Paardekooper et al., 2022), and gas kinematics review chapters (Disk Dynamics Collaboration et al., 2020; Pinte et al., 2022), respectively.

3 Numerical Methods

This chapter presents descriptions of the numerical methods used in the research presented in this Thesis (Chapters 4 and 5).

3.1 Hydrodynamical Simulations

The numerical simulations works presented in this thesis were performed using the publicly available versions of the PLUTO[2] code (Mignone et al., 2007). The PLUTO code is a Godunov grid based code that can solve fluid dynamics problems including relativistic and non-relativistic magneto-hydrodynamics. For the numerical simulations presented in Chapter 4 we used PLUTO version 4.3, while for Chapter 5 we used version 4.4.

I conducted global high-resolution hydrodynamical simulations of isothermal circumstellar disks unstable to the vertical shear instability. By global referring to simulations of a full disk, as to differentiate from local-box simulations which only simulate a small section of the disk.

We use the HD module of the PLUTO code to solve the Navier-Stokes equations of classical fluid dynamics:

$$\frac{\partial \rho}{\partial t} + \vec{\nabla} \cdot (\rho \vec{v}) = 0 \tag{3.1}$$

$$\frac{\partial (\rho \vec{v})}{\partial t} + \vec{\nabla} \cdot (\rho \vec{v} \vec{v}^{\mathrm{T}}) = -\vec{\nabla} P - \rho \vec{\nabla} \Phi, \tag{3.2}$$

were ρ is the gas mass density, $\vec{v}$ is the gas velocity vector, P is the pressure, and Φ is the gravitational potential. The fluid is affected by the gravitational

[2] http://plutocode.ph.unito.it/

potentials of a star only in Chapter 4, $\Phi_\star = -GM_\star/r$, while in Chapter 5 we add the potential of embedded massive planets.

For all the simulations presented, the hydrodynamical equations were solved using a second-order accurate scheme with linear spatial reconstruction (LINEAR), with the least diffuse limiter implemented in PLUTO (monotonized central difference limiter; MCLIM). For the time stepping calculation, I chose second-order Runge-Kutta time-stepping (RK2), while for the solver we use the Harten-Lax-Van Leer-Contact (HLLC) Riemann solver, that restores with the middle contact discontinuity. The Courant number (CFL), that controls the time step lenght, is set to 0.25 for the simulations of Chapter 4, and 0.3 in Chapter 5, with no differences in the results[3].

For the VSI-unstable disk simulations I run inviscid numerical simulations; therefore, technically the code solves the Euler equations. However, for the simulations including an artificial viscosity presented in Chapter 5, I include the viscous stresses into the HD equations, implemented as a parabolic diffusion term in the momentum equation. The viscosity depends on a shear viscosity coefficient (ν), which we set to follow the alpha viscosity prescription of Shakura & Sunyaev 1973:

$$\nu = \alpha c_s H, \tag{3.3}$$

with α the widely used alpha constant parameter, which I set to be $\alpha = 5 \times 10^{-4}$. c_s and H denote the local sound speed and the disk pressure scale height. For the numerical integration of the diffusion term we chose the Super-Time-Stepping (STS) technique as implemented in PLUTO, which accelerates the calculations compared to an explicit treatment.

For all simulations, the computational domain extends from 0.4 to 2.5 code units of length in the radial direction, and in the azimuthal direction the grid covers the full 2π rad. However, in the vertical (or merdional) direction the model covers approximately ~ 9 disk scale heights in total for the simulations presented in Chapter 4, and ~ 10 for the ones presented in 5. Note that we simulate the full disk, that is both disk hemispheres; thus, for example the simulation grids of Chapter 5 cover $5H$ at each side of the disk midplane ($Z = 0$).

The grid of our simulations follow an spherical geometry, logarithmically spaced in the radial direction r, while evenly-spaced in colatitude (θ) and

[3]The stability criterion is $CFL \lesssim 1/N_{dim}$ for our setup, with N_{dim} the number of dimensions.

azimuth (ϕ). For the simulations presented in Chapter 4 resolution of the grid is $(r, \theta, \phi) = (512, 128, 1024)$, which gives a resolution of roughly 14 cells per scale height and cells with an aspect ratio $\delta r{:}r\delta\theta{:}r\delta\phi$ of approximately 1:1.9:1.7. The simulations later presented in Chapter 5 have a higher resolution in the vertical direction, with 192 grid cells in colatitude (19 cells per scale height).

Since our simulations follows a locally isothermal equation of state, these can be re-scaled to any physical radial distance. However, the reference aspect ratio at the code unit of lenght of $H/R = 0.1$ set in our simulations fits best for a disk model re-scaled to around 100 au. Aditionally, the stellar mass is set to be equal to one Solar Mass ($M_\star = 1 M_\odot$). Therefore, I use these reference values to re-scale our simulation results in all figures presented in Sections 4.2.2 and 5.2, and also for the radiative transfer post-processing.

In the set of simulations presented, I adopted similar boundary conditions as Flock et al. (2017), which consist in the following: In colatitude, it corresponds to a modified outflow boundary condition which enforces zero inflow of gas into the computational domain. In the gas density, it extrapolates the logarithmic field along the meridional direction into the ghost cells. Additionally, includes a softening of the azimuthal velocity radial gradient, only at the meridional interface between the ghost cells and the computational domain to reduce effects from the boundary corners. In the radial direction, enforced zero inflow of gas is also imposed. In order to minimize wave reflections close to the inner and outer radial boundaries, I include buffer zones in which the gas density and radial velocity are damped to the initial profiles. In the simulation of Chapter 4 the buffer zones are equal to 20% of the inner and outer edge radius, respectively. Due the inclusion of planets, a larger buffer zone at the inner boundary is implemented for the simulations of Chapter 5, equal to 25% of the grid inner radius. Morevoer, the damping in the simulations of Chapter 5 is faster, with a timescale of 10% of the local orbital period, while being 30% in the simulation shown in Chapter 4.

I present a summary of the parameters used in the simulations presented in this thesis in Table 3.2.

3.2 Radiative Transfer Calculations

To produce synthetic images of molecular line emission of a VSI-active disk, the simulations outputs are post-procesed with the Monte-Carlo radiative transfer code RADMC-3D[4] (Dullemond et al., 2012). The RADMC-3D version 0.41 was used in Chapter 4 and version 2.0 in Chapter5, with no significant differences in the results. The construction of the RADMC-3D input files from simulation data is partly based on the FARGO2RADMC3D[5] scripts (Baruteau et al., 2019).
We explore as observable the spatially resolved velocity centroid map (also labeled line-of-sight velocity map) computed from synthetic CO channel maps. To study the effect of different tracer abundance, the synthetic maps for three different CO isotopologues are computed: ^{12}CO, ^{13}CO and C^{18}O, whose probe different disk layers. In Chapter 4 we compute predictions for the J=2-1 transition observable in ALMA Band 6, while in Chapter 5 we compute the data cubes for the J=3-2 transition observable within ALMA Band 7. No significant differences are observed in the choice of transition for our models besides the traced emission layer being higher for the J:3-2 transition. Nevertheless, ALMA Band 7 has finer spectral resolution available, ideal for kinematical observations.

3.2.1 Setup

As mentioned in Section 3.1, the simulations are scale-free. Therefore, it is necessary to re-scale the simulation outputs to physical units before using them as input into the radiative transfer code. A central star of $1 M_\odot$ is assumed, and the density and velocity fields of the hydrodynamical simulation are re-scaled to $R_0 = 100$ au (i.e., one code unit is re-scaled to 100 au), and then used as input into RADMC-3D. To improve the performance, we volume-average the simulation data onto a coarser grid, halving the grid resolution for the radiative transfer post-processing. We also extended our disk, including an inner disk that goes from 10 au to the simulation grid's inner edge of 40 au, that follows the equilibrium solution used as the initial condition in the simulation (see equations 4.1 and 4.2). Therefore, our disk model extends from 10 to 250 au. Additionally, we set the gas density of the model so the total gas mass of the disk in molecular hydrogen is $0.05\,M_\odot$ in Chapter 4,

[4] http://www.ita.uni-heidelberg.de/~dullemond/software/radmc-3d
[5] https://github.com/charango/fargo2radmc3d

which result in a gas surface density of ~ 3 g cm^{-2} at 100 au. In Chapter 5, the total gas mass of the disk is lowered to prevent tracing the grid cells close to the simulation's edge in colatitude.

The disk temperature is computed via dust thermal Monte Carlo and assume that gas and dust have the same temperature. However, since our simulations are gas only, the dust is included manually, adopting a constant gas-to-dust mass ratio of 100. The dust is composed of 60 % astrosilicates (Draine & Lee, 1984) and 40 % amporphous carbon (Li & Greenberg, 1997). The optical constant of the mixture was calculated using the Bruggeman mixing formula, with a resulting intrinsic density of $2.7\,\mathrm{g\,cm^{-3}}$. Mie theory was used to compute the dust opacities (Bohren & Huffman, 1983). In the models of Chapter 4, the dust size distribution is defined adopting 10 logarithmically spaced dust size bins, with sizes ranging between a minimum of $0.01\,\mu$m, and a maximum of 1 cm. The dust size distribution follows a power-law profile $n(s) \propto s^{-p}$ with $p = 3.5$, in which the mass in the i-th size bin is $M_{d,i} = \chi M_{gas} \times s_i^{4-p} / \sum_i s_i^{4-p}$, with s_i the size of the i-th dust bin, $\sum_i$ denotes a sum over all bins, $\chi = 0.01$ the dust-to-gas mass ratio and $M_{gas} = 0.05\,M_\odot$ the gas mass in the disk model (see also Baruteau et al., 2019). We adopted a simplified dust vertical settling prescription in which the dust smaller than $10\,\mu$m has the same scale height as the gas, whereas the dust with sizes larger than $10\,\mu$m is settled towards the midplane, with the dust scale height of the i-th dust size bin following: $H_{d,i} = \Lambda H_g (s_i/s_{min})^{-0.1}$, where H_g is the scale height of the gas and s_{min} is the minimum dust size in the model. The settling parameter Λ is set to 0.2, selected to roughly match our mm-sized dust scale height with constraints from observations (e.g., Pinte et al., 2016; Villenave et al., 2020). The adopted dust scale heights are comparable to the obtained using standard diffusion models (e.g., Dubrulle et al., 1995) for the disk-averaged vertical alpha in our simulation $\alpha_{z\phi} \sim 5.1 \times 10^{-4}$, computed for one hemisphere of the disk following Eq. 4 in Stoll, Moritz H. R. et al. 2017. Global simulations of the VSI that including dust and gas dynamics constrain larger dust scale heights due to the vertical mixing produced by the VSI vertical motions (Stoll & Kley, 2016; Flock et al., 2017, 2020). Nevertheless, in our models a different vertical distribution of dust would only change the vertical temperature gradient of the disk in our radiative transfer predictions, which would have a small effect on the observable kinematic signatures.
In Chapter 5, the approach described above is simplified to speed-up the

calculations by assuming only one representative dust size bin, and limiting its maximum size to 10 μm, following the same distribution as the gas. In addition, the dust opacity is slightly reduced to $2.0\,\mathrm{g\,cm^{-3}}$, giving a total disk mass in dust of 5×10^{-5}. The resulting temperature structure is not significantly affected by these changes.

We assume that the central star emits as a perfect Black-body with an effective temperature of $T_* = 7000\,\mathrm{K}$ and a has a radius of $R_\star = 1\,R_\odot$. The obtained midplane temperatures roughly matches the used in the hydrodynamical simulations, which follows a power law $\propto R^{-0.5}$, with R the cylindrical radius. Given the assumed central star, the midplane temperature goes from ~ 40 K at 40 au to ~ 16 K at 250 au. The dust is not included in the image ray-tracing to avoid optical depth effects produced by the dust continuum in the line emission, since dust-gas simulations are required to properly model these effects. We use 10^9 photon packages to compute the dust temperature via thermal Monte Carlo and 10^8 photon packages for the image ray-tracing. In Chapter 4 we only consider absorption opacities, while in Chapter 5 we also consider scattering opacities, assuming Henyey-Greenstein anisotropic scattering.

For the molecular abundances, a constant fraction of ^{12}CO relative to H_2 of 1×10^{-4} its assumed. To obtain the abundance of ^{13}CO and C^{18}O isotopologues, the ^{12}CO abundance its scaled with the ISM isotope ratios $[^{12}\mathrm{C}]/[^{13}\mathrm{C}] \sim 77$ and $[^{16}\mathrm{O}]/[^{18}\mathrm{O}] \sim 560$, respectively (Wilson & Rood, 1994). The line emission is computed assuming local-thermodynamic-equilibrium (LTE). The molecular data is from the LAMDA[6] database (Schöier et al., 2005). Variations of CO abundance from photo-dissociation are not included in our models, while a simplified freeze-out is included in Chapter 5, by reducing the CO abundance in cold regions ($T \leq 21$ K). Although we omit the effect of CO freeze-out in Chapter 4, the dust temperature obtained via thermal Monte Carlo shows a vertical gradient, leading to stronger emission in the upper layers.

Using the molecular abundance fraction above, we generate sets of 3D grids of CO number density, and the three components of the velocity. Finally, as mentioned above, the gas temperature cube is constructed assuming the same temperature as the dust, computed via dust thermal Monte Carlo.

As the gas motions produced by the VSI are roughly axisymmetric, only

[6] https://home.strw.leidenuniv.nl/~moldata/

effects of varying the disk inclination are studied, while keeping the disk position angle (PA) fixed. We assume a distance to the source of 100 pc.

The synthetic data cubes are computed with a fine velocity resolutions of 10 m s^{-1}. Then, we average these to obtain data cubes with a coarser resolution, matching the velocity resolutions observable with ALMA and mimicking the telescope limitations without including artificial micro-turbulence. The later data cubes are used to simulate the ALMA observations, described in the following Section.

I present a summary of the parameters used in the radiative transfer predictions of this thesis in Table 3.3.

3.2.2 Simulated Observations

To predict how the synthetic images of the models would look in an interferometric ALMA observation, I simulate mock observations with the Common Astronomy Software Applications package (CASA; McMullin et al. 2007), the main data processing software for the Atacama Large Millimeter/submillimeter Array and other radio observatories. From the different versions, in Chapter 4 I used version 5.6, while in Chapter 5 I used version 6.4, both publicly available[7].

The simulated observations are computed in three steps, the simulation of the observed visibilities, inclusion of noise and cleaning of the dirty image.

First, we use the task `simobserve` to simulate the observed visibilities using our RAW synthetic data cubes as input image used to model the sky. The uv-coverage is computed for a combination of two antenna configurations, one extended and one compact, in which the integration of the compact configuration is roughly $22\% - 23\%$ of the extended one, as described in the ALMA proposers guide. The combination of two different antenna configuration is to cover both short and long baselines in the uv-plane, in order to recover information from large and small spatial scales, respectively. Long on-source integration times (≥ 10 h) are used in the set of simulated observations, in order to have good uv-coverage, crucial for a final image with good fidelity to extract the kinematical information. Furthermore, such long integrations are also needed due the difficulty to get fairly good signal-to-noise in high resolution (spatial and spectral) CO observations.

Second, we use the task SM.CORRUPT() (simulator.corrupt) to corrupt the

[7] https://casa.nrao.edu/index.shtml

simulated data, adding errors in the visibilities. We include errors with an RMS in mJy/beam corresponding to our assumed long integration times, calculated using the ALMA sensitivity calculator[8]. Note that these noise calculations assume particular atmospheric conditions, that significantly affect the time required to reach a particular sensitivity.

Third, I applied the CASA `tclean` to reconstruct the image from the modeled dirty image visibilities, following the CLEAN algorithm. In this process, I used the multi-scale mode and a briggs weighting scheme. Moreover, I used the non-interactive Automasking (auto-multithresh; Kepley et al. 2020), which automatically generates the masks used during the cleaning process. Such automatic masking is possible due the known morphology of the emission from the radiative transfer models; however, in real observations masking the image manually is recommended. As a final product cleaned spectral cube with expected artifacts from real ALMA observations is obtained.

3.3 Kinematic Analysis Tools

The kinematic signatures of the synthetic predictions are extracted in two steps. First, the line-of-sight velocity map is computed from the data cube (also referred as velocity centroid line maps, see Section 2.3). Second, the best fit Keplerian model to the line-of-sight velocity map is found, which when subtracted to the original reveals the structure of the non-Keplerian gas flows.

3.3.1 Line Centroid Maps

For the first step, we compute velocity centroid maps (v_0) from the ALMA simulated data cubes using a Gaussian function to fit the CO line emission in each pixel. For this we use the publicly available Python package BETTERMOMENTS[9] (Teague & Foreman-Mackey, 2018; Teague, 2019). This package robustly computes the centroid maps of spectral line data for a variety of methods, and their respective statistical uncertainties. A Gaussian function is chosen as it gives the best results for the synthetic models, which is expected since the emission lines in the radiative transfer code are also modeled as a Gaussians.

[8] https://almascience.eso.org/proposing/sensitivity-calculator
[9] https://github.com/richteague/bettermoments

Among the options, the most accurate for optically thin lines are Gaussian and quadratic fits, while Gaussian Hermite can be used for more optically thick lines. In addition, the traditional methods to compute statistical methods (e.g., First and Ninth Moment methods are available).

Alternative methods can be also applied in this step, for example fitting a quadratic function or a Gaussian Hermite. In addition, the traditional methods to compute statistical methods (e.g., Zeroth and First Moments), and the Ninth Moment method are available in BETTERMOMENTS. In order to apply the fitting of a quadratic or Gaussian function, a high average signal-to-noise observation is needed for the methods to work properly; however, are required to have precise results. Moreover, the use of these higher precision methods (quadratic or Gaussian) are needed to accurately extract the line-of-sight velocity of the upper emission surface only, without mixing information from both emission layers. On the contrary, the widely used First Moment map (as implemented in CASA) can have contributions from the upper and lower CO layers, that could result in a incorrect interpretation of the kinematical structure of the disk. Further, the First Moment map results would be inconsistent with the following step of fitting the upper emission surface to find the best Keplerian model, since the model fitting assumes that the information comes from one layer only. Nonetheless, the method used to extract the line-of-sight velocity map on real observations will depend on the particular quality of the observations, traced molecule, and disk geometry.

3.3.2 Finding the best Keplerian model

Following, we extract the velocity perturbations of the projected velocity into the line-of-sight image. For this purpose we use the Extracting Disk DYnamics Python suite EDDY[10] (Teague, 2019a) to obtain the best fitting Keplerian disk model for the ^{12}CO velocity centroid maps of the simulated ALMA observations.

I used a model that assumes a geometrically thick disk with an elevated emission surface, in which the emitting surface is parameterized by:

$$z(r) = z_0 \times \left(\frac{R}{1''}\right)^{\psi} \times \exp\left(-\left[\frac{R}{R_{\rm taper}}\right]^{q_{\rm taper}}\right), \tag{3.4}$$

[10] https://github.com/richteague/eddy

where R is the disk cylindrical radius, ψ dictates the flaring of the emission surface, and z_0 and R_{taper} the reference disk aspect ratio and exponential taper reference radius. The exponential taper mimics a drop of the emission height seen in observations (e.g., Teague et al. 2021).While in Chapter 4 such exponential taper is included, I found that it was not optimal for our models; therefore, in Chapter 5 I assumed the limit $R_{taper} = \infty$, reducing the number of free parameters.

For the fitting of the disk rotation in Chapters 4 and 5, I used two different options available in EDDY.

In Chapter 4 I used the more flexible option, in which the fitting also includes a global contribution of the radial velocity component, where both the disk rotation curve and radial velocity follow a power-law profile:

$$v_\phi = v_{\phi,100} \times \left(\frac{R}{100\,\text{au}}\right)^{v_{\phi,q}} \tag{3.5}$$

$$v_R = v_{R,100} \times \left(\frac{R}{100\,\text{au}}\right)^{v_{R,q}}, \tag{3.6}$$

with R the cylindrical radius, and $v_{R,100}$ and $v_{\phi,100}$ the disk radial and azimuthal velocity at 100 au from the star. This approach allows a rotation curve that follows a rotation curve slightly different from Keplerian, being sub-Keplerian in my models due the contribution from the global pressure gradient and the disk being not self-gravitating.

Following, the disk velocity model projected into the line of sight considering the contributions of both radial and azimuthal velocity components:

$$\text{v}_{mod} = v_\phi \cdot \cos\phi \cdot \sin i + v_R \cdot \sin\phi \cdot \sin i + v_{LSR}, \tag{3.7}$$

where ϕ is the polar angle of the pixel (measured east of north relative to the red-shifted major axis) and v_{LSR} is the systemic velocity. In this flexible approach, the free disk parameters are the disk position angle, systemic velocity, disk center, the radial and azimuthal velocity at 100 au from the star, the slope of the radial and azimuthal velocity power-law profiles, and emission surface parameters (z_0, ψ, R_{taper} and q_{taper}). We fix the distance to the source to 100 pc and the disk inclination equal to the value used to compute the input data cube. Then, a series of MCMC chains are run to

find the parameters of the best fit (sub-)Keplerian model for the geometrically thick disk. In this case, I use 128 walkers that take 2000 burn-in steps and additional 500 steps to sample the posterior distributions for the model parameters. A delimited radial region of the disk is considered in the model fitting, set to [0.55,2.0], [0.58,1.85] and [0.6,1.7] arcseconds for inclinations of 5, 25 and 35 degrees, respectively. Finally, the velocity perturbations are extracted by subtracting the velocity centroid map of the best fit disk model (v_{mod}) to the original (v_0).

In Chapter 5 we applied a different approach for fitted rotation curve, since I found very similar results as the presented in Chapter 4 with fewer free disk parameters. In this case, the rotation curve follows a Keplerian profile accounting the altitude of the emission height:

$$\mathrm{v}_{Kep} = \sqrt{\frac{GM_{star}R^2}{(R^2+z^2)^{3/2}}}, \tag{3.8}$$

with M_{star} the mass of the central star. The fitting is run as described above, but with fewer free parameters (M_{star}, disk PA, z_0, ψ,v_{LSR}, x_0, y_0), again fixing the disk inclination to the input model inclination and the distance to the system to 100 pc. The projected line-of-sight velocity in the later case do not include the radial velocity component; therefore, follows:

$$\mathrm{v}_{mod} = v_{Kep} \cdot \cos\phi \cdot \sin i + v_{LSR} \tag{3.9}$$

Again, both approaches give similar results, and the application to real observations would depend on the target's emission surface geometry and the constrained parameters.

An alternative way to look at the disk kinematic structure is to obtain an azimuthally averaged view of the disk velocities (radial profiles); however, in this thesis I only study the two-dimensional view of the deviations from Keplerian rotation. In principle, I could exploit the axis-symmetry of the VSI flows with such approach, while also boosting the signal-to-noise of the simulated observations, reducing the observing time needed to extract the velocity perturbation. Unfortunately, there is a degeneracy between the flows produced by the VSI and a massive planet when exploring the radial velocity profiles of the upper CO emission layer only. Moreover, the extraction of the radial profiles is extremely sensitive to systematic errors, and more com-

putationally expensive. Finally, I highlight that alternative tools to BETTERMOMENTS and EDDY are also publicly available, such as GMoments[11] (Casassus & Pérez, 2019) and Discminer (Izquierdo et al., 2021, 2022). Differences between methods can be found in terms of flexibility of the models, specific applications or to suit a particular target (see e.g., Disk Dynamics Collaboration et al. 2020).

[11] https://github.com/simoncasassus/GMoments

Symbol	Definition	Description
r,θ,ϕ		spherical coordinates
R,ϕ,Z		cylindrical coordinates
ρ		gas density
H	c_s/Ω_K	disk pressure scale height
h	H/R	disk aspect ratio
P		pressure
c_s		isothermal sound speed
p		slope of the radial density profile
q		slope of the radial temperature profile
v_r,v_θ,v_ϕ		radial, meridional and azimuthal velocities
v_K	$\sqrt{GM_\star/R}$	Keplerian azimutal velocity
Ω_K	$\sqrt{GM_\star/R^3}$	Keplerian angular frequency
$R_{r,\phi}$,$R_{z,\phi}$		Reynolds stresses in radial and vertical directions
$\alpha_{r,\phi}$,$\alpha_{z,\phi}$		Stress over pressure ratios in radial and vertical directions
α		constant alpha viscosity parameter
ν	$\alpha c_s H$	artificial viscosity following alpha prescription
v_0		velocity in the line of sight
v_{Kep}		rotation curve of a Keplerian disk
v_{eq}		velocity in the line of sight of a disk in equilibrium
v_{mod}		velocity in the line of sight of the best fit disk model
z_0		reference geometrical surface height (aspect ratio)
ψ		flaring of the model emission surface
v_{LSR}		disk systemic velocity

Table 3.1: Summary of symbols used in this thesis.

Parameter	Value (Chapter 4)	Value (Chapter 5)
Reference radius	100 au	100 au
Aspect ratio at 100 au	0.1	0.1
Flaring index	0.25	0.25
Surface density slope	-1.0	-1.0
Temperature slope	-0.5	-0.5
Stellar mass	1.0 $M_\odot$	1.0 $M_\odot$
# of cells in r	512	512
# of cells in ϕ	1024	1024
# of cells in θ	128	192
Grid inner radius	0.4 (40 au)	0.4 (40 au)
Grid outer radius	2.5 (250 au)	2.5 (250 au)
Grid domain in colatitude	$\pi/2 \pm \pi/7.4$	$\pi/2 \pm \pi/6.8$
Inner buffer zone Radius	0.48 (48 au)	0.5 (50 au)
Outer buffer zone Radius	2.1 (210 au)	2.1 (210 au)
Damping timescale	$0.3\Omega_K$	$0.1\Omega_K$

Table 3.2: Summary of the parameters used in the simulations of Chapters 4 and 5.

Parameter	Value (Chapter 4)	Value (Chapter 5)
Stellar radius	$1.0\,R_{\odot}$	$1.0\,R_{\odot}$
Stellar effective temperature	7000 K	7000 K
Distance	100 pc	100 pc
Disk total gas mass	0.05 $M_{\star}$	0.01 $M_{\star}$
Disk total dust mass	5×10^{-4}	5×10^{-5}
Maximum dust size	1 cm	10 μm
Minimum Dust Size	0.01 μm	0.01 μm
Dust size slope	-3.5	-3.5
Dust intrinsic density	2.7 g cm^{-3}	2.0 g cm^{-3}
Number of Dust Size Bins	10	1
Disk inclination	[5°,20°,35°]	[5°,15°,30°]

Table 3.3: Summary of the parameters used in the radiative tranfer predictions presented in Chapters 4 and 5.

4 Observational signatures of the vertical shear instability in protoplanetary disks CO kinematics

The content of this chapter is an adapted version of the the published research article *"Observability of the vertical shear instability in protoplanetary disk CO kinematic"* (Barraza-Alfaro et al., 2021).

4.1 Introduction

The main objective of the research project presented in this Chapter is to study the observability of the gas velocity structure produced by the vertical shear instability (VSI) in CO kinematics observations with the Atacama Large Millimetre/submillimetre Array[12] (ALMA). For this purpose, we performed global 3D high-resolution hydrodynamical simulations of an inviscid and locally isothermal disk unstable to the VSI. We post-processed the simulation results with radiative transfer calculations and produced synthetic predictions of CO emission lines. Next, we computed the line of sight velocity map and its deviations from a disk following a Keplerian equilibrium solution, in order to predict their expected kinematical signatures. Finally, we explored the potential of detecting these VSI induced kinematical signatures by simulating ALMA observations, and extracting the kinematical signatures by fitting a geometrically thick Keplerian disk model to the line of sight velocity maps. I address which spatial and spectral resolutions are needed to robustly characterize VSI kinematic signatures, and how their identification would add constraints on the disk physical properties. Especially the morphology of the observable large scale VSI motions in gas kinematics that may support or discard the VSI operating in planet-forming disks.
In this chapter I start by presenting the hydrodynamical simulations results. Following, I show the radiative transfer images and simulated observations.

[12] https://www.almaobservatory.org/

I discuss our main findings in Section 4.4. Finally, I summarize our work and draw our conclusions in Section 4.5.

4.2 Hydrodynamical Simulations

In the present Section, I first describe in Section 4.2.1 the physical model used as initial condition for the simulations. Then, the results are shown and described in Section 4.2.2. For a detailed description of the numerical methods used for the simulations see Section 3.1.

4.2.1 Physical model

We adopted the physical model of the disk from Nelson et al. (2013). The physical model is described using cylindrical coordinates (R,Z,ϕ). The hydrodynamical simulations described in Section 4.2 are performed in spherical coordinates (r,θ,ϕ). As initial conditions, we construct a set of 2D axisymmetric profiles for the density and rotation velocity that fulfill hydrostatic equilibrium. The initial conditions for density and angular velocity are given by the equilibrium solutions:

$$\rho(R,Z) = \rho_0 \left(\frac{R}{R_0}\right)^p \exp\left(\frac{GM}{c_s^2}\left[\frac{1}{\sqrt{R^2+Z^2}} - \frac{1}{R}\right]\right), \tag{4.1}$$

$$\Omega(R,Z) = \Omega_K \left[(p+q)\left(\frac{H}{R}\right)^2 + (1+q) - \frac{qR}{\sqrt{R^2+Z^2}}\right]^{1/2}, \tag{4.2}$$

where Ω_K is the Keplerian angular velocity $\Omega_K = \sqrt{GM/R^3}$, $H = c_s/\Omega_K$ is the local disk scale height, c_s the local sound speed, R_0 is the reference radius, set to be equal to the code unit of length, and p and q are the power-law profiles for the density and temperature. ρ_0 sets the value of the gas midplane density at $r = R_0$. The gas in our simulation is described by a locally isothermal equation of state, that is $P = \rho c_s^2$. The isothermal sound speed is proportional to the temperature, $c_s^2 \propto T$. Therefore, q also represents the radial power-law index of $c_s^2(R)$:

$$c_s^2(R) = c_0^2 \left(\frac{R}{R_0}\right)^q. \tag{4.3}$$

The disk pressure scale height follows:

$$H(R) = H_0 \left(\frac{R}{R_0} \right)^{(q+3)/2}, \tag{4.4}$$

where H_0 is the disk scale height at the reference radius R_0, set such that $H_0/R_0 = 0.1$. In our simulations the midplane density slope is $p = -1.0$, while the temperature slope is $q = -0.5$, resulting in a flared disk with a flaring index of 0.25. Looking at the last term of the prescription given in equation 4.2, we observe that for the same cylindrical radius the upper layers of the disk have slower angular velocity than the midplane; that is, the disk has a vertical shear, which sets the instability in our simulations.
The same disk physical model is also used for the Simulations presented in Chapter 5.

4.2.2 Simulation results

Figure 4.1 shows the temporal evolution of the $\alpha_{r\phi}$ value consisting of the radial Reynolds stress-to-pressure ratio. We determine $\alpha_{r\phi}$ using the pressure-weighted stress-to-pressure ratio

$$\alpha_{\mathrm{r}\phi} = \frac{\int \mathrm{T}_{\mathrm{r}\phi} \mathrm{dV}}{\int \mathrm{P dV}} = \frac{\int \rho \mathrm{v}'_\phi \mathrm{v}'_\mathrm{r} \mathrm{dV}}{\int \rho \mathrm{c}_\mathrm{s}^2 \mathrm{dV}}, \tag{4.5}$$

with the volume dV, and v'_ϕ and v'_r representing the turbulent components of the velocities are determined by subtracting the azimuthally averaged value at each r and θ. Fig. 4.1 shows the time evolution, with a growth from very small values (we set the initial radial and vertical velocities to zero) until reaching a saturated value after around 170 orbits of evolution with $\alpha_{r\phi} \sim 1.4 \times 10^{-4}$. For the further post-processing we use a snapshot after 300 orbits. A 3D plot showing the 3D gas dynamics of the disk is shown in Fig. 4.2.

As a next step, we present detailed horizontal and vertical 2D plots out of the 3D dataset using the same snapshots after 300 orbits (measured at the code unit of length). These 2D plots are shown in Figure 4.3. The fields have been computed re-scaling the code unit of length to 100 au, and considering a central Solar-mass star, therefore, the snapshot corresponds to a disk evolution time of ∼0.3 Myr. Each row represents snapshots of the midplane, top row, at three scale heights middle row, and a vertical cut in the R-Z plane.

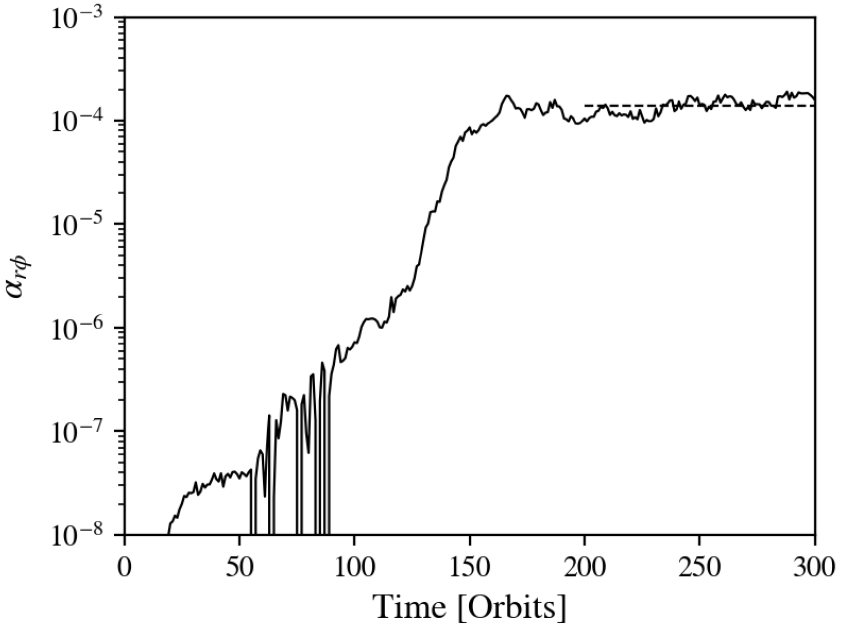

Figure 4.1: Time evolution of the stress-to-pressure ratio $\alpha_{r\phi}$ of the VSI-unstable 3D hydrodynamical simulation. We show the time evolution in units of the orbital timescale at $R = 100\,\mathrm{au}$. The dashed line indicates the time-averaged value of $\alpha_{r\phi}$ between 200 and 300 orbits.

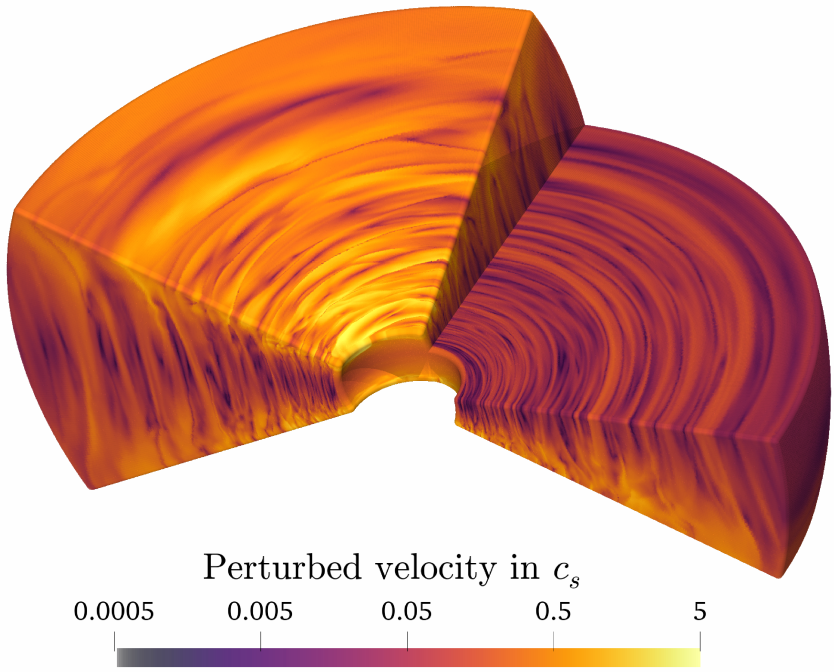

Figure 4.2: 3D rendering of a VSI-unstable protoplanetary disk. The color map shows the perturbed total velocity of the gas in units of the local sound speed. Only a part of the simulation domain is shown for visualization purposes.

The four columns present density and the three velocity components. In the left column of Fig. 4.3, we plot the gas density perturbations, $(\rho - \rho_0)/\rho_0$. At the midplane and upper layers we see a turbulent structure with spirals and ring-like structures. At the midplane the density deviations are on a level of several percent of the background value. At the upper layers of the disk the density deviations reaches levels of up to 30%. We note that even though the fluctuations are strong in the upper layers, there is no particular morphology that could be easily identified as VSI-generated.
Figure 4.3, right columns, show the 3D velocity structure typical of a disk in which the VSI is active in its saturated state. Strong perturbations are present in the three velocity components. Similarly, very turbulent structures are present in the azimuthal velocity deviations from a disk in sub-Keplerian rotation (expected from an unperturbed disk) at the midplane. Close to the surface, however, axisymmetric rings are visible. Interestingly, in some of these rings the rotation is sub-Keplerian in one hemisphere while super-Keplerian in the other. We also note that similar to the radial perturbations, the azimuthal ones are also weakest in the midplane with values of around 10's meters per second while they become larger at the upper layers.
We summarize that the density perturbations, radial velocity perturbations and the azimuthal velocity deviation from a disk in Keplerian rotation are weak close to the disk midplane, however, above three pressure scale heights they can reach up to 100's of meters per second.
Even more interesting are the meridional velocity motions, seen in Fig. 4.3 third column. There are prominent large scale motions through the whole vertical extent of the disk reaching velocities of around 50 meters per second. These motions are mostly axisymmetric, and therefore they show a clearer signature compared to the radial and azimuthal components.

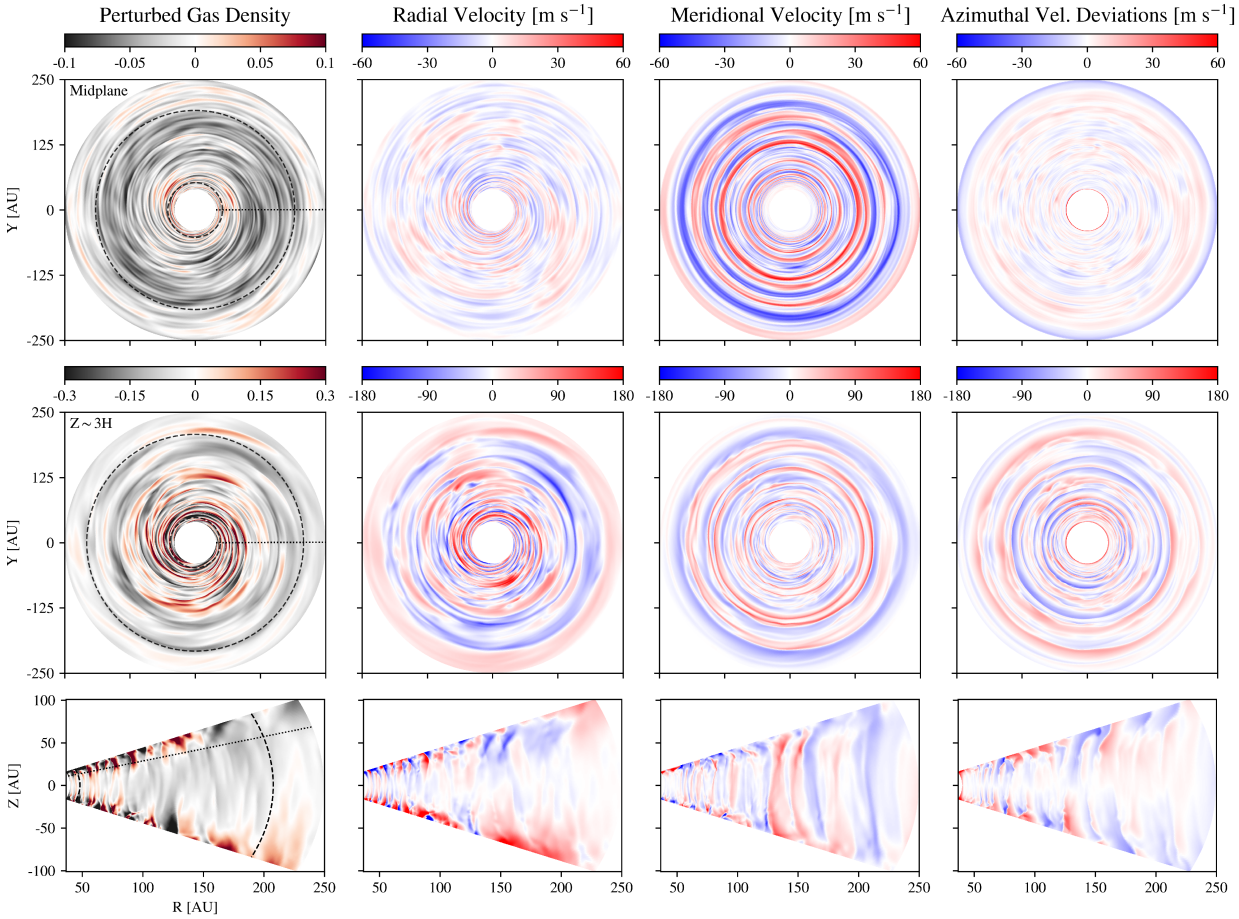

Figure 4.3: Results of the VSI-unstable disk 3D hydrodynamical simulation. The panels show snapshots of the density and the velocities, taken after 300 orbital periods. *From left to right*: Perturbed gas density, radial velocity, meridional velocity, and azimuthal velocity deviations from a sub-Keplerian velocity equilibrium solution. The velocity values are in physical units, where the simulation code unit of length is re-scaled to 100 au, and the central star is a Solar-mass star. *From top to bottom*: r-ϕ slices of the fields at the disk midplane, r-ϕ slices of the fields at approximately three pressure scale heights ($3H$) above the midplane, and r-θ slices of the fields. In the left-most column plots, the circles in dashed lines indicate the location of the inner and outer buffer zones. The dotted lines in the r-ϕ slices indicate the azimuth where the r-θ slice is taken, while in the r-θ plots the dotted line indicates the location where $z \sim 3H$.

4.3 Radiative Transfer Post-processing Results

In this Section I present the radiative transfer images computed from the post-processing of the simulations results shown in Section 4.2.2, simulated observations of these synthetic images (see Section 4.3.1), and the extracted non-Keplerian kinematical signatures (see Section 4.3.2). For a detailed description of the numerical tools used in these calculations see Section 3.2.
For the images presented in the present Chapter, we chose to compute predictions of the emission of the J=2-1 transition for the three CO isotopologues, ^{12}CO centered at ≈ 230.538 GHz, ^{13}CO centered at ≈ 220.399 GHz, and C^{18}O centered at ≈ 219.560 GHz. All three transitions are observable with ALMA Band 6. We compute predictions for three different inclinations: 5°,25° and 35°, while keeping the PA fixed to 90° east-of-north.
We compute the synthetic cubes to have a total bandwidth of 6 km s^{-1}, with 600 channels of 0.01 km s^{-1}. Then, we average these to obtain data cubes with a resolution of 0.05 km s^{-1}, that is the current maximum resolution of ALMA in Band 6, that we use in the analysis.
In the synthetic images, the disk near side is the south, and its rotation is counter-clockwise with respect to the observer. The total integrated flux of the ^{12}CO$(2-1)$, ^{13}CO$(2-1)$ and C^{18}O$(2-1)$ synthetic data cubes are approximately 42, 23 and 13 Jy km s^{-1}, respectively.
For a first approximation of a synthetic observation, we convolved the raw resulting synthetic channel maps by a circular-Gaussian beam, and study the addition of noise following the white noise model implemented in FARGO2RADMC3D (see also Baruteau et al. 2019). A mask of 0.42 arcseconds (42 au) was applied to all raw images to remove the emission from the disk regions close to the simulation's inner edge.
Additional data cubes varying the velocity resolution and spatial resolution are computed to explore the dependency of our results with resolution which we discuss in Section 4.4.3. The emission of four different velocity channels convolved by a circular Gaussian beam of 50 mas (5 au) is shown in Figure 4.4, for each disk inclination. It is readily seen that the VSI produces velocity perturbations in individual channels, seen as a corrugated pattern at the edges of the emission, more prominent with decreasing disk inclination.

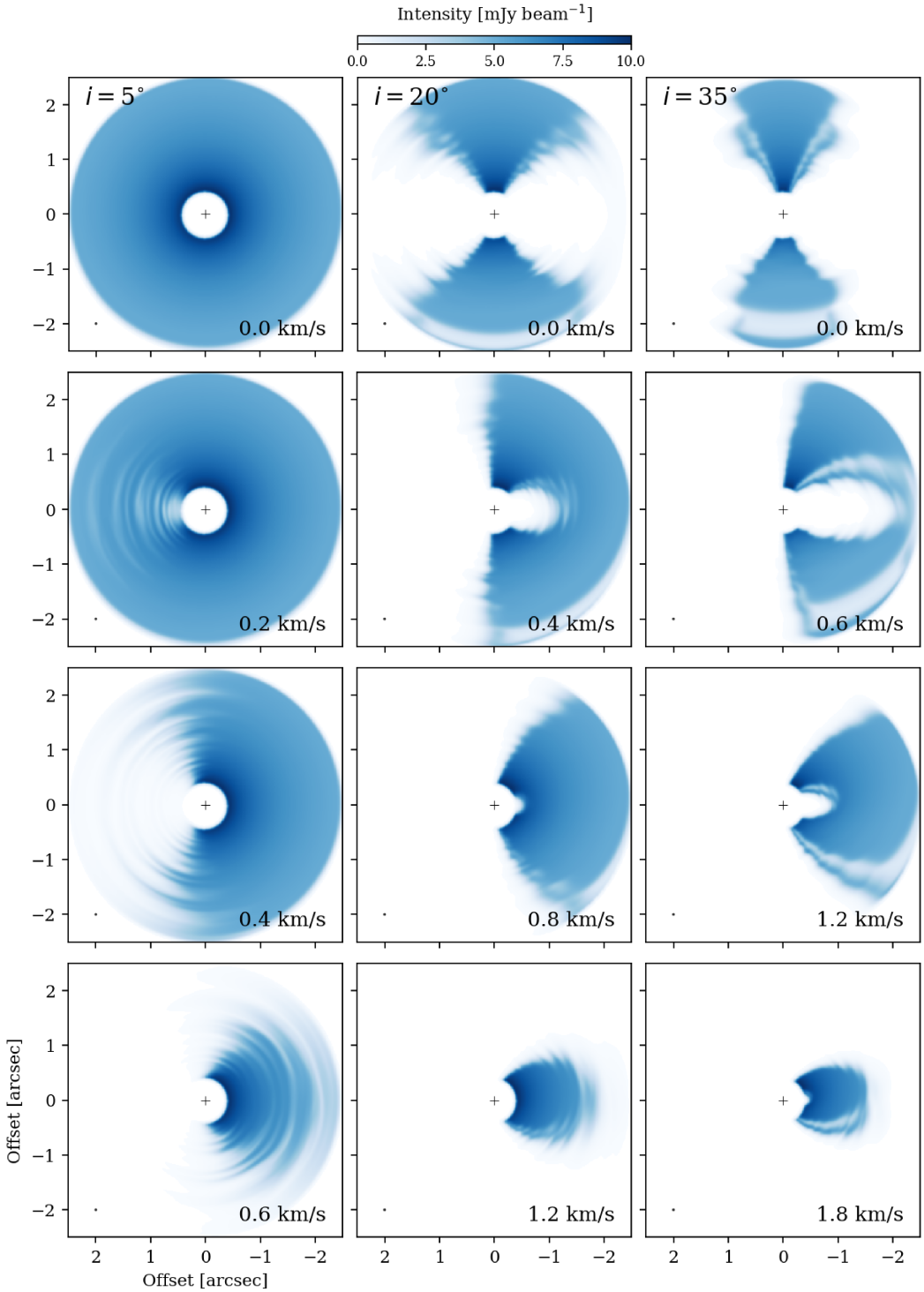

Figure 4.4: Predictions of the ^{12}CO disk emission of a VSI-unstable disk for different velocity channels. From left to right, the columns correspond to predictions for disk inclinations $i = 5$, 20 and 35 degrees. The channel widths are 0.05 km s^{-1}. The images are convolved with a circular Gaussian beam of 50 mas, shown in the bottom-left corner of each panel. The disk emission shows a corrugated pattern. Only red-shifted channels are shown, as the structures are quasi axisymmetric, therefore, the symmetric blue-shifted channels show similar substructures.

4.3.1 ALMA synthetic observations

We use our ^{12}CO$(2-1)$ synthetic data cubes as input to `simobserve`. We simulate a 20 h integration in configuration C43-8 (8.5 km longest baseline) combined with a 4.4 h integration in C43-5 (1.4 km longest baseline). Then, we corrupt the visibilities to obtain a RMS of ~ 1.5 mJy beam^{-1} in each channel. This noise level is the expected RMS for a precipitable water vapor (PWV) of 0.9 mm and 20 h of integration time. Finally, we compute final CLEANed spectral cubes with `tclean` using briggs weighting with robust parameter 1.0, resulting in a synthesized beam with a FWHM of $\sim 80 \times 60$ mas (8×6 au). The average signal-to-noise per beam and channel is ~ 10 at ~ 100 au from the central star, and larger than 5 in all the disk. Such sensitivity level is ideal for kinematic analysis, and recover the non-Keplerian coherent substructures. Further details on the simulated observations are presented in Section 3.2.2.

4.3.2 Deviations from a sub-Keplerian disk model

The line of sight velocity maps, and extracted velocity deviations from a sub-Keplerian disk for three different disk inclinations (5°, 20° and 35°) are shown in Figure 4.5. The maps are computed for line emission data cubes with a velocity resolution of 0.05 km s^{-1}. In the first column, the line centroid at each pixel is presented as the disk velocity in the line of sight (v_0), for images convolved by a circular Gaussian beam of 50 mas. Substantial deviations from the typical pattern from an inclined sub-Keplerian disk are already noticeable in the low inclination case. The following columns show the extracted velocity perturbations, which are seen as quasi axisymmetric rings that reach magnitudes of ~ 50 m s^{-1}. The substructures become more complex as we increase the disk inclination. In the second column, we present the velocity perturbations obtained when we subtract to v_0 shown in the first column, a second velocity centroid map computed from a synthetic observation of a smooth disk following an equilibrium solution (v_{eq}). We use here the initial conditions from the simulation as input for the radiative transfer calculations, to compute the synthetic observations of the disk in equilibrium. The resulting residual map can be used as the expected velocity perturbations in an ideal observation with 5 au resolution. In the third column, the residual of subtracting to v_0, in this case computed for a synthetic cube convolved by a 10 au circular Gaussian beam, the best fit disk model obtained

with EDDY (v_{mod}). As detailed in Section 3.3.2, the model corresponds to a geometrically thick disk, that follows power-law profiles for the velocities in the radial and azimuthal directions. The resulting residual maps are the observable velocity perturbations in a 10 au resolution observation, with the addition of white noise with an RMS level expected for a 20h long-baseline ALMA observation. Recovering properly the emission surface and velocity profiles is harder for the highest inclination case presented ($i = 35°$). We tested a higher inclination case with $i = 45°$, and we found we were unable to recover the velocity perturbations reliably. The extracted velocity perturbations match fairly well with the expected pattern for inclinations of 5 and 20 degrees. Additional modulations are present depending on the polar angle with respect to the disk's major axis for the inclination of 35 degrees case. These modulations are due to systematic differences between the fitted and the true emission surface, with a secondary contribution from the errors on the disk center, PA, and velocity profiles (see also Figure 12 in Yen & Gu 2020). In the fourth column, we applied the same procedure to extract the velocity perturbations shown in the third column, but in this case for a v_0 computed from the simulated ALMA observations described in Section 4.3.1. We observe that the perturbations are consistent with the expected VSI ringed structure, therefore, VSI-signatures are observable within ALMA capabilities.

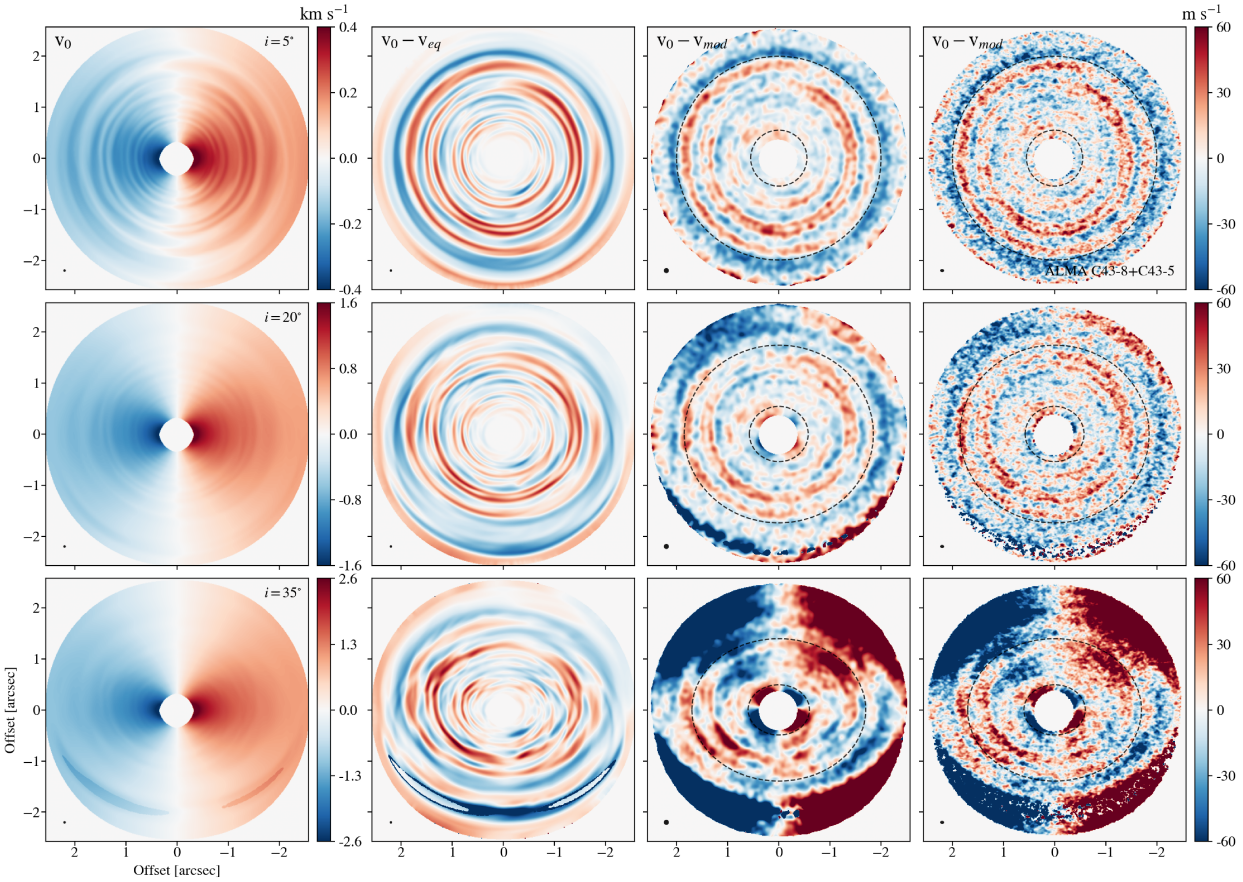

Figure 4.5: Results of the line of sight velocity map and extracted velocity perturbations from ^{12}CO(2-1) synthetic lines observations of a VSI-unstable disk. The velocity centroid of the line was computed at each pixel from mock data cubes with a velocity resolution of 0.05 km s^{-1}. The input fields are shown in Figure 4.3, which corresponds to a disk after ~ 0.3 Myr of evolution. From top to bottom, are shown the results for disk inclinations of 5°, 20° and 35°. *First column:* Velocity centroid maps (v_0). The images are convolved by a circular Gaussian beam of 50 mas and have no noise. *Second column:* Residual map of subtracting to v_0 the velocity centroid map obtained from a disk following an equilibrium solution (v_{eq}). *Third column:* Residual of subtracting to v_0 the best fit disk model obtained using Eddy (v_{mod}). The images in this case are convolved by a 0.1 arcseconds circular Gaussian beam and have an RMS noise of ~ 1.5 mJy beam^{-1}. *Fourth column:* The same as the third column, but for a 20 h Cycle 7 ALMA simulated observation using configurations C43-8 and C43-5, with an RMS noise of ~ 1.5 mJy beam^{-1}. The beam size is shown with a black circle at the bottom left of each panel. The black-dotted ellipses in panels of columns 3 and 4 are the inner and outer edge of the region considered to obtain the best fit model. The x- and y-axes indicate the R.A. and Dec. angular offset from the central star's position in arcseconds.

How the different velocity components contribute to the projected line of sight velocity (LOSV) is crucial to interpret the velocity deviations. As shown by Teague et al. 2019 (see their Figure 5), a ring of super(sub) Keplerian azimuthal motions show a sign-flip (from red- to blue-shifted, or vice versa) with respect to the PA of the disk. While for a ring of inward(outward) flow the sign flip is with respect to the line perpendicular to the disk PA. A ring of upward(downward) vertical motion, however, has the same sign for all PA. To better understand the contributions of each velocity component to the projected line of sight velocity, we computed the expected velocity perturbations considering each component separately. The synthetic data cubes were calculated using an input velocity field in which only one of the three velocity components is from a VSI unstable disk simulation and the remaining two are set to follow an equilibrium disk solution (v_{eq}). In Figure 4.6 we observe the contributions to the LOSV from the radial velocity v_r, meridional velocity v_θ and azimuthal velocity v_ϕ for different disk inclinations. It is clear that the meridional velocity dominates the LOSV. With increasing inclination, the radial and azimuthal velocities contribute more to the LOSV, where the radial velocity introduces asymmetric features in our highest inclination case. The contribution from the azimuthal velocity perturbations is minor for all the inclinations explored.

To summarize, the meridional flows from the VSI body modes are the most distinctive feature observable in the velocity centroid maps of a VSI-unstable disk. For low disk inclinations we have rings of red- or blue-shifted emission. Increasing the inclination we have a significant contribution of the radial velocity, in which the asymmetric nature of the radial perturbations adds complications to interpret the observable VSI signatures. Moreover, modulations of the extracted perturbations depending on the polar angle relative to the disk PA can appear due to the limitations of the method, making the characterization of the VSI-signatures difficult.

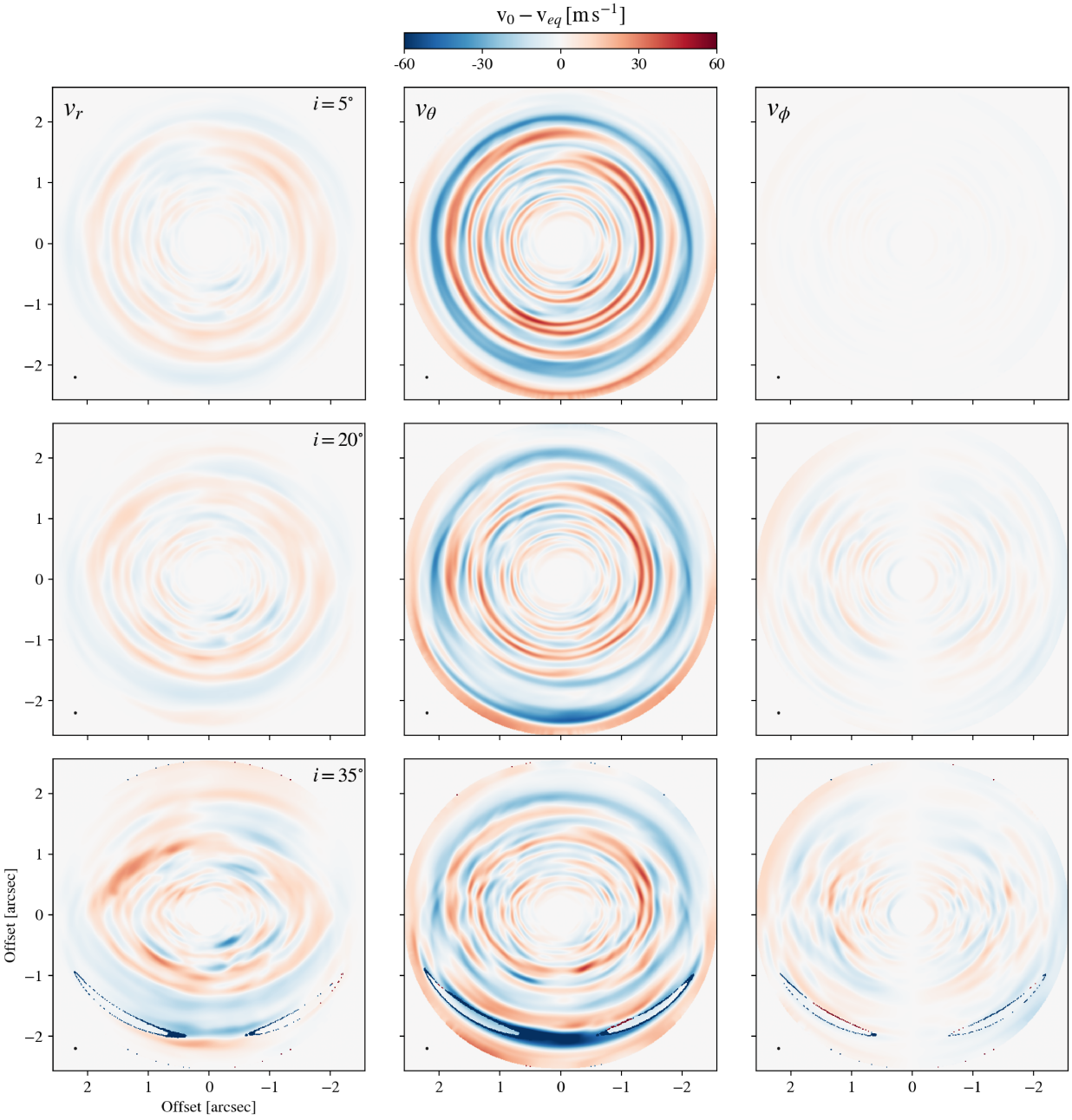

Figure 4.6: Results of the expected observable velocity perturbations from ^{12}CO synthetic lines observations, in which one of the velocity components is from a VSI unstable disk. The input VSI-active velocity field into the radiative transfer is modified to follow an equilibrium disk solution in two of the components. From left to right, the columns show predictions considering the contributions of the radial velocity, the meridional velocity and azimuthal velocity, respectively. From top to bottom, the different rows show the results for disk inclinations of 5°, 20° and 35°. The mock data cubes have a velocity resolution of 0.05 km s^{-1}, and the images are convolved by a circular Gaussian beam of 50 mas, shown at the bottom left corner of each panel. The x- and y- axes indicate the R.A. and Dec. angular offset from the position of the central star, in arcseconds.

4.3.3 Kinematic signatures for different CO isotopologues

Observing different CO isotopologues allows to study different layers of the disk and probe the dependency of the kinematic structures with disk height. To test the effect of the tracer optical depth, we run the radiative transfer calculations of our VSI unstable disk model for ^{12}CO, ^{13}CO and C^{18}O. The disk layers traced approximately by the different isotopologues are shown in Figure 4.7, where we display the layer where the disk becomes optically thick ($\tau = 1$ surface). For simplicity, the calculations of the $\tau = 1$ surfaces are computed for a disk face-on ($i = 0°$). The emission surfaces traced in our predictions, shown in Figure 4.7, roughly match with constraints from recent ALMA observations (e.g., Zhang et al., 2017; Pinte et al., 2018).

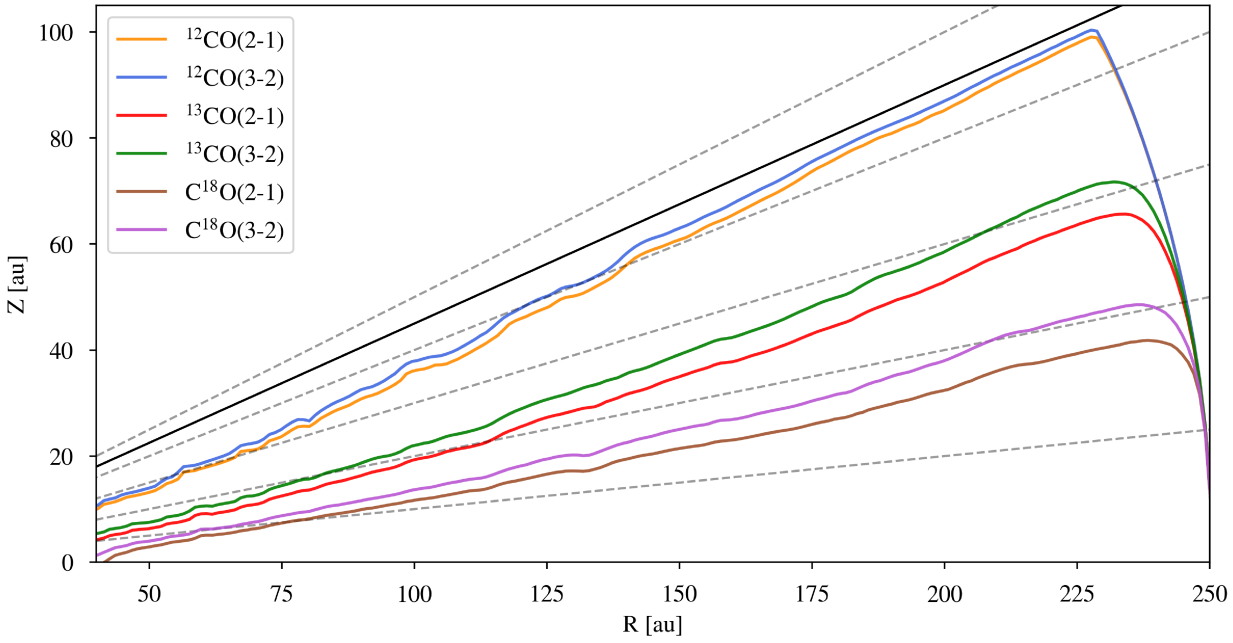

Figure 4.7: Radial profile of the disk layers where the disk becomes optically thick ($\tau = 1$ surface), for different CO isotopologues of the VSI-unstable disk radiative transfer model. We illustrate the $\tau = 1$ surface for the J:2-1 and J:3-2 transitions of three CO isotopologues, ^{12}CO, ^{13}CO and C^{18}O. We assume a face-on disk orientation for the calculation. The gray dashed lines show where $Z = AR$ for A$= 0.1; 0.2; 0.3; 0.4$ and 0.5. The solid black line shows the grid boundary in colatitude of the simulated disk, located approximately at $Z = 0.45R$.

The expected velocity perturbations from a VSI-unstable disk for the three different isotopologues is shown in Figure 4.8, for different disk inclinations. We observe that the quasi axisymmetric ring structure present in the residuals of the ^{12}CO predictions are also recovered for the ^{13}CO and C^{18}O predictions. Further, the remaining velocity residuals are feebler for optically thinner tracers, where the difference between isotopologues becomes more noticeable with increasing disk inclination. These findings are expected since the emission layer for these lines trace lower disk heights where the VSI perturbations are weaker. Moreover, the radial and azimuthal velocity components decrease faster than the vertical moving towards the midplane, as seen in the r-θ slices of the disk in Figure 4.3, where is shown that the vertical motions from the VSI body modes penetrate through the whole vertical extent of the disk. Therefore, the meridional component of the velocity perturbations is predicted to also dominate the line of sight velocity at deeper layers, resulting in the recovered quasi axisymmetric ringed morphology (as discussed in Section 4.3.2). Furthermore, the difference among tracers becomes larger for more inclined disks as the contribution to the line of sight velocity from the radial and azimuthal gas velocity increases with inclination. Additionally, the velocity structure is smeared for optically thinner tracers due to the emission arising from a larger range of heights (Zhang et al., 2017). Therefore, detecting VSI signatures in ^{13}CO or C^{18}O would require higher sensitivity, especially for inclined disks. Adding the difficulties to get high spatial resolution observations with enough signal-to-noise, we conclude that ^{12}CO is the best tracer to detect VSI signatures. Nevertheless, observing the weak dependence with disk height of the morphology and magnitude of the VSI velocity perturbations for low inclined disks is essential to confirm its origin.

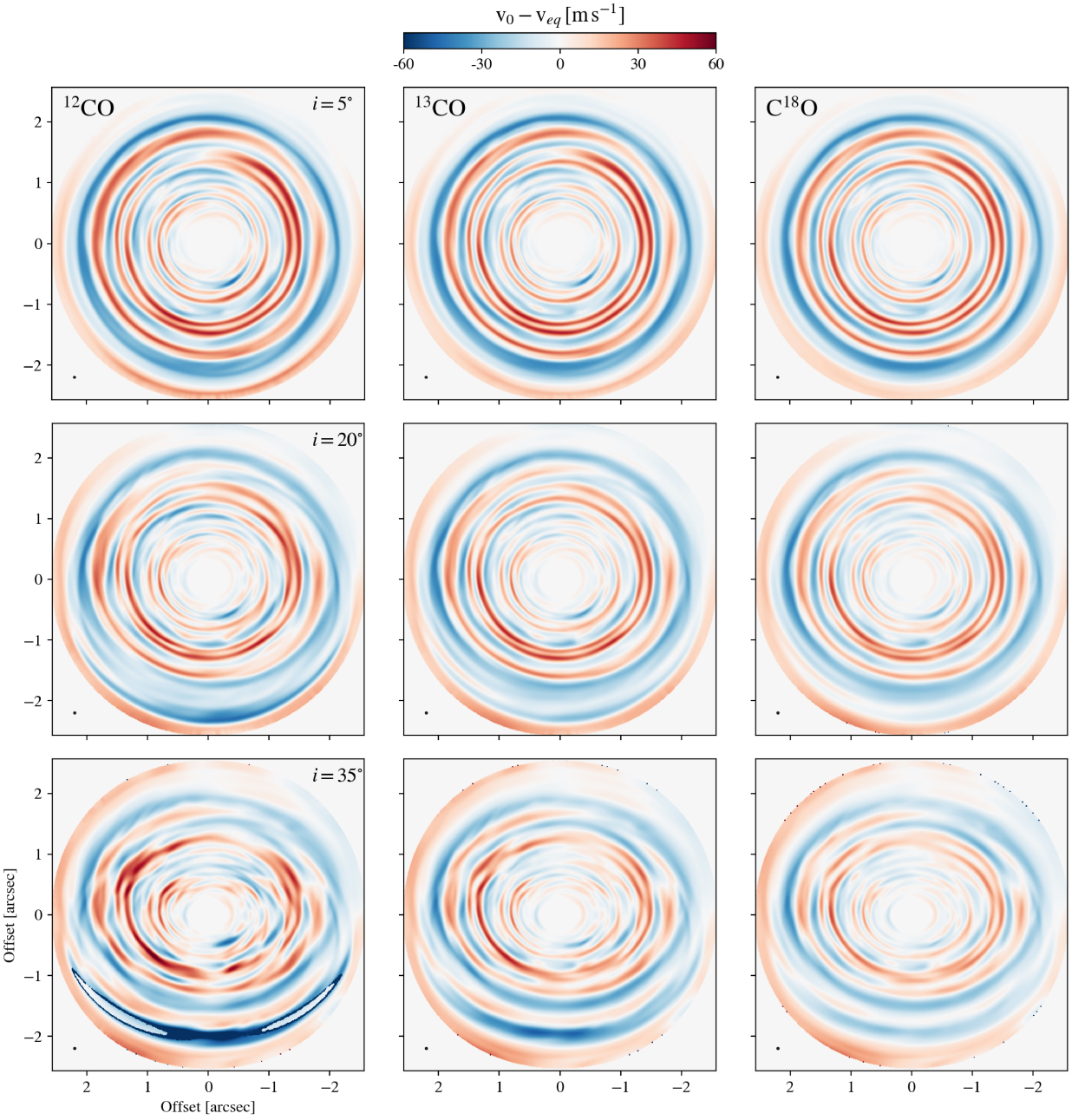

Figure 4.8: Results of the expected observable velocity perturbations from a VSI unstable disk synthetic lines observations for different CO isotopologues. From left to right, the columns show predictions for ^{12}CO, ^{13}CO and C^{18}O. From top to bottom, the rows show the results for disk inclinations of 5°, 20° and 35°. The mock data cubes have a velocity resolution of 0.05 km s^{-1}, and the images are convolved by a circular Gaussian beam of 50 mas, shown at the bottom left corner of each panel. The x- and y- axes indicate the R.A. and Dec. angular offset from the position of the central star, in arcseconds.

4.3.4 Detectability of VSI driven turbulence

A previous study has shown that a disk with isotropic turbulence can produce observable signatures of nonthermal gas motions in ALMA observations (Simon et al., 2015). First, it can produce a change in the shape of the spatially integrated line of emission, increasing the ratio of the peak line flux to the flux at line center. Such diagnosis has been applied to constrain disk turbulence in the outer regions of protoplanetary disks (see e.g., Flaherty et al. (2020) and references therein). We note that Simon et al. (2015) used a parametric fit to nonthermal gas motions to determine a turbulent broadening parameter as a function of radius and height. This parameter was then used as input in the line radiation transfer code LIME for the sake of computational efficiency. For our work we include the full 3D velocity field to calculate the line emission.

We explored if we can see the effect of line broadening by turbulence in our simulation data with anisotropic turbulence from the VSI. We compare directly the shape of the line of the synthetic observations for the VSI unstable disk, and a disk that follows a sub-Keplerian equilibrium solution with $v_{turb} = 0$, that is a laminar disk with the radial and meridional velocities being zero. We assume the same dust temperature structure for both disks. The comparison is shown in Fig. 4.9 for data cubes with spatial resolution of 50 mas (5 au) and velocity resolution of 50 m s^{-1}. We observe that the effect of VSI turbulence in the line shape is negligible compared to the thermal broadening for all inclinations and CO isotopologues explored. We recovered similar results for a disk around a central star with lower temperature, analogous to a young Sun, with an effective temperature of 4300 K and radius of $2.6\,R_{\odot}$. This highlights how important is to use the full 3D velocity data to produce synthetic observation and study the line broadening in protoplanetary disks.

The second main result by Simon et al. (2015) showed that isotropic turbulence can affect the distribution of the emission in a given velocity channel. Flaherty et al. (2020) has shown that anisotropic turbulent motions can mimic such effect in spatially or spectrally unresolved observations. We observe that this effect is minor in our predictions, as the physical size and magnitude of the velocity perturbations is rather small (about 10 au and 50 m s^{-1}). The finger-like features are already indistinguishable in independent channels for a spatial resolution of about 30 au. We summarize again that

a full 3D velocity field is needed when studying line-broadening. For ^{12}CO, the thickness of the emission layer is smaller than a scale height. Furthermore, line broadening is only caused by velocity fluctuations with physical scales smaller than the depth of the emission layer. This fact causes the turbulent broadening to be negligible because the amplitudes of these velocity fluctuations are about one order of magnitude smaller than the large scale fluctuations. We stress that it might be more promising to determine the kinematics by spatially and spectrally resolved observations in contrast to determine the line broadening in unresolved disk observations. Our results of the α viscosity values from the hydrodynamical simulations are consistent with the upper limits from nonthermal broadening in ALMA observations, with α viscosity values $\lesssim 10^{-3}$. We compute in our simulation a disk-averaged radial α value of $\alpha_{r\phi} = 1.4 \times 10^{-4}$, and a value about 3.6 times larger in the vertical direction (computed for one hemisphere of the disk following Eq. 4 in Stoll, Moritz H. R. et al., 2017), i.e. $\alpha_{z\phi} \sim 3.6\alpha_{r\phi}$. However, we note again that these are not directly comparable as stated above, and going for higher resolution, or more sensitive observations would not result on the constraint of a turbulent α from VSI. We emphasize that spatially resolving the velocity perturbations from the VSI is required to confirm it as a source of turbulence. Moreover, it is feasible to estimate an α viscosity value of the disk by directly comparing the observed velocity structure with synthetic predictions from 3D hydrodynamical simulations. We conclude that the currently applied diagnostics to detect nonthermal turbulent motions in ALMA observations using a parametrization of the turbulence level are not reliable if the turbulence is anisotropic. Therefore, we can not discard that the VSI is active in these disks, and that turbulence is still playing an important role. Finally, despite our simulations do not resolve the smallest scales of the instability (Flores-Rivera et al., 2020), we do not expect a change in the turbulent line broadening when resolving these. The smaller turbulence scales are expected to have lower RMS velocities due to the turbulent cascade. Therefore, they do not significantly contribute to the broadening of the integrated line emission.

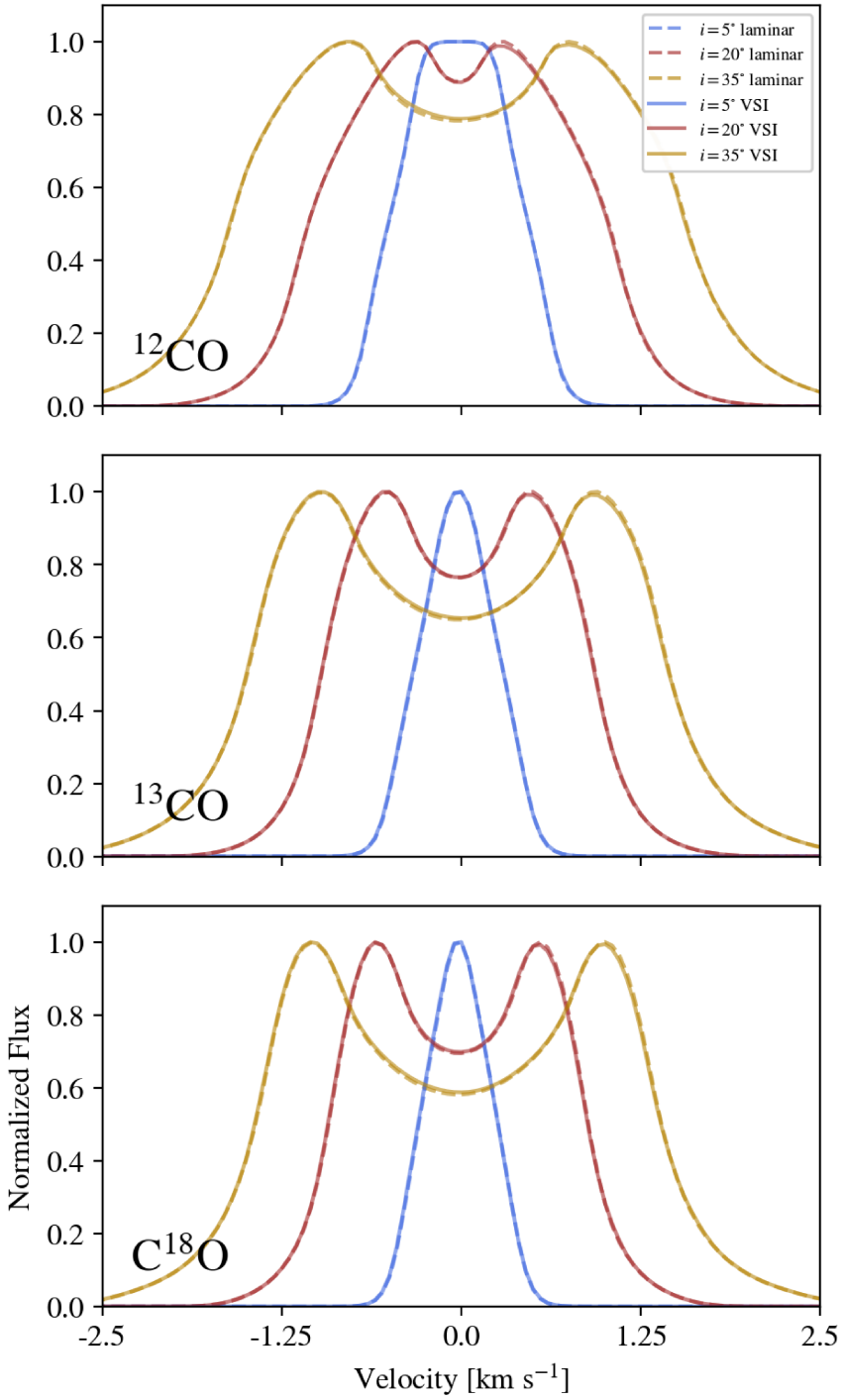

Figure 4.9: Line profiles from synthetic observations for different CO isotopologues and disk inclinations. In each panel we show a comparison of the integrated line emission for a VSI unstable disk (solid lines) and a laminar disk (dashed lines).

4.4 Discussion

4.4.1 Differences between VSI signatures and other mechanisms

Recognizing VSI-driven gas motions is very important to interpret kinematics observations. Large-scale perturbations in the gas velocities can also be produced by other mechanisms. For example, massive planets (Disk Dynamics Collaboration et al., 2020), vortices (Huang et al., 2018; Robert et al., 2020) or gravitational instabilities (Hall et al., 2020). Therefore, it is crucial to identify the features that can be used to separate the VSI signatures from other mechanisms.

Firstly, VSI signatures are quasi axisymmetric. Velocity perturbations of similar magnitude are visible in all velocity channels (see Figure 4.4), and show ringed substructures when extracted from the Moment one map (see Figure 4.5). On the contrary, perturbations from the aforementioned alternative mechanisms are asymmetric, as trace spiral-arms or localized deviations. Planetary-wakes and vortices are expected to be strongest in a few velocity channels and show a localized signature in the velocity centroid maps (Perez et al., 2015; Pérez et al., 2018; Huang et al., 2018; Robert et al., 2020). Large-scale spiral arms, however, can also appear across all velocity channels, yet are distinguishable from rings when extracted from the velocity centroid maps (Pérez et al., 2018; Hall et al., 2020).

Secondly, the velocity component that contributes more to the line of sight velocity of the perturbations in a VSI-unstable disk is the vertical component. For planetary wakes and spiral-arm structures the largest contributions are from the radial and azimuthal velocities (Pérez et al., 2018; Hall et al., 2020). Meridional flows can also be generated in the gaps carved by embedded massive planets (Kley et al., 2001; Morbidelli et al., 2014; Fung & Chiang, 2016; Teague et al., 2019a). For Jupiter mass planets, the azimuthally averaged velocities at the gap and gap's edges can have similar magnitude as the predicted VSI signatures (Teague et al., 2019a). However, such flows are typically present together with spiral arms and perturbations localized around the planet's location (Pérez et al., 2018; Juhász & Rosotti, 2018). Therefore, resolved two-dimensional velocity centroid maps are required to disentangle between both scenarios.

Thirdly, the vertical motions of the VSI-modes are present in the whole disk vertical extent. Therefore, no significant change in the morphology of the

observable VSI signatures are predicted when tracing different CO isotopologues. For planetary wakes and spiral arms, it is expected that the observable velocity perturbations change depending on disk height (Perez et al., 2015). Fourthly, an embedded planet in a slow-cooling disk can generate additional tightly wound spiral arms due to buoyancy resonances. These spirals can have a strong vertical velocity component and produce observational signatures that can be confused with VSI signatures (Bae et al., 2021). Nevertheless, high spatial resolution observations can potentially disentangle between tightly wound spirals and VSI quasi axisymmetric rings in the line of sight velocity residuals.
Finally, VSI-perturbations are expected to produce dust traffic jams in the outer disk (Flock et al., 2017, 2020; Schäfer, Urs et al., 2020). It can also generate a dust trap at the radial transition where the cooling-timescale is short enough to sustain the VSI (Flock et al., 2020). Additionally, it can trigger Rossby Wave Instability vortices (Flock et al., 2020; Manger & Klahr, 2018), which can efficiently trap dust at its center (Barge & Sommeria, 1995). Similar structures in the dust distribution can be produced by embedded planets. Thus, it is difficult to disentangle between VSI and other mechanisms when studying the radial and azimuthal distribution of the dust continuum. Nevertheless, by studying the vertical distribution of the dust from edge on it is possible to assess if dust vertical mixing from the VSI is present (Flock et al., 2017, 2020; Villenave et al., 2020).

In our simulation, short-lived small-scale Rossby Wave Instability vortices appear, consistent with previous results on VSI-unstable disks with very short thermal relaxation time scales (Richard et al., 2016; Flock et al., 2020). These vortices could produce kinematic signatures in CO line emission, as previously shown for large-scale planet-induced vortices (Huang et al., 2018; Robert et al., 2020). However, we focus on the global quasi-axisymmetric ringed structure produced by the VSI. Further analysis is needed to constrain the observability of vortices induced by the VSI in CO kinematics.

4.4.2 Constraints on the disk properties from a VSI-detection

Strong constraints can be done from the detection of the VSI in a protoplanetary disk. First, a VSI detection would confirm that the disk has a vertical shear and a radial gradient of the temperature. Second, a short cooling timescale is necessary for the VSI to operate in the traced layers of the

disk. Via hydrodynamical simulations it has been shown that the VSI is active in disks with cooling timescales $< 10\%$ of the local orbital timescale (Nelson et al., 2013; Lin & Youdin, 2015; Flock et al., 2020). Hence, a VSI detection would constrain the disk cooling timescales. Finally, it also shows that the turbulence in the disk is fully or partly due to the VSI, which has been constrained from hydrodynamical simulations to α viscosity values in the range of 10^{-5} to 10^{-3}. Damping of the VSI is predicted for the upper layers of the disk where the densities are low enough to allow collisional dust-gas decoupling (Pfeil & Klahr, 2021) and magnetic effects dominate (Cui & Bai, 2020). Therefore, studying the velocity perturbations at different layers of the disk can help us to understand changes in physical conditions at different disk heights.

4.4.3 Observations spatial and spectral resolution

We explored the effect of spatial and spectral resolution on the observable velocity perturbations for a disk with an inclination of 20 degrees. We display in Figure 4.10 the expected velocity perturbations from a VSI unstable disk varying the velocity resolution of the data cube, and size of the convolved circular Gaussian beam, in the first and third row, respectively. Additionally, the statistical uncertainties from the calculation of the line centroid maps derived using Eddy (Teague & Foreman-Mackey, 2018) are shown in the third and fourth rows. Each data cube has added white noise with an RMS level expected from a 20 h integration ALMA observation. We observe that for beam sizes ≤ 10 au the VSI structure is well resolved. For such a high spatial resolution, all velocity resolutions explored reach an uncertainty level smaller than $\sim 20\%$ the channel width and the structure is recovered. However, only for the highest velocity resolution cases (channel width ≤ 50 m s^{-1}) these uncertainties are below $\sim 20\%$ the magnitude of the velocity perturbations. In summary, we found that high resolution observations using ALMA extended antenna configurations can spatially resolve the VSI signatures. However, the highest spectral resolution observations are needed for a robust detection.

For our predictions, with an assumed distance to the system of 100 pc, a 0.1 arcsecond resolution is enough. In ALMA band 6, the antenna configuration 8 gives the required resolution, where a 20h integration time can get sufficient signal-to-noise ratio. Disks further away would require higher angular resolution to resolve the VSI, which would require a longer integration time.

Our simulated observation setup is at the limit of the capabilities available for ALMA Cycle 8. Therefore, detection of VSI-signatures in the next ALMA cycle might be feasible for the brightest protoplanetary disks only.
Considering a standard Hanning smoothing, the highest resolutions are ~ 0.05 km s^{-1} and~ 0.03 km s^{-1}, for ALMA Bands 6 and 7, respectively. According to our predictions, with these resolutions it is possible to resolve well the VSI signatures. Nonetheless, no spectral averaging and avoiding Hanning smoothing when preparing ALMA observations allows to achieve finer spectral resolution (down to ~ 0.025 km s^{-1} for Band 7), which could ease the identification of VSI signatures.
We highlight that a good calibration is key to recover velocity perturbations from the data. For such a high spectral resolution observation to be successful, at least one of the basebands should be set up in TDM/wideband to get the best calibration. Otherwise, there may not be enough total bandwidth for best phase calibration, and this is truly essential to get the highest dynamic range images using self-calibration.
Our predictions are also valid for the CO J:3-2 transitions, observable within ALMA Band 7 in which higher velocity resolution observations are possible. Moreover, observing ^{12}CO and ^{13}CO within the same observation can be done for the J:3-2 transition. Obtaining the VSI signatures at different layers of the disk is important to better understand the vertical flows in the disk, and can potentially confirm the origin of the velocity perturbations.
The velocity resolution required to identify the VSI signatures could also vary depending on the method used to compute the line centroids and extract the velocity perturbations. Alternative methods to obtain the moment maps and the non-perturbed velocity centroid map are GMoments[13], and ConeRot[14] (Casassus & Pérez 2019, Casassus et al. in prep). The advantage of ConeRot compared to Eddy is that the perturbations can be extracted directly from observations without strong assumptions about the underlying disk model, and employing a reduced number of free parameters. Nevertheless, we do not expect significant differences in our results, but in its application to ALMA data.
Last, further study of the disk velocity structure can be performed analysing the velocity radial profiles. For this purpose ConeRot and

[13] https://github.com/simoncasassus/GMoments
[14] https://github.com/simoncasassus/ConeRot

GOFISH[15](Teague, 2019b) can be applied. However, as discussed in Section 4.4.1, a thorough study of the three velocity components at different layers of the disk would be required to possibly disentangle between perturbations produced by planets or VSI.

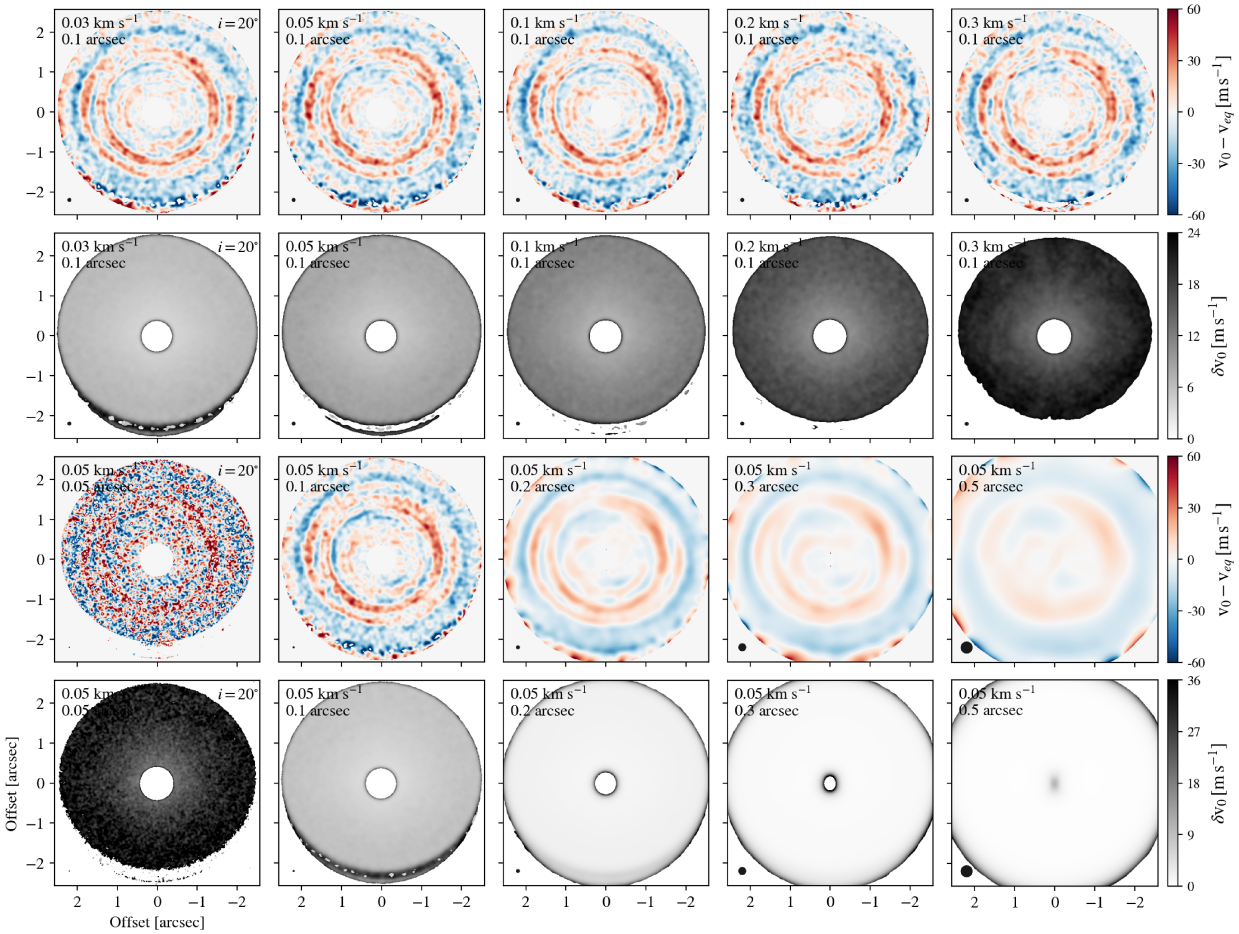

Figure 4.10: Results of the expected observable velocity perturbations from a VSI unstable disk ^{12}CO synthetic lines observations ($v_0 - v_{eq}$), for various velocity and spatial resolution data cubes. Each channel of the cube has a RMS noise expected from a 20 h integration ALMA observation with an extended configuration (1.9, 1.5, 1.0, 0.8, 0.6 mJy from the higher to the lower velocity resolution cases). In addition, we show the uncertainties in the calculation of the velocity centroid map using BETTERMOMENTS (δv_0). The FWHM of the circular Gaussian beams are shown at the bottom left corner of each panel. The x- and y- axes indicate the R.A. and Dec. angular offset from the position of the central star, in arcseconds.

[15] https://github.com/richteague/gofish

4.5 Summary

In this chapter, I presented a study of the observability of gas motions produced by the vertical shear instability (VSI) in ALMA CO kinematics observations. We explore the effect of disk inclination, spatial and spectral resolution. Furthermore, we compare the results for different CO isotopologues. We couple the results of 3D global hydrodynamical simulations of a disk unstable to the VSI, with radiative transfer calculations to obtain synthetic line emission predictions for ^{12}CO, ^{13}CO and C^{18}O molecules. Next, we produce simulated observations that are directly comparable to those obtained by ALMA. Finally, we extract the velocity perturbations from our simulated observations, and recover the VSI perturbations. The main findings from this project are:

- We find that the VSI perturbations are seen as a corrugated pattern in the emission of individual velocity channels, and quasi axisymmetric concentric rings in the line of sight velocity residuals after subtracting a sub-Keplerian disk model fitted to the data.
- The characteristic morphology of the extracted perturbations results from the meridional velocity component being dominant in the velocity projected into the line of sight.
- With increasing inclination, the line of sight velocity has stronger addition of the radial and azimuthal velocity of the disk, adding asymmetries on top of the rings, making the VSI-perturbations challenging to characterize. Moreover, the method to extract the perturbations does not correctly recover the expected morphology for large inclinations ($i \gtrsim 35°$).
- The morphology of the extracted VSI velocity perturbations is predicted to be similar for different layers of the disk. The change in the magnitude of the expected velocity perturbations for different tracers remains relatively low for all inclinations explored. Further, the difference in magnitude increases with disk inclination.
- Our results show that the nonthermal broadening produced by the VSI in integrated line emission is negligible, consistent with current limits from ALMA radio observations. We emphasize that resolving the structure is fundamental to determine the turbulence sources in the disk.

- To recover the VSI-perturbations, spatial resolution below the disk pressure scale height might be enough to resolve the structures, which in our case corresponds to beam sizes $\lesssim 10$ au. However, the spectral resolution needed to capture the perturbations reliably ($\lesssim 0.05\,\mathrm{km\,s^{-1}}$) is the highest available with the ALMA interferometer.

I highlight that the predictions are optimistic and the predicted observational signatures should be treated as upper limits. The conducted simulations are inviscid and follow a locally isothermal equation of state, giving the ideal conditions for the development of vigorous VSI motions in the disk. The inclusion of a finite cooling time or background viscosity can weaken the VSI perturbations.
Observing the gas kinematics at different layers of the disk is important to disentangle between the VSI and other mechanisms that could produce similar kinematic signatures. We conclude that the best cases to detect VSI signatures are gap-less disks close to face-on, in which the VSI meridional flows can be directly traced.
Finally, the presence of velocity perturbations from a different origin (e.g., massive planets) can obstruct the identification of the VSI signatures. In Chapter 5, I present an investigation of kinematic signatures in the case of a disk unstable to the VSI interacting with massive embedded planets. However, further work is needed to study other possible physical mechanisms that could coexist with the VSI affecting the observed kinematical structure.

5 Kinematical signatures of planet-disk interactions in VSI-turbulent protoplanetary disks

This chapter presents results of the research publication in preparation *"Kinematical signatures of planet-disk interactions in VSI-turbulent protoplanetary disks"* (Barraza-Alfaro et al. in prep.).

5.1 Introduction

Planets are thought to form inside the weakly ionised region of protoplanetary disks. In the fast cooling parts of the dead-zone the vertical shear instability (VSI) can be active, inducing turbulence and large-scale gas motions. The objective of this project is to understand what is the effect of the turbulence and gas motions generated by the VSI, in the evolution of the structures triggered by a fairly massive planets, and vice versa.

While our results of the observability of the VSI presented in Chapter 5 predicts clear kinematical signatures of the VSI, these simulations assume a clean case, in which the VSI develops without interacting with planets or other physical processes. However, the brightest disks, in which the VSI could be observed, also show dust substructures that hint the presence of unseen embedded massive protoplanets. Therefore, it is important to understand how these unseen planets would affect the detectability of VSI kinematic signatures, and explore how the VSI could affect the kinematical detection of these planets.

Planets embedded in VSI-unstable disk have been previously studied for planets of 10, 30 and 100 earth masses (Stoll et al., 2017). While for the 10, and 30 M_{earth} cases the VSI remains unaffected by the presence of the planets, a 100 M_{earth} planet can change the VSI dynamical structure at the midplane. Following these results, we studied further these interactions by conducting global 3D hydrodynamical simulations of an inviscid and locally isothermal

VSI-unstable disk with an embedded massive planet. We explore the cases of an embedded Saturn mass planet ($\approx 95\ M_{earth}$) and Jupiter mass planet ($\approx 318\ M_{earth}$). Moreover, we compare the VSI-unstable disks with results from an alpha-viscous disk. Post-processing our set of simulations with a radiative transfer code, we studied the kinematical signatures that could be observed in CO high resolution ALMA radio interferometric observations.

The present Chapter is structured as following. First, I present the global 3D hydrodynamical simulation results. Second, I show the results of the Radiative Transfer calculations and synthetic observations. Third, I present the discussion of results and Fourth, I draw the chapter's main conclusions.

5.2 Hydrodynamical Simulations Results

As initial conditions for the simulations we use the same equilibrium solutions as presented in Chapter 4 Section 4.2.1. The simulations grid have the same domain and resolution in the radial and azimuthal direction as our simulation presented in Chapter 4. However, is extended in the colatitude direction to cover $10H$ at the code unit of length, with a resolution of 196 cells.

5.2.1 Inclusion of planets

For the inclusion of planets, we use an standard approach slowly inserting the planet as a gravitational potential of a point of mass, with a smoothing around the location of the planet (e.g., Stoll et al. 2017).

$$\Phi_P = \begin{cases} -\frac{GM_P}{d}, & \text{for } d \geq d_{rsm}, \\ -\frac{GM_P}{d}\left[\left(\frac{d}{d_{rsm}}\right)^4 - 2\left(\frac{d}{d_{rsm}}\right)^3 + 2\left(\frac{d}{d_{rsm}}\right)\right], & \text{for } d < d_{rsm}, \end{cases} \tag{5.1}$$

where d is the distance between a fluid element and the planet's position. A potential smoothing length d_{rsm} is used to prevent numerical artifacts at the planet location. The value of d_{rsm} is set to be three cell diagonals evaluated at the planet location, this corresponds to around 56% of Saturn's and 37% of Jupiter's Hill spheres ($r_{Hill} = r_p(m_p/3M_\star)^{1/3}$).
In order to avoid numerical artifacts during the inclusion of the planet, its mass is smoothly increased from zero to its final mass in 40 and 100 planetary orbits for the Saturn and Jupiter cases, respectively. We include the planets

in the VSI-unstable disk simulations after 200 orbits of evolution, when the VSI is already in its saturated state (as shown in Figure 4.1 and discussed in Section 4.2.2).

To compare directly our simulations of VSI-unstable disks with a case without VSI, we run the same set of simulations including artificial viscosity following the alpha prescription of Shakura & Sunyaev 1973, that is $\nu = \alpha c_s H$, for a viscosity value comparable to the effective viscosity driven by the VSI. Including artificial viscosity with $\alpha = 5 \times 10^{-4}$ is enough to damp the VSI in the disk and recover similar structures from previous studies of planet-disk interactions in isothermal disks (e.g., Pérez et al. 2018; Rabago & Zhu 2021).

We inspect and post-process the output after 300 orbits of evolution for the VSI simulation without a planet, while for the Jupiter and Saturn mass planets simulations we chose the outputs after 145 and 285 orbits after the inclusion of the planet, respectively. At these times, the planets have already carved a gap and the structures are in quasi steady state.

5.2.2 VSI-unstable planet-forming disks

In this sub-section we describe the structures induced in our set of VSI-unstable disk simulations. First, we compare a cartesian face-on view of the simulations fields at the midplane (Figure 5.1) and above three pressure scale heights of the disk (Figure 5.2). Particularly important is to inspect different disk heights, since observations of optically thick CO isotopologues, such as ^{12}CO, trace upper layers of the disk, while optically thinner can trace deeper layers (e.g., C^{18}O).

In both Figures 5.1 and 5.2, we present a simulation without an embedded planet (first row), with an embedded Saturn (second row), and with an embedded Jupiter (third row). The columns indicate, gas density relative to the initial density field (ρ/ρ_0; first column), radial velocity (v_r; second column), meridional velocity (v_θ; third column), and azimuthal velocity deviations from Keplerian rotation ($v_\phi - v_{Kep}$; fourth column). For reference, in the radial velocity negative values indicate gas moving towards the central star, in the meridional direction positive values indicate gas flowing downwards (e.g., positive flow at $Z \sim 3H$ means gas moving towards the midplane), while in the azimuthal direction positive means super-Keplerian flow. In the first rows

of Figures 5.1 and 5.2, we recover the velocity structure of a disk unstable to the VSI as described in Chapter 4 Section 4.2.2. In the midplane, the axisymmetric meridional flows dominate the velocity structure, while in the surface strong velocity perturbations are seen in all velocity components. In the simulations including planets (second and third rows), a gap depleted of gas carved by the planet, deeper and eccentric for the Jupiter-mass planet case. At the edges and inside the gap, rings of super- and Sub-Keplerian gas are seen. Additionally, spiral arms via Lindblad resonances are induced by the planets in the density, and radial and azimuthal velocities. Around the planet location, planetary spiral wakes are also produced by the planets. Moreover, a large-scale vortex is also produced by the Jupiter planet, seen as a horseshoe shaped structure in the gas density (see also Chapter 2 Section 2.4 on planet-disk interactions). At the disk midplane, we observe that the planet induced structures dominate the overall structure. Interestingly, in the meridional velocities, damping of the VSI flows is produced for both planet masses. Such dampling, is produced in the region inside the planet radial location, the gap and gap outer edge. At the disk surface, however, damping of the VSI meridional flows seems to be present only for the Jupiter mass case (see Figure 5.2). For the Saturn mass planet case, a mixture of VSI structures and the planet-induced spiral arms is observed. The velocity structure in the meridional and azimuthal directions from the VSI simulation without a planet and a Saturn mass planet are similar overall; however, a global damping of the VSI induced flows is produced by the planet, reaching lower velocities. Finally, in the Jupiter case, the localized velocity flows around the planet are strongest in the radial and meridional directions, while in the azimuthal directions a ring of super-Keplerian gas at the outer gap edge is the most prominent feature.

To highlight the stronger damping of the VSI at the disk midplane produced by the presence of the embedded planets, we show a $Z - R$ view of our set of VSI-unstable disk simulations in Figure 5.3. We present the azimuthally-averaged fields, following the same order of presentation as in Figures 5.1 and 5.2. Clearly, the damping of the VSI is more effective in the region below three pressure scale heights from the midplane. In the outermost regions of the disk, flows induced by the VSI are still active, characterized by the full columns of gas moving upwards or downwards. A interesting feature also seen in Figure 5.3, later discussed in Section 5.4, is the different symmetry of the flows with respect to the midplane from the perturbations induced by

planets and the VSI. In the radial and azimuthal directions, the VSI flows are symmetric with respect to the midplane, while planet-induced flows are anti-symmetric. On the contrary, in the meridional direction the VSI flows are anti-symmetric with respect to the midplane, while planet-induced flows are symmetric, that is they move towards the midplane at both disk hemispheres.

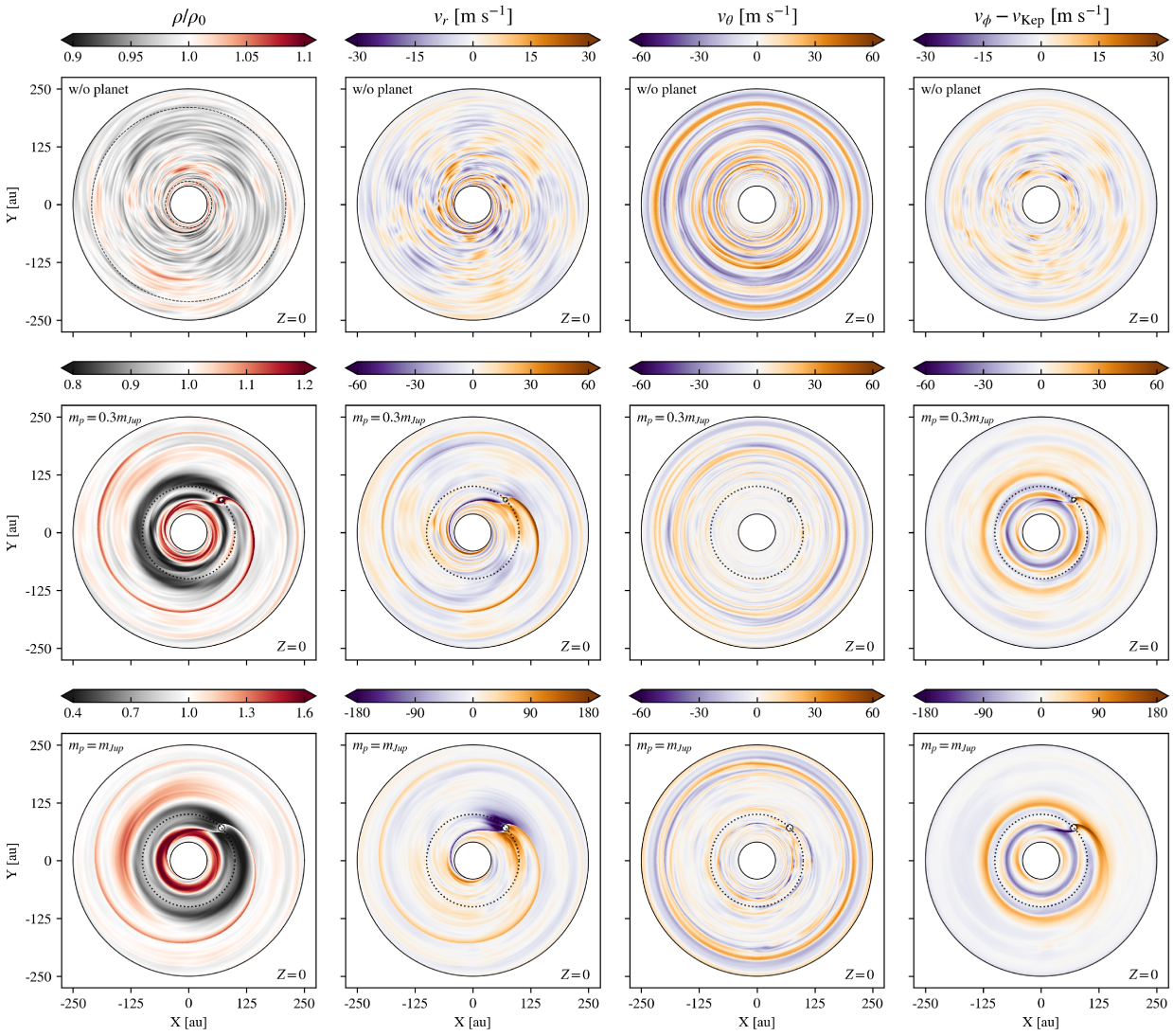

Figure 5.1: VSI-unstable disks simulations at the disk midplane ($Z = 0$). From left to right, gas density normalized by the initial value, radial velocity, meridional velocity, and azimuthal velocity deviations from Keplerian rotation. From top to bottom, simulation without an embedded planet, with a Saturn planet ($m_p = 0.3 m_{Jup}$), and a Jupiter planet ($m_p = m_{Jup}$). The black dashed lines in the first panel show the simulation buffer zones. The white circles show the location of the planets, in which their sizes are equal to the planets' Hill spheres.

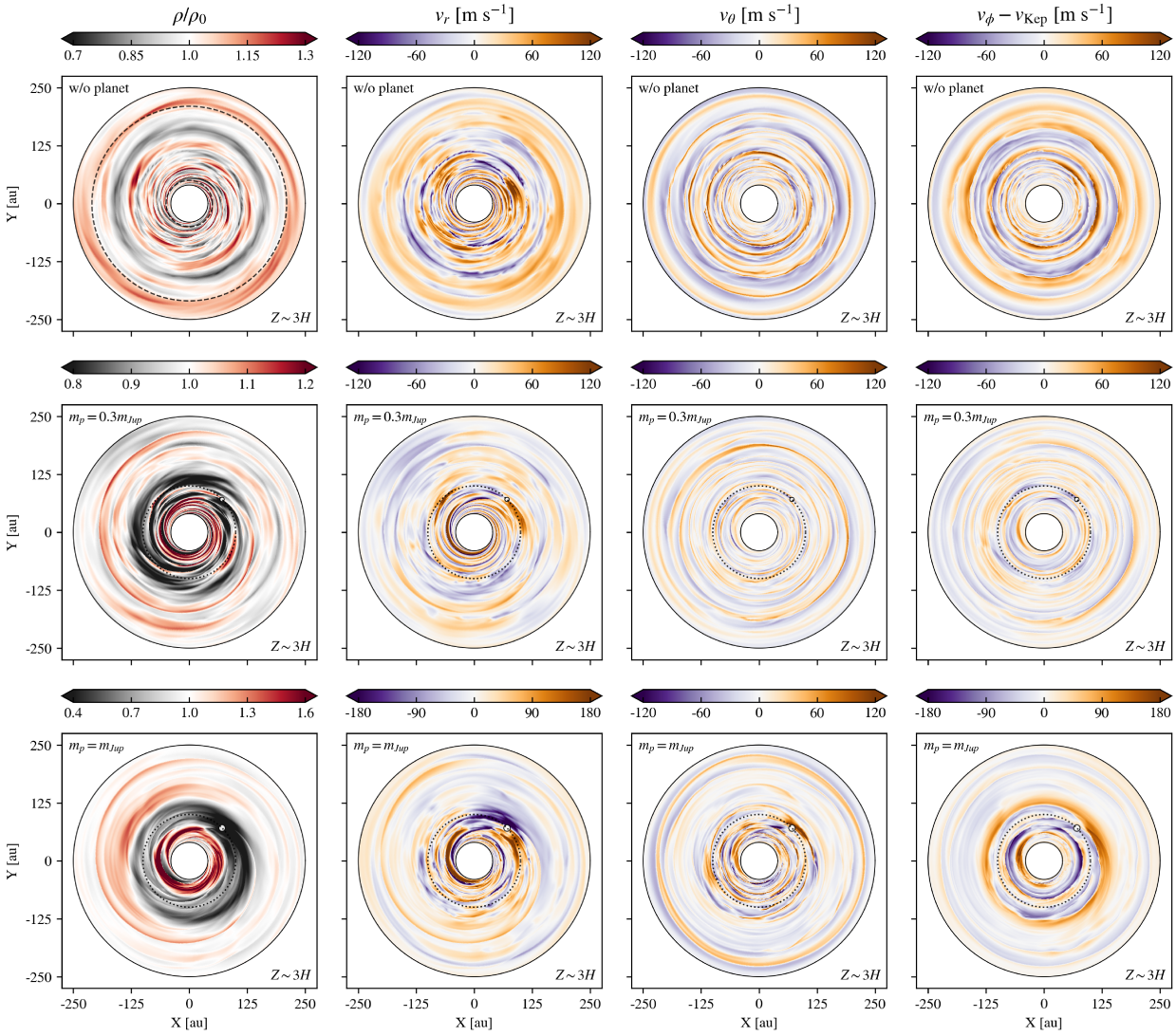

Figure 5.2: VSI-unstable disks simulations at the surface. Same as Fig. 5.1 but above three pressure scale heights from the midplane ($Z \sim 3H$).

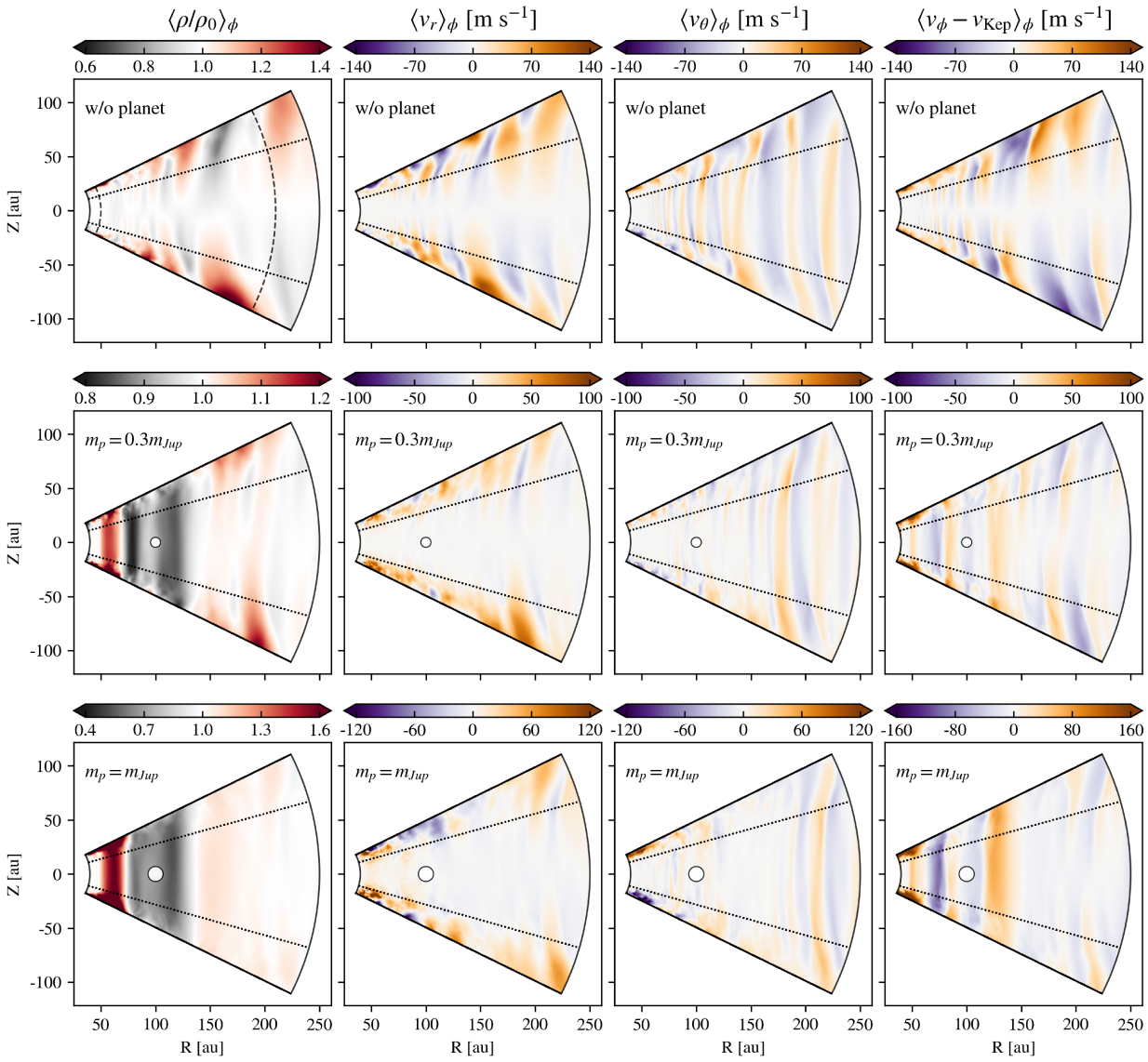

Figure 5.3: $R - Z$ view of the azimuthally-averaged fields of our VSI-unstable disks simulations. From left to right, gas density normalized by the initial value, radial velocity, meridional velocity, and azimuthal velocity deviations from Keplerian rotation. From top to bottom, simulation without an embedded planet, with a Saturn planet ($m_p = 0.3 m_{Jup}$), and a Jupiter planet ($m_p = m_{Jup}$). The black dashed lines in the first panel show the simulation buffer zones. The black dotted lines indicate the height $Z \sim 3H$. The white circles show the radial location of the planets, in which their sizes are equal to the planets' Hill spheres.

5.2.3 Time evolution of VSI modes

We studied the time evolution of the VSI induced large-scale meridional velocity flows in our VSI-unstable disk simulations, in order to explore the damping produced by the presence of massive planets. In Figure 5.4, we show the azimuthal average of the meridional velocity at the disk midplane ($Z = 0$) at each orbit, for 300 orbits starting at the time in which we include the planets in our planet-disk interactions simulations. The axis-symmetry of the VSI modes allows to observe the VSI unstable modes evolution clearly in the azimuthal averages.

In the first row of Figure 5.4, we show the time evolution of a simulation without embedded planets, in which the VSI operates in its saturated stated. Radial migration towards the central star of the VSI modes is observed, with narrow radial regions in which the VSI is weakest migrating outwards. These results are consistent with previous findings of the VSI modes time evolution (e.g., Pfeil & Klahr 2021). Note that the innermost region is damped by the effect of the buffer zones.

In the second and third rows of Figure 5.4, is shown the time evolution of the VSI unstable simulations with an embedded Saturn-mass planet (second row) and the simulation with an embedded Jupiter-mass planet (third row). The planets are located at 100 au from the star, indicated by the horizontal black dotted line. It's clear that the planets produce a damping of the flows induced by the VSI, particularly in the regions inside its radial orbit, along the gap region, and outer edge of the gap. The damping produced by the Saturn-mass planet weaker; therefore, the VSI motions still vigorous in most of the outer regions of the disk after 300 orbits ($r \gtrsim 150$ au). In the case of an embedded Jupiter, the damping of the VSI is very effective, in wich the VSI motions are damped up to ~ 200 au from the star.

While we did not find a direct correlation of the dampened regions with other quantities, the time-scale of the damping is similar to the times-scale of the gap opening by the planets. Therefore, we attribute the damping to the effects of the planets in the gas density and pressure structure, in combination with the influence of the planet-triggered spiral arms in the global disk evolution.

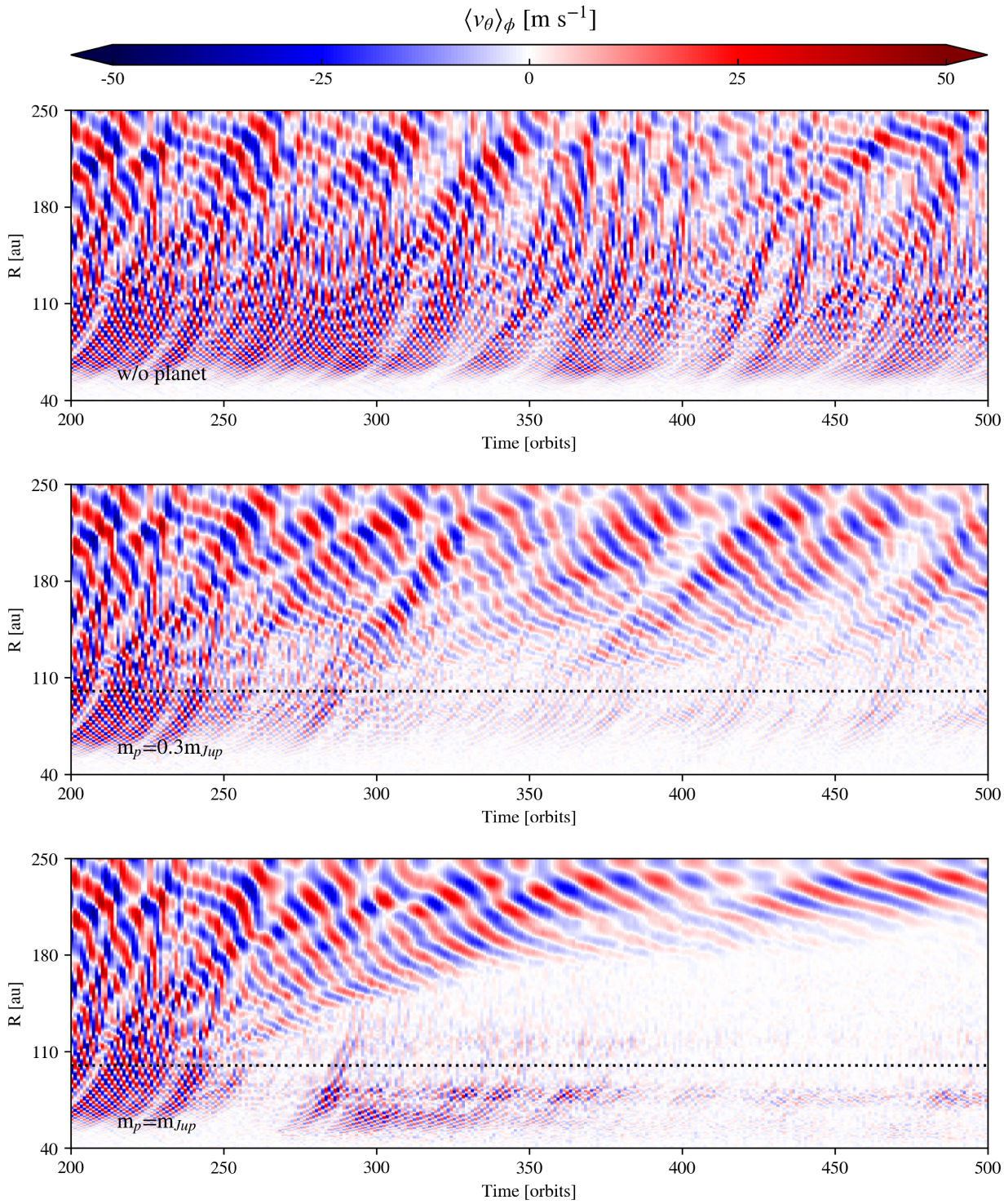

Figure 5.4: Time evolution of the azimuthally averaged meridional velocity at the disk midplane ($Z = 0$). From top to bottom, we show the simulation of VSI without an embedded planet, with an embedded Saturn mass planet, and with an embedded Jupiter mass planet. The orbits are measured at the the planets radial location (100 au), shown by black dotted lines. The figure starts at 200 orbits, time in which the planets are slowly inserted in the simulation.

5.2.4 Alpha-viscous vs VSI-unstable disks

In this sub-section we compare the disk structure produced by planets in turbulent VSI-unstable disks and alpha viscous disks, both at the disk midplane (Fig. 5.5) and surface ($Z \sim 3H$; Fig. 5.6). This is a simplified approach to compare disks with and without the VSI operating in the disk. We present the simulations gas density and velocities results in the same order of columns as Figures 5.1, 5.1 and 5.3.

It is clear that the VSI induces additional fine structure in all velocity fields, while the structures of the α-viscous simulations is smoothed by the artificial viscous diffusion. The artificial viscosity significantly reduces the velocity magnitude of the flows around the planets, relevant for constraining planet masses from CO kinematic observations.

Particularly different between VSI and α-viscous simulations is the meridional velocity structure, in which the meridional quasi-axisymmetric rings from the VSI are observed. Moreover, inside the carved gaps the VSI turbulence disrupts the meridional velocity structure at the surface layers, opposite to the smooth rings of meridional flows along the gap and gap edges observed in the viscous disks. Finally, we observe that in the VSI-unstable case the Jupiter planet triggers a stronger anti-cyclonic vortex at the outer edge of the gap.

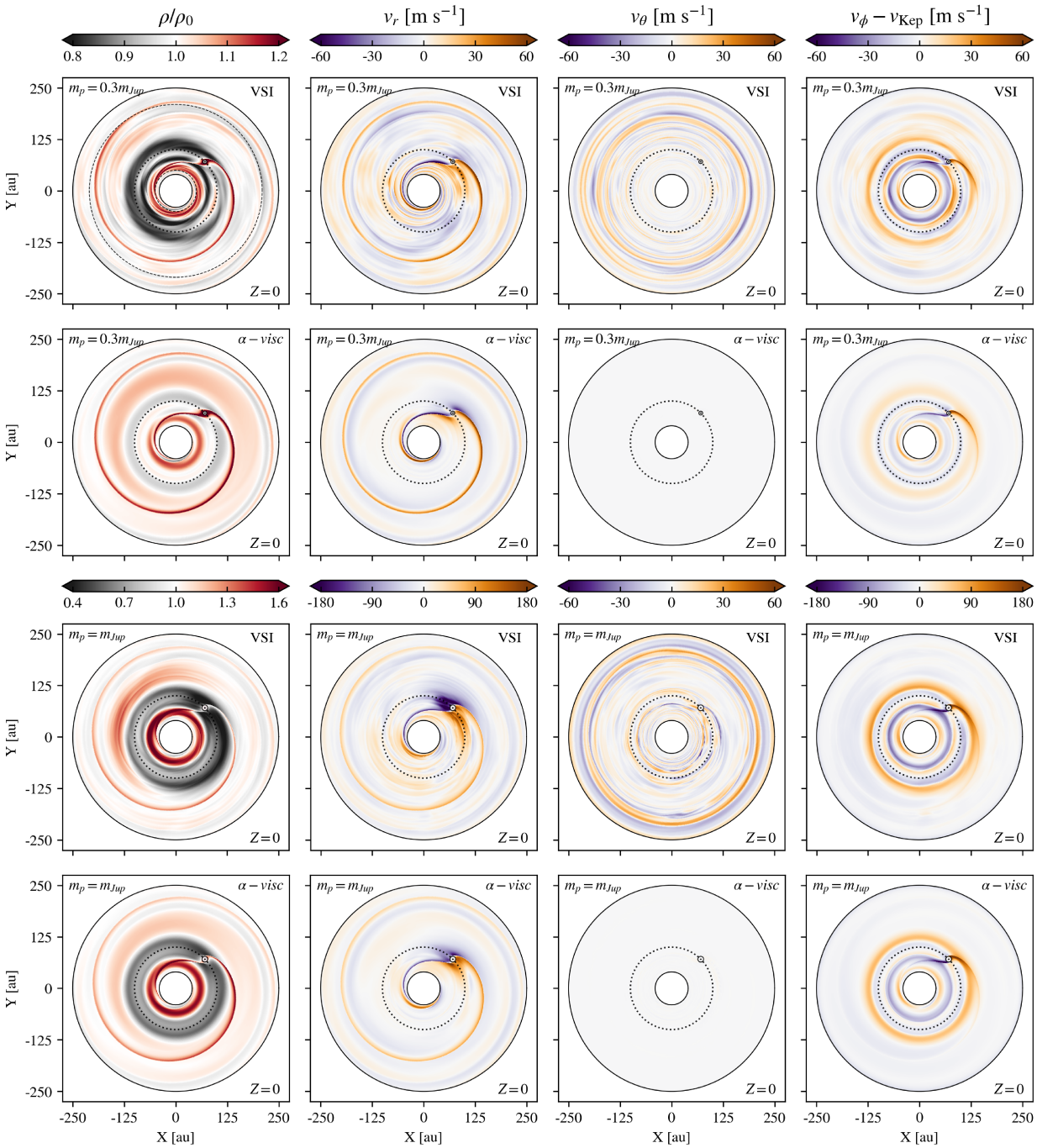

Figure 5.5: VSI-unstable and α-viscous disks ($\alpha = 5 \times 10^{-4}$.) simulations at the disk midplane ($Z = 0$). From left to right, gas density normalized by the initial value, radial velocity, meridional velocity, and azimuthal velocity deviations from Keplerian rotation. From top to bottom, VSI simulation with a Saturn planet ($m_p = 0.3 m_{Jup}$), α-viscous simulation with a Saturn planet, VSI simulation with a Jupiter planet ($m_p = m_{Jup}$), and α-viscous simulation with a Jupiter planet. The black dashed lines in the first panel show the simulation buffer zones. The white circles show the location of the planets, in which their sizes are equal to the planets' Hill spheres.

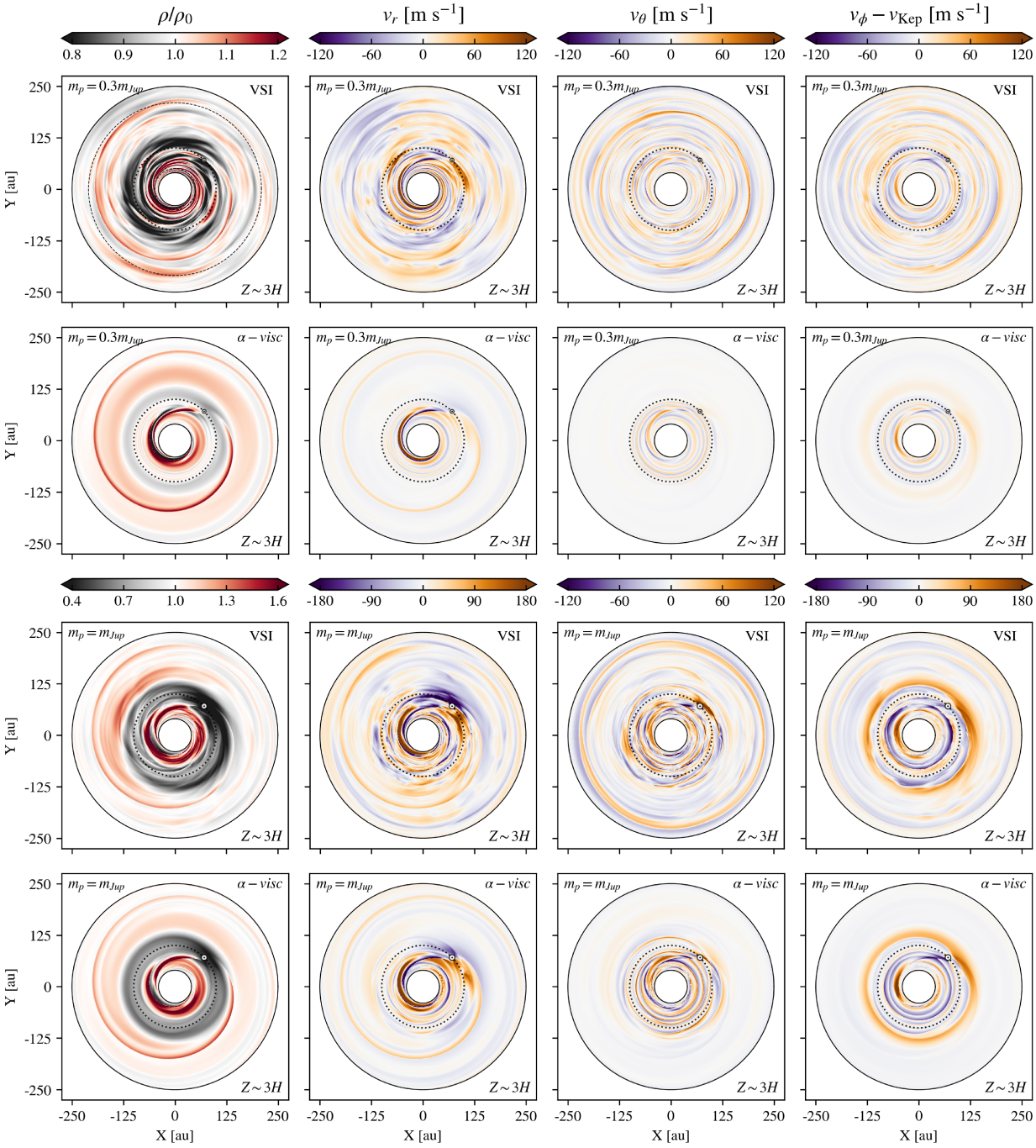

Figure 5.6: VSI-unstable and α-viscous disks ($\alpha = 5 \times 10^{-4}$.) simulations at the disk surface. Same as Fig. 5.5 but above three pressure scale heights from the disk midplane ($Z \sim 3H$)

5.3 Radiative Transfer Results

For the physical model used in the radiative transfer models presented in this Chapter, we follow the same approach and model than the presented in Chapter 4. Nevertheless, in this chapter we used only one dust size bin for the temperature calculation, representing a range of sizes between 0.05 μm and 10μm. We found no significant difference in the temperature structure obtained, and since the dust is not included in the line radiative transfer there is no effect in the image ray-tracing. Additionally, we now include a simplified freeze-out of the CO into grains, by reducing the number density of the CO isotopologues by 10^{-5} in the regions where the temperature falls below 21 K.

For the orientation in the sky of the disk in our synthetic line radiative transfer predictions we chose a disk position angle of 140° (east-of-north), while the inclinations are set so the near side is the north-east. For the predictions including a planet, the position of the planet is located roughly 30° clock-wise starting from the semi-minor axis in the north-east part of the disk. We fixed the planet location to the reduce the amount of free parameters; however, the kinematic signatures from a planet would vary depending on its position (e.g., Pinte et al. 2020). We explore the kinematic structure of the disk models for inclinations of 5, 15 and 30 degrees.

We compute synthetic images of the J=3-2 rotational transition for ^{12}CO, ^{13}CO and C^{18}O, centered at $\approx$ 345.795 GHz, $\approx$ 330.587 GHz and $\approx$ 329.330 GHz, respectively. We create a set of synthetic datacubes with a resolution of 10 m s^{-1} covering 7.5 km s^{-1}, without artificial micro-turbulence. Nevertheless, the cubes used for the simulated ALMA observations are averaged to a 100 m s^{-1} velocity resolution, to mimic observational limitations.

Next, we computed simulated ALMA observations with CASA simobserve (McMullin et al., 2007) for our ^{12}CO images. We simulate the uv-coverage of a total of 10h on-source observation. The angular resolution of our mock observations is $\approx$ 0.07 arcseconds ($\approx$ 7 au). Aiming to study the structures observed in high signal-to-noise observations, we include a noise level of 1 mJy per beam per channel in the simulated observations of ^{12}CO. These simulated observations fulfill the spatial and velocity resolution needed for robust kinematical detection of massive planets (Disk Dynamics Collaboration et al., 2020). We do not explore the observability with ALMA of the kinematical structure in ^{13}CO and C^{18}O due their fainter emission.

5.3.1 Kinematical signatures: An idealistic view

First, we compare the kinematical signatures of our disk models in an idealistic case, that is without beam convolution nor inclusion of noise, and for a velocity resolution of 5 m s^{-1}. We first study this case in order to have a reference of what would be extracted from our disk model synthetic predictions in an ideal case of unrealistically deep observations and perfect modelling. For this purpose, we extract the deviations from Keplerian rotation in the line-of-sight velocity maps computed from our RAW synthetic radiative transfer images. Further, in order to extract the deviations from Keplerian rotation from the line of sight velocity map of the perturbed disks, we subtract a second line of sight velocity map computed for a disk following our disk equilibrium solutions. To avoid effects from variations in the traced CO emission layer in the residuals, we only change the model velocities to the equilibrium solutions keeping the same CO number densities and disk temperature. Therefore, this approach is not feasible to apply in real observations; however, as aforementioned, is to have an ideal view of what could be the non-Keplerian signatures in an ideal picture. We present these predictions for our set of simulations in Figure 5.7, for three different disk inclinations (5, 15 and 30 degrees). In the first column, we present the kinematic signatures of our VSI model without an embedded planet, recovering the results of our study presented in Chapter 4. In the second and third colums, we show the cases with an embedded Saturn-mass planet in a VSI-unstable disk and viscous disk, respectively. We observe that the signatures from the VSI are not seen along the region affected by the planet, while signatures from the VSI are still visible in the outermost parts of the disk; however, mixed with signatures of the spiral driven by the planet via Lindblad resonances, breaking the quasi-axisymmetry of the kinematic signatures. On the contrary, a Saturn mass planet produces weak kinematical signatures, with the exception of the Lindblad spiral triggered inner to the planets' radius (see Section 2.4). In columns four and five, we show the cases with an embedded planet with the mass of Jupiter, for our VSI-unstable disk and viscous disk simulations, respectively. In these cases, the massive planet produces a strong signature around its location. Such feature has been denominated 'Doppler-flip' (see e.g. Disk Dynamics Collaboration et al. 2020) and has a significant contribution from the planet's spiral wakes, which produces a super-Keplerian feature outside the planet's radius and a sub-Keplerian fea-

ture inside the planet's radius. Following, additional kinematical signatures are from the planets Lindblad spirals (inner and outer) and the super- and sub-Keplerian rings of gas at along the gap and gap's edges. Similar to the case for the Saturn-mass planet, for the VSI-unstable disk additional kinematical features are seen in the outermost regions of the disk, in interplay with the planetary spiral arms, wich gives a complex kinematical structure with arcs and spiral-like non-Keplerian flows. The effect of disk inclination is relevant, as seen in the comparison of the different disk models, by increasing the inclination the planet driven kinematical signatures are more prominent, while the VSI signatures velocity magnitude remains fairly constant. These results are expected, since the velocity perturbations in the gas velocity of the disk produced by the planet are strongest in the radial and azimuthal directions, which contribute more to the line-of-sight velocity for higher disk inclinations.

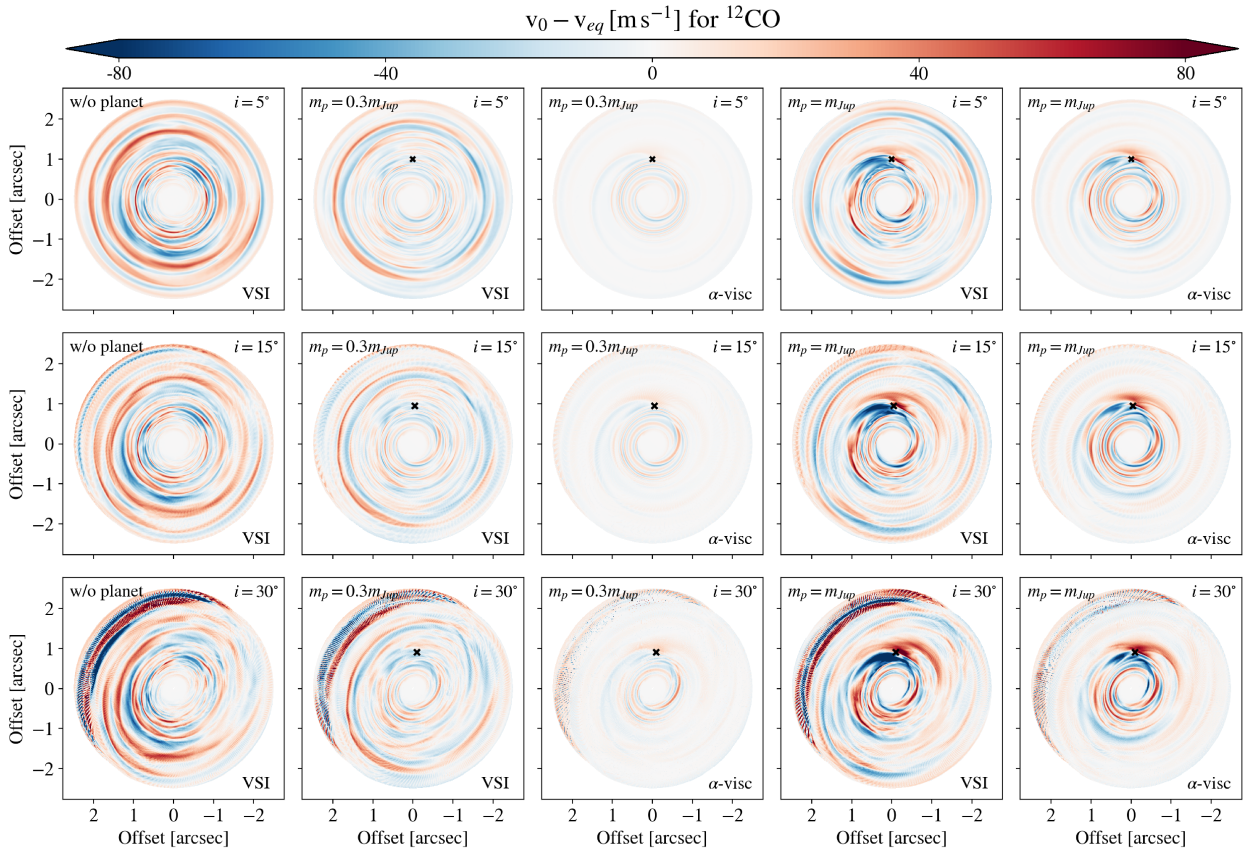

Figure 5.7: Deviations from Keplerian rotation for the RAW ^{12}CO(3 – 2) synthetic predictions of our post-processed simulations. From the left to right columns, are shown: VSI unstable disk without a planet, VSI-unstable disk with a Saturn planet, α-viscous disk with a Saturn planet, VSI-unstable disk with a Jupiter planet, and α-viscous disk with a Jupiter planet. From top to bottom, predictions for different disk inclinations are presented ($i = [5°, 15°, 30°]$). The α-viscous models are run for $\alpha = 5 \times 10^{-4}$. The approximated location of the planets are indicated with a black cross.

We further explore the kinematical signatures dependence on the traced disk region, by also computing the ideal view of the deviations from Keplerian for our ^{13}CO$(3-2)$ and C^{18}O$(3-2)$ predictions, presented in Figures 5.8 and 5.9, respectively. Moving from the most abundant tracer (^{12}CO) to the less abundant (C^{18}O), deeper layers of the disk are probed, in which the change in the morphology of the kinematic structure strongly depends on the disk inclination. In the case without embedded planets, the morphology of the non-Keplerian features remain fairly constant for different CO isotoplogues, as previously presented in Chapter 4. On the contrary, clear changes could be seen among the residuals for the three different isotopologues for the models including a massive planet. For low disk inclinations, we observe that for less abundant tracers, the planetary induced non-Keplerian flows are weaker, isolating the VSI operating in the outermost regions of the disk, but with lower velocity magnitudes compared to ^{12}CO. In addition, the contribution of the Lindblad spirals to the Keplerian models residuals weakens for less abundant tracer independent of disk inclination. Contrarily, for the case with disk inclination of 30° the Doppler-flip around the planet location and the super-Keplerian ring at the gap's outer edge remains prominent independent of CO tracer, particularly clear in the Jupiter case. These features could be explained by the planetary spiral wakes being strongest in the disk midplane, with vigorous azimuthal and radial flows, the super-Keplerian ring of gas being fairly independent on disk height, while Lindblad spiral arms and VSI flows are reach larger velocities at the disk surface (see Section 5.2.2).

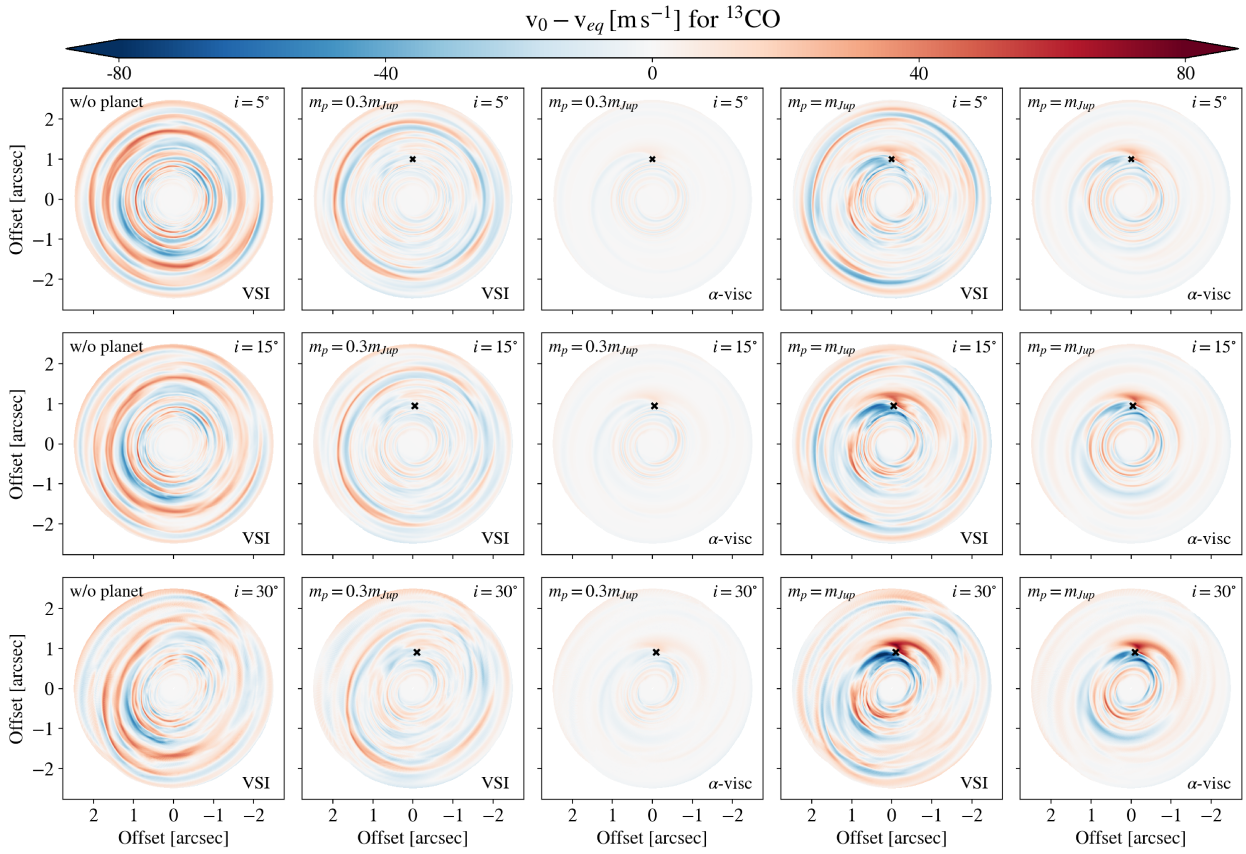

Figure 5.8: Same as Figure 5.7 but for ^{13}CO$(3-2)$.

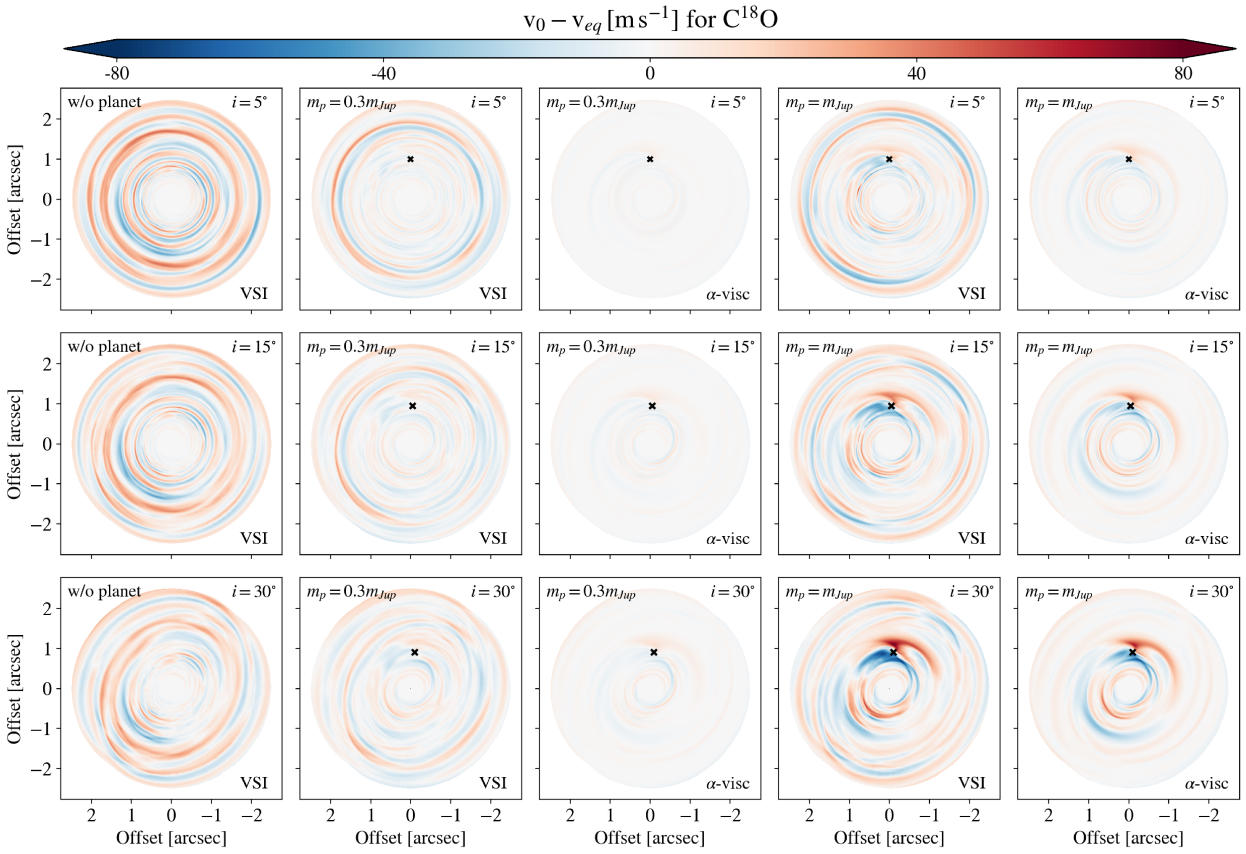

Figure 5.9: Same as Figure 5.7 but for $C^{18}O(3-2)$.

5.3.2 Kinematical Signatures: ALMA simulated observations

In order to study a more realistic picture of the kinematic signatures that could be observed in VSI-unstable planet-forming disks, we produce simulated ALMA observations for our three VSI-unstable disk models. In Figure 5.10, we show the deviations from Keplerian rotation extracted from mock observations of ^{12}CO($J:3-2$) using Eddy (see Chapter 3 Section 3.3.2), for three different inclinations ($i = [5°, 15°, \text{and } 30°]$). The simulated observations are performed for a combination of ALMA configurations 7 ($\approx$ 8 h) and 4 ($\approx$ 2 h), with longest baselines of 3.6 km and 784 m, respectively. The adopted antenna configuration is similar to the used in the large program MAPS (e.g., Öberg et al. 2021); however, for Band 7, resulting in a spatial resolution of 84×62 mas (8.4×6.2 au). In terms of spectral resolution, these are produced by a fine velocity resolution of 100 m s^{-1}, and a noise level included by corrupting the visibilities, with an RMS of 1 mJy beam^{-1} per channel (see Chapter 3 Section 3.2.2). These predictions are optimistic, and follow the ideal design for embedded planet kinematic detection (Disk Dynamics Collaboration et al. 2020; Pinte et al. 2022). Such observation would take a large amount of integration time; for example, at 345 GHz (approximated frequency of the J:3-2 transition of ^{12}CO) for a column density of water vapour of ≈ 0.9 mm such observation would take approximately 40 hours on-source. Nevertheless, these ambitious observations are the goal for the future of the community studying the kinematical structure of protoplanetary disk, needed to fully resolve the substructures in the disk gas velocities. We observe in the deviations from Keplerian rotation presented in Figure 5.10, that the VSI kinematical signatures are observed clearly only in the case without embedded planets. Arcs of VSI-induced red and blue shifted gas are also seen in the outermost regions of the Saturn mass case for disk inclinations of 5° and 15°; however, their velocity magnitude is weaker due the global damping of the VSI induced by the planet, as discussed in 5.2.2. In the case with an embedded Jupiter-mass planet, the planet-induced kinematic signatures stand out in the Keplerian model residuals; particularly a Doppler-flip around the planet and large-scale Lindblad spirals. Global patterns on the model residuals are due to errors in the model, as discussed in Chapter 4 Section 4.3.2.

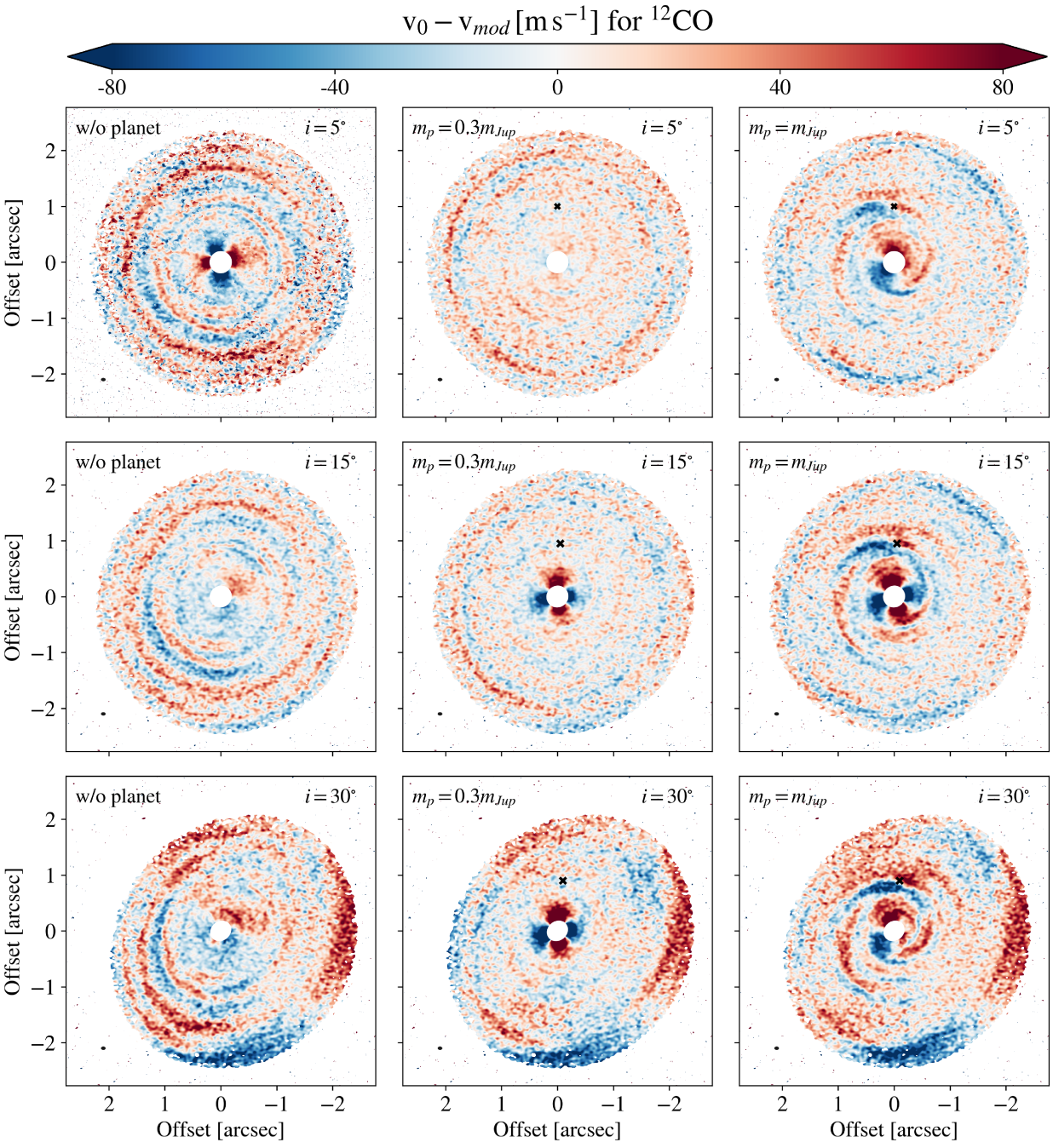

Figure 5.10: Deviations from Keplerian rotation for ^{12}CO(3 − 2) ALMA simulated observations of the post-processed simulations. From the left to right columns, are shown: VSI unstable disk without a planet, VSI-unstable disk with a Saturn planet, and VSI-unstable disk with a Jupiter planet. From top to bottom, predictions for different disk inclinations are presented ($i = [5°, 15°, 30°]$). The approximated location of the planets are indicated with a black cross. The synthesized beam of 84×62 mas is shown at the left-bottom corner of each panel. The data cubes have a velocity resolution of 100 m s^{-1}, with a RMS of 1 mJy per channel. In all images regions of low S/N have been clipped, showing only the front ^{12}CO layer.

5.4 Discussion

5.4.1 Can we confirm the VSI as origin of kinematical signatures?

While our discussion in Chapter 4 Section 4.4.1 describes how to disentangle VSI kinematical signatures from other mechanisms, there are still processes that could induce similar structures; however, observational predictions of CO kinematics of these processes still lacking. That is the case, for example, of magnetically-driven winds (e.g., Hu et al. 2022). Therefore, we face the question: If we observe a kinematical structure that perfectly matches VSI, can we robustly say that the VSI is operating therein? We discuss here that the answer is positive.

As mentioned in Section 5.2.2, flows induced by the VSI have a unique property, that is, their symmetry with respect to the disk midplane. With respect to the midplane the VSI flows are: anti-symmetric in the meridional direction, and symmetric in the radial and azimuthal direction. Luckily, it is possible to explore such feature by extracting the kinematical information of both disk hemispheres using observations of CO isotopologues, in which two layers are observed, separated by the colder disk midplane region (see e.g., channel maps of the HD 163296 disk presented in Pinte et al. 2018).

Currently, great efforts are being put to develop techniques to extract both emission CO layers, the brighter front (or upper) and the fainter back (or lower) surfaces. By fitting a double-Gaussian profile to the collapsed molecular line at each pixel, the front and back layers have been successfully extracted in the disks HD 135344B (Casassus et al., 2021) and HD 163296 (Izquierdo et al., 2022). However, deeper and higher resolution observations are needed to precisely disentangle both surfaces, crucial for kinematical analysis and study of the spatially resolved non-Keplerian flows. Moreover, mm-dust at the disk midplane can block parts of the emission from the back side layer, complicating even more its study. Nevertheless, its has been demonstrated that exploring both hemispheres of the disk in CO kinematical observations is possible. Thus, future deep high-resolution observations of CO isotopologues will be able to confirm the symmetry of the VSI flows with respect with the midplane, a robust proof of the VSI operating in planet-forming disks.

5.5 Summary and Conclusions

In this Chapter I presented a study of the gas dynamics and kinematical signatures of VSI-unstable planet forming disks, including the presence of embedded masssive planets. I performed this project by running global 3D hydrodynamical simulations, post-processed with radiative transfer calculations. Particularly, I studied the effects in the disk dynamical structure of single planets with the mass of Saturn and Jupiter.

I found that the presence of the planets substantially affect the gas velocity structure produced by the VSI, by damping their unstable modes in the regions where the structure of the disk was modified by the planets. These dampened region is particularly enclosed in the midplane layers of the disk. The effect of the planets on the VSI motions alter the kinematical signatures, in which observable kinematical signatures of the VSI are globally weakened, and only clearly visible tens of au radially outward from the planets' location. The VSI adds additional fine structure to the planet-induced kinematical signatures; however, the planetary signatures dominate the kinematical structure of the disk in the Jupiter planet case.

I compare the VSI-unstable disk with 'alpha' viscous model simulations, whose highlight is the predictions of the additional kinematical signatures produce by the VSI compared to the viscous case. The more complex kinematical structure, with a mixture of VSI-modes and planet-induced spirals, might impede the identification of planets in ALMA observations. Thus, simultaneous modelling of different CO isotopologues might be needed for a robust planet detection, where the best strategy to isolate the planet signatures is to observe closer to the midplane of moderately inclined disks.

Finally, the best chances to detect clear VSI signatures is to look for disk regions distant from observed deep continuum gaps, in which massive planets could be halting the VSI development.

6 Summary and Future Prospects

6.1 Summary

Previous theoretical studies concur that turbulence plays a crucial role in global disk evolution and in the planet formation process. However, the mechanism behind gas turbulence is still uncertain. Thus, understanding the nature of gas turbulence in planet forming disks is important to comprehend its role in the global transport of angular momentum through the disk and in the evolution of solid particles in the disk. In this dissertation, I have performed an study of observational signatures of hydrodynamical turbulence in gas kinematics of planet forming disks, which could potentially reveal the mechanism behind turbulence in high-resolution interferometric observations. In particular, I have studied the gas dynamics and kinematical signatures of planet-forming disks unstable to the vertical shear instability (VSI), a candidate to generate turbulence in the outer fast-cooling regions of protoplanetary disks. To perform my study I connected 3D global high-resolution hydrodynamical simulations with radiative transfer predictions and synthetic observations.

In Chapter 1 I briefly set the context of my work, by introducing the current status of planet formation and protoplanetary disks studies relevant to this thesis. Following, in Chapter 2 I deepen into the topic of planet-forming disks and introduce the main concepts important for this thesis.
In Chapter 3 I give details about the theory and numerical tools used through this thesis, the grid-based hydrodynamical code PLUTO, the radiative transfer code RADMC3D, the software CASA used to produce synthetic observations, and the Python tools Bettermoments and Eddy used to extract kinematical information from the simulated observations.
In Chapters 4 and 5, I present studies of the gas dynamics and kinematical

signatures of planet-forming disks unstable to the vertical shear instability. Chapter 4 presents a study of the observability of the VSI in its saturated state, I found for the first time that the gas flows induced by the VSI are observable in CO kinematic observations with the current ALMA capabilities. I found that the VSI produces unique kinematical signatures both in the individual velocity channel maps as corrugated emission, and in the residuals from subtracting a Keplerian model to the line-of-sight velocity maps as quasi-axisymmetric rings of sub- and super- Keplerian gas. Such signatures open the possibility to identify for the first time a mechanism that generates turbulence in protoplanetary disks.

In Chapter 5 I present the follow-up project of the presented in Chapter 4, in which I conducted a study of the gas dynamical evolution and kinematical signatures of a VSI-unstable disk including the presence of massive embedded planets. I studied how the influence of a Saturn and a Jupiter planet affect the development of the VSI. Moreover, I explored how the VSI influences the planet-triggered structures by directly comparing VSI-unstable and alpha-viscous models. I found that the VSI can be partially suppressed along the midplane region by the embedded massive planets, in which the velocity flows planet-induced dominate around the planet carved gap and gap edges.

As a main conclusion of my thesis I would like to stress the importance and incredible potential of gas kinematical observations. Long-baseline radio interferometric observations with ALMA can probe the three-dimensional dynamical structure of the disk, that can reveal the physical processes operating in the disk, such as gas turbulence or planet-disk interactions. In combination with dust observations, we will be able to draw a global picture of the planet-forming disks and planet formation. Nevertheless, is imperative to conduct high-resolution 3D global simulations to interpret such observations.

6.2 Future Prospects

The direction of my future work is to connect state-of-the art numerical simulations with resolved gas kinematics observations of planet-forming disks. The future prospects of my research work are the following:

6.2.1 Characterizing the vertical shear instability in protoplanetary disks

Recent CO observations with ALMA, for example, the large program MAPS (Öberg et al., 2021) have resolved kinematic signatures in planet-forming disks. These are seen as deviations from Keplerian rotation, expected for an unperturbed disk. The morphology of some of the deviations has a striking resemblance to predictions to my predictions of observational signatures from the VSI (Barraza-Alfaro et al., 2021), both showing rings and arcs of non-Keplerian gas. However, dedicated numerical simulations including the observational constraints into the hydrodynamical simulations initial conditions and physics is needed to properly model the disk substructures. To tackle this, I will conduct dedicated numerical simulations to observed protoplanetary disks, improving the thermal structure and equation of state assumed on my current simulations. By directly comparing the velocity deviations recovered from ALMA observations to synthetic predictions, I will disentangle if the signatures are from the VSI or/and alternative mechanisms (e.g., embedded planets). The characterization of the VSI operating in a protoplanetary disk would confirm for the first time the VSI as a source of gas turbulence, with a significant impact on the understanding of the planet-forming environment.

6.2.2 Simulations and predictions of exoALMA protoplanetary disks

The ALMA large program exoALMA (PI: R. Teague) will observe the gas kinematics of 15 protoplanetary disks, with a high angular resolution (100 mas) for the highest spectral resolution available in ALMA Band 7 (i.e., 26 m s^{-1}). I will be involved in the theoretical interpretation of the observed features, for example, running numerical simulations and radiative transfer models to constraining the locations and masses of the embedded exoplanets. The planets that are expected to be detected with exoALMA are fairly massive ($>$ Saturn mass) and orbit at large distances from the star ($>$10 au).

The detection of a population of forming exoplanets in that region of parameters would reveal efficient massive planet formation in the outer parts of the disk, challenging our current knowledge about planet formation mechanisms and timescales.
For alternative scenarios to explain the origin of the observed substructures, I will lead a project to study if observed non-Keplerian ring substructures in CO kinematics are produced by the VSI. Again, as shown in Chapter 4 (see also; Barraza-Alfaro et al. 2021) these ring structures could indicate that the VSI is operating in the disk. Finally, I will help in constraining the level of turbulence and explore mechanisms behind turbulence in the exoALMA targets.

6.2.3 Understanding the interplay between forming planets and their environment

As highlighted in this thesis, protoplanetary disks are three-dimensional objects; therefore, three-dimensional global numerical simulations are essential for the interpretation of disk observations. However, these simulations are computationally expensive, which has created a gap in our knowledge of the origin of substructures in protoplanetary disks. In particular, the interplay between planet-disk interactions and other physical processes in the disk is still highly unexplored.
Planet-triggered structures with simplified disk physics have been widely studied. Under strong assumptions, the structures triggered by planets are well understood and is known that these substructures will be fully resolved with upcoming facilities. Therefore, studies of how other disk physical processes would affect the observable planet-triggered structures can be used to extract essential information about the disk and understand the environment of forming planets. Furthermore, knowledge about how other physical processes affect the magnitude of the spiral wakes around the forming planets is fundamental to constrain their masses correctly, important to properly trace the properties of the population of forming exoplanets. In my future work I will set, run and analyze simulations of planet-disk interactions including realistic physics, in order to explore the interplay between forming planets and other physical processes in the disk.

6.2.4 Exploring the potential of upcoming observational facilities

In addition, my future research will have the goal of connecting theoretical predictions to upcoming observational facilities, in order to understand their interpretation. In the near future, particularly important will be the upgrade of ALMA capabilities (ALMA2030), with a planned increase of the spectral line sensitivity and bandwidth, among other improvements. The upgrade in spectral line sensitivity will significantly reduce the observing time required to reach science goals for molecular line observations. Therefore, it will ease obtain high quality data with high spatial and spectral resolution, essential to resolve kinematical signatures in planet-forming disks and apply to its full potential the current techniques to extract the disk kinematical structure. Therefore, detailed predictions of gas kinematics will be necessary.
Future observatories in mm- and cm-wavelengths, such as the next generation Very Large Array (ngVLA), will trace dust thermal emission in au scales. With such exquisite spatial resolution, fine dust substructures will be resolved if present (see e.g., Blanco et al. 2021). Particularly exciting is that substructures produced by massive planets analogs to our Solar System's giants might be possible (see e.g., Bergez-Casalou et al. 2022). However, is still unexplored the potential to probe gas kinematics with ngVLA, in which I will contribute in the near future.
Finally, in near-IR and optical wavelengths, the Webb space telescope and the Extremely Large Telescope (ELT) aim to detect the thermal emission of embedded protoplanets. If successful, the detected location of the planets will be used as input in my numerical simulations, substantially improving current models. By reproducing the resolved substructures in multi-wavelength observations with numerical simulations I will have a detailed global picture of planet-disk interactions. With this full picture, I will be able to use the planet-triggered structures to calibrate current numerical simulations, that will tightly constrain the forming planets' masses, disks' physical properties and the planet-formation environment.

List of publications

These scientific publications have been submitted and published during my studies, or are in preparation for publication within this year.

List of first-author publications included in this thesis

1. **Barraza-Alfaro M.**, Flock M., Marino S., Pérez S., 2021, A&A, 653, A113. *Observability of the vertical shear instability in protoplanetary disk CO kinematics*

2. **Barraza-Alfaro M.**, Flock M. in prep. *Kinematical signatures of planet-disk interactions in VSI-turbulent protoplanetary disks*

List of contributions to publications not included in this thesis

1. Brown-Sevilla S. B., Keppler M., **Barraza-Alfaro M.**, Melon Fuksman J. D., Kurtovic N., Pinilla P., Feldt M., et al., 2021, A&A, 654, A35. *A multiwavelength analysis of the spiral arms in the protoplanetary disk around WaOph 6*

2. Alarcón F., Teague R., Zhang K., Bergin E. A., **Barraza-Alfaro M.**, 2020, ApJ, 905, 68. *Chemical Evolution in a Protoplanetary Disk within Planet Carved Gaps and Dust Rings*

3. Baruteau C., **Barraza M.**, Pérez S., et al., 2019, MNRAS, 486, 304. *Dust traps in the protoplanetary disc MWC 758: two vortices produced by two giant planets?*

4. Blanc G.A., Lu Y., Benson A., Katsianis A., **Barraza M.**, 2019, ApJ, 877, 6. *A Characteristic Mass Scale in the Mass-Metallicity Relation of Galaxies*

5. Casassus S., Marino S., Lyra W., ..., **Barraza M.**, et al., 2019, MNRAS, 483, 3278. *Cm-wavelength observations of MWC 758: resolved dust trapping in a vortex*

6. Casassus S., Avenhaus H., Pérez S., ..., **Barraza M.**, et al., 2018, MNRAS, 477, 5104. *An inner warp in the DoAr 44 T Tauri transition disc*

7. Reggiani M., Christiaens V., Absil O., ..., **Barraza M.**, et al., 2018, A&A, 611, A74. *Discovery of a point-like source and a third spiral arm in the transition disk around the Herbig Ae star MWC 758*

Bibliography

Alarcón, F., Teague, R., Zhang, K., Bergin, E. A., & Barraza-Alfaro, M. 2020, ApJ, 905, 68 25

ALMA Partnership, Brogan, C. L., Pérez, L. M., et al. 2015, ApJ, 808, L3 8, 12

Andrews, S. M., Huang, J., Pérez, L. M., et al. 2018, The Astrophysical Journal, 869, L41 13

Asensio-Torres, R., Henning, T., Cantalloube, F., et al. 2021, A&A, 652, A101 19

Avenhaus, H., Quanz, S. P., Garufi, A., et al. 2018, The Astrophysical Journal, 863, 44 13

Bae, J., Teague, R., & Zhu, Z. 2021, ApJ, 912, 56 24, 65

Bae, J., & Zhu, Z. 2018, ApJ, 859, 118 24

Bae, J., Zhu, Z., & Hartmann, L. 2017, The Astrophysical Journal, 850, 201 24

Bai, X.-N. 2017, ApJ, 845, 75 15

Balbus, S. A., & Hawley, J. F. 1991, ApJ, 376, 214 16

Barge, P., & Sommeria, J. 1995, A&A, 295, L1 25, 65

Barraza-Alfaro, M., Flock, M., Marino, S., & Pérez, S. 2021, A&A, 653, A113 21, 45, 99, 100

Baruteau, C., Crida, A., Paardekooper, S. J., et al. 2014, in Protostars and Planets VI, ed. H. Beuther, R. S. Klessen, C. P. Dullemond, & T. Henning, 667 26

Baruteau, C., Barraza, M., Pérez, S., et al. 2019, MNRAS, 486, 304 19, 25, 32, 33, 51

Benisty, M., Bae, J., Facchini, S., et al. 2021, ApJ, 916, L2 8, 26

Bergez-Casalou, C., Bitsch, B., Kurtovic, N. T., & Pinilla, P. 2022, A&A, 659, A6 101

Bi, J., Lin, M.-K., & Dong, R. 2021, ApJ, 912, 107 25

Binkert, F., SzulÃ¡gyi, J., & Birnstiel, T. 2021, Monthly Notices of the Royal Astronomical Society, 506, 5969 25

Birnstiel, T., Dullemond, C. P., & Brauer, F. 2010, A&A, 513, A79 14

Blanco, D., Ricci, L., Flock, M., & Turner, N. 2021, ApJ, 920, 70 101

Boehler, Y., Ménard, F., Robert, C. M. T., et al. 2021, A&A, 650, A59 21

Bohren, C. F., & Huffman, D. R. 1983, Absorption and scattering of light by small particles 33

Carrasco-González, C., Sierra, A., Flock, M., et al. 2019, ApJ, 883, 71 12

Casassus, S., & Pérez, S. 2019, ApJ, 883, L41 20, 40, 67

Casassus, S., Christiaens, V., Cárcamo, M., et al. 2021, MNRAS, 507, 3789 94

Cui, C., & Bai, X.-N. 2020, ApJ, 891, 30 16, 66

Desch, S. J., & Turner, N. J. 2015, ApJ, 811, 156 15

Dipierro, G., Price, D., Laibe, G., et al. 2015, MNRAS, 453, L73 24

Disk Dynamics Collaboration, Armitage, P. J., Bae, J., et al. 2020, arXiv e-prints, arXiv:2009.04345 8, 19, 21, 22, 26, 40, 64, 85, 86, 92

Dong, R., Liu, S.-Y., & Fung, J. 2019, ApJ, 870, 72 25

Draine, B. T., & Lee, H. M. 1984, ApJ, 285, 89 33

Dubrulle, B., Morfill, G., & Sterzik, M. 1995, Icarus, 114, 237 33

Dullemond, C. P., Juhasz, A., Pohl, A., et al. 2012, RADMC-3D: A multi-purpose radiative transfer tool, ascl:1202.015 32

Dullemond, C. P., Birnstiel, T., Huang, J., et al. 2018, ApJ, 869, L46 14

Dzyurkevich, N., Turner, N. J., Henning, T., & Kley, W. 2013, ApJ, 765, 114 15

Flaherty, K., Hughes, A. M., Simon, J. B., et al. 2020, ApJ, 895, 109 14, 15, 17, 61

Flaherty, K. M., Hughes, A. M., Rosenfeld, K. A., et al. 2015, ApJ, 813, 99 15, 17

Flaherty, K. M., Hughes, A. M., Teague, R., et al. 2018, ApJ, 856, 117 15, 17

Flaherty, K. M., Hughes, A. M., Rose, S. C., et al. 2017, ApJ, 843, 150 15, 17

Flock, M., Nelson, R. P., Turner, N. J., et al. 2017, ApJ, 850, 131 16, 17, 18, 31, 33, 65

Flock, M., Ruge, J. P., Dzyurkevich, N., et al. 2015, A&A, 574, A68 14

Flock, M., Turner, N. J., Nelson, R. P., et al. 2020, ApJ, 897, 155 16, 18, 33, 65, 66

Flores-Rivera, L., Flock, M., & Nakatani, R. 2020, A&A, 644, A50 16, 62

Fromang, S., & Papaloizou, J. 2006, A&A, 452, 751 14

Fu, W., Li, H., Lubow, S., & Li, S. 2014, ApJ, 788, L41 14

Fukuhara, Y., Okuzumi, S., & Ono, T. 2021, ApJ, 914, 132 17

Fung, J., & Chiang, E. 2016, ApJ, 832, 105 64

Garufi, A., Avenhaus, H., Pérez, S., et al. 2020, A&A, 633, A82 13

Goldreich, P., & Tremaine, S. 1980, ApJ, 241, 425 23

Goldreich, P., & Ward, W. R. 1973, ApJ, 183, 1051 12

Guilloteau, S., Dutrey, A., Wakelam, V., et al. 2012, A&A, 548, A70 15

Hall, C., Dong, R., Teague, R., et al. 2020, ApJ, 904, 148 21, 64

Hawley, J. F., & Balbus, S. A. 1991, ApJ, 376, 223 16

Hu, X., Li, Z.-Y., Zhu, Z., & Yang, C.-C. 2022, arXiv e-prints, arXiv:2203.05629 94

Huang, P., Isella, A., Li, H., Li, S., & Ji, J. 2018, The Astrophysical Journal, 867, 3 25, 64, 65

Hughes, A. M., Wilner, D. J., Andrews, S. M., Qi, C., & Hogerheijde, M. R. 2011, ApJ, 727, 85 15

Izquierdo, A. F., Facchini, S., Rosotti, G. P., van Dishoeck, E. F., & Testi, L. 2022, ApJ, 928, 2 20, 40, 94

Izquierdo, A. F., Testi, L., Facchini, S., Rosotti, G. P., & van Dishoeck, E. F. 2021, A&A, 650, A179 40

Juhász, A., & Rosotti, G. P. 2018, MNRAS, 474, L32 64

Kanagawa, K. D., Muto, T., Tanaka, H., et al. 2016, PASJ, 68, 43 24

Kant, I. 1755, Allgemeine Naturgeschichte und Theorie des Himmels oder Versuch von der Verfassung und dem mechanischen Ursprunge des ganzen Weltgebäudes nach Newtonischen Grundsätzen abgehandelt (Petersen, Königsberg and Leipzig) 7

Kepley, A. A., Tsutsumi, T., Brogan, C. L., et al. 2020, PASP, 132, 024505 36

Keppler, M., Benisty, M., Müller, A., et al. 2018, A&A, 617, A44 8

Klahr, H., & Hubbard, A. 2014, ApJ, 788, 21 16

Kley, W., D'Angelo, G., & Henning, T. 2001, ApJ, 547, 457 24, 64

Laplace, P. S. 1796, Exposition du Systéme du Monde (Imprimerie Cercele-Social, Paris) 7

Lesur, G., Ercolano, B., Flock, M., et al. 2022, arXiv e-prints, arXiv:2203.09821 14, 16, 18

Li, A., & Greenberg, J. M. 1997, A&A, 323, 566 33

Li, Y.-P., Li, H., Li, S., et al. 2020, The Astrophysical Journal, 892, L19 25

Lin, M.-K., & Youdin, A. N. 2015, ApJ, 811, 17 66

Lynden-Bell, D., & Pringle, J. E. 1974, MNRAS, 168, 603 14

Lyra, W. 2014, ApJ, 789, 77 16

Lyra, W., Johansen, A., Zsom, A., Klahr, H., & Piskunov, N. 2009, A&A, 497, 869 14

Lyra, W., & Umurhan, O. M. 2019, PASP, 131, 072001 16, 18

Malygin, M. G., Klahr, H., Semenov, D., Henning, T., & Dullemond, C. P. 2017, A&A, 605, A30 16

Manger, N., & Klahr, H. 2018, MNRAS, 480, 2125 17, 18, 65

Marcus, P. S., Pei, S., Jiang, C.-H., & Barranco, J. A. 2016, ApJ, 833, 148 16

Marcus, P. S., Pei, S., Jiang, C.-H., et al. 2015, ApJ, 808, 87 16

McMullin, J. P., Waters, B., Schiebel, D., Young, W., & Golap, K. 2007, in Astronomical Society of the Pacific Conference Series, Vol. 376, Astronomical Data Analysis Software and Systems XVI, ed. R. A. Shaw, F. Hill, & D. J. Bell, 127 35, 85

Mignone, A., Bodo, G., Massaglia, S., et al. 2007, in JENAM-2007, "Our Non-Stable Universe", 96–96 29

Miotello, A., Kamp, I., Birnstiel, T., Cleeves, L. I., & Kataoka, A. 2022, arXiv e-prints, arXiv:2203.09818 12

Morbidelli, A., Szulágyi, J., Crida, A., et al. 2014, Icarus, 232, 266 24, 64

Muro-Arena, G. A., Dominik, C., Waters, L. B. F. M., et al. 2018, A&A, 614, A24 13

Nelson, R. P., Gressel, O., & Umurhan, O. M. 2013, MNRAS, 435, 2610 16, 17, 46, 66

Öberg, K. I., Guzmán, V. V., Walsh, C., et al. 2021, ApJS, 257, 1 13, 19, 21, 92, 99

Ormel, C. W., & Cuzzi, J. N. 2007, A&A, 466, 413 14

Paardekooper, S.-J., Dong, R., Duffell, P., et al. 2022, arXiv e-prints, arXiv:2203.09595 26

Paneque-Carreño, T., Pérez, L. M., Benisty, M., et al. 2021, The Astrophysical Journal, 914, 88 21

Pérez, S., Casassus, S., & Benítez-Llambay, P. 2018, MNRAS, 480, L12 19, 64, 75

Perez, S., Dunhill, A., Casassus, S., et al. 2015, ApJ, 811, L5 19, 26, 64, 65

Pérez, S., Casassus, S., Hales, A., et al. 2020, ApJ, 889, L24 20

Pfeil, T., & Klahr, H. 2019, ApJ, 871, 150 16

Pfeil, T., & Klahr, H. 2021, The Astrophysical Journal, 915, 130 17, 18, 66, 80

Picogna, G., Stoll, M. H. R., & Kley, W. 2018, A&A, 616, A116 14

Pinilla, P., Benisty, M., & Birnstiel, T. 2012a, A&A, 545, A81 13, 14, 24

Pinilla, P., Birnstiel, T., Ricci, L., et al. 2012b, A&A, 538, A114 13, 14

Pinte, C., Dent, W. R. F., Ménard, F., et al. 2016, ApJ, 816, 25 14, 33

Pinte, C., Teague, R., Flaherty, K., et al. 2022, arXiv e-prints, arXiv:2203.09528 14, 19, 21, 26, 92

Pinte, C., Price, D. J., Ménard, F., et al. 2018, ApJ, 860, L13 20, 58, 94

Pinte, C., van der Plas, G., Ménard, F., et al. 2019, Nature Astronomy, 3, 1109 20

Pinte, C., Price, D. J., Ménard, F., et al. 2020, ApJ, 890, L9 20, 85

Rabago, I., & Zhu, Z. 2021, MNRAS, 502, 5325 75

Regály, Z., Juhász, A., Sándor, Z., & Dullemond, C. P. 2012, MNRAS, 419, 1701 14

Richard, S., Nelson, R. P., & Umurhan, O. M. 2016, MNRAS, 456, 3571 65

Robert, C. M. T., Méheut, H., & Ménard, F. 2020, A&A, 641, A128 21, 25, 64, 65

Rosotti, G. P., Benisty, M., JuhÃ¡sz, A., et al. 2019, Monthly Notices of the Royal Astronomical Society, 491, 1335 21

Schäfer, Urs, Johansen, Anders, & Banerjee, Robi. 2020, A&A, 635, A190 18, 65

Schöier, F. L., van der Tak, F. F. S., van Dishoeck, E. F., & Black, J. H. 2005, A&A, 432, 369 34

Segura-Cox, D. M., Schmiedeke, A., Pineda, J. E., et al. 2020, Nature, 586, 228 22

Shakura, N. I., & Sunyaev, R. A. 1973, A&A, 500, 33 14, 30, 75

Simon, J. B., Hughes, A. M., Flaherty, K. M., Bai, X.-N., & Armitage, P. J. 2015, ApJ, 808, 180 15, 61

Speedie, J., Booth, R. A., & Dong, R. 2022, The Astrophysical Journal, 930, 40 24

Stoll, M. H. R., & Kley, W. 2014, A&A, 572, A77 16, 17

—. 2016, A&A, 594, A57 18, 33

Stoll, M. H. R., Picogna, G., & Kley, W. 2017, A&A, 604, A28 73, 74

Stoll, Moritz H. R., Kley, Wilhelm, & Picogna, Giovanni. 2017, A&A, 599, L6 16, 33, 62

Szulágyi, J., Binkert, F., & Surville, C. 2022, ApJ, 924, 1 26

Szulágyi, J., Morbidelli, A., Crida, A., & Masset, F. 2014, ApJ, 782, 65 24

Szulágyi, J., Plas, G. v. d., Meyer, M. R., et al. 2017, Monthly Notices of the Royal Astronomical Society, 473, 3573 26

Tanigawa, T., Ohtsuki, K., & Machida, M. N. 2012, ApJ, 747, 47 24

Teague, R. 2019a, The Journal of Open Source Software, 4, 1220 37

—. 2019b, The Journal of Open Source Software, 4, 1632 68

Teague, R. 2019, Research Notes of the American Astronomical Society, 3, 74 36

Teague, R., Bae, J., & Bergin, E. A. 2019a, Nature, 574, 378 20, 56, 64

Teague, R., Bae, J., Bergin, E. A., Birnstiel, T., & Foreman-Mackey, D. 2018a, ApJ, 860, L12 20, 22

Teague, R., Bae, J., Huang, J., & Bergin, E. A. 2019b, ApJ, 884, L56 20

Teague, R., & Foreman-Mackey, D. 2018, Research Notes of the American Astronomical Society, 2, 173 36, 66

Teague, R., Guilloteau, S., Semenov, D., et al. 2016, A&A, 592, A49 15, 17

Teague, R., Henning, T., Guilloteau, S., et al. 2018b, ApJ, 864, 133 15

Teague, R., Bae, J., Aikawa, Y., et al. 2021, ApJS, 257, 18 19, 20, 21, 26, 38

Trapman, L., Rosotti, G., Bosman, A. D., Hogerheijde, M. R., & van Dishoeck, E. F. 2020, A&A, 640, A5 17

Turner, N. J., Fromang, S., Gammie, C., et al. 2014, in Protostars and Planets VI, ed. H. Beuther, R. S. Klessen, C. P. Dullemond, & T. Henning, 411 14, 15

Villenave, M., Ménard, F., Dent, W. R. F., et al. 2020, A&A, 642, A164 14, 33, 65

Villenave, M., Stapelfeldt, K. R., Duchêne, G., et al. 2022, ApJ, 930, 11 14

Wilson, T. L., & Rood, R. 1994, ARA&A, 32, 191 34

Wölfer, L., Facchini, S., Kurtovic, N. T., et al. 2021, A&A, 648, A19 20

Wolszczan, A., & Frail, D. A. 1992, Nature, 355, 145 7

Yen, H.-W., & Gu, P.-G. 2020, ApJ, 905, 89 54

Yu, H., Teague, R., Bae, J., & Öberg, K. 2021, ApJ, 920, L33 20

Zhang, K., Bergin, E. A., Blake, G. A., Cleeves, L. I., & Schwarz, K. R. 2017, Nature Astronomy, 1, 0130 58, 59

Zhang, S., Zhu, Z., Huang, J., et al. 2018, ApJ, 869, L47 19, 24

Zhu, Z., Andrews, S. M., & Isella, A. 2018, Monthly Notices of the Royal Astronomical Society, 479, 1850 26

Acknowledgements

I would like to thank to all the people that accompanied me and gave me support during my PhD studies. Firstly, I would like to thank my PhD advisor Mario Flock for its amazing support and guidance. Secondly, to the members of my PhD thesis committee C. Dullemond and B. Bitsch. Thirdly, to the members of the UFOS group G. Bertrang and L. Flores-Rivera, and the scientists part of our weekly group meetings at MPIA, which always provided rich discussions, in particular P. Pinilla, B. Bitsch, D. Semenov, C. Bergez-Casalou, S. Savvidou, G. Smirnov-Pichunkov and T. Delage. Fourthly, to my collaborators S. Pérez and S. Marino. Fifthly, to my friends in Heidelberg P. Bluhm, I. Pessa, N. Kurtovic, J. Isbell, O. Völkel, G. Mattia, S. Brown-Sevilla, D. Melon-Fuksman, and other IMPRS students. Finally, special thanks to all my family and friends in Chile.

Also, I would like to acknowledge the work of the developers of the *freely available* tools used during this thesis. In particular, A. Mignone (PLUTO), C. Dullemond (RADMC3D) and R. Teague (Bettermoments and Eddy).

The research presented in this dissertation was possible thanks to the funding from the European Research Council (ERC) under the European Union's Horizon 2020 research and innovation program (grant agreement No. 757957).

The numerical simulations presented in this thesis were run in the on the HPC system COBRA at MPCDF (Max Planck Computing and Data Facility). Simulation tests, radiative transfer predictions and simulated observations were run on the MPIA clusters.

Declaration of Originality

Declaration of Originality

I hereby declare that this thesis is my own work and that I have used no other than the stated sources and aids.

Erklärung zur Originalität der Arbeit

Ich versichere, dass ich diese Arbeit selbstständig verfasst habe und keine anderen als die angegebenen Quellen und Hilfsmittel benutzt habe.

Heidelberg, der 16. Mai 2022

Marcelo Barraza-Alfaro